

GLOBAL AND SEASONAL EFFECTS OF
LIGHTNING-INDUCED ELECTRON PRECIPITATION

A DISSERTATION
SUBMITTED TO THE COMMITTEE ON GRADUATE STUDIES
OF STANFORD UNIVERSITY
IN PARTIAL FULFILLMENT OF THE REQUIREMENTS
FOR THE DEGREE OF
DOCTOR OF PHILOSOPHY
IN
ELECTRICAL ENGINEERING

Austin Patrick Sousa
April 2018

© Copyright by Austin Patrick Sousa 2018

All Rights Reserved

I certify that I have read this dissertation and that, in my opinion, it is fully adequate in scope and quality as a dissertation for the degree of Doctor of Philosophy.

(Prof. Sigrid Close) Principal Adviser

I certify that I have read this dissertation and that, in my opinion, it is fully adequate in scope and quality as a dissertation for the degree of Doctor of Philosophy.

(Prof. Robert Marshall, University of Colorado Boulder)

I certify that I have read this dissertation and that, in my opinion, it is fully adequate in scope and quality as a dissertation for the degree of Doctor of Philosophy.

(Prof. Antony Fraser-Smith)

Approved for the Stanford University Committee on Graduate Studies

Preface

This thesis tells you all you need to know about...

Acknowledgments

(Acknowledgements go here)

Contents

Preface	iv
Acknowledgments	v
1 Introduction	1
1.1 The Space Environment	1
1.2 Motivation	2
1.2.1 The Radiation Belts	2
1.2.2 Sources and Loss Processes	3
1.3 Previous Work	5
1.3.1 Wave-Particle Interactions	5
1.3.2 LEP measurements	6
1.3.3 Modeling of single LEP events	7
1.3.4 Behavior of whistler waves in the magnetosphere	8
1.3.5 Electron lifetime estimates due to LEP	8
1.4 Scientific Contribution	8
1.5 Thesis Organization	8
2 Physics and Methods	10
2.1 Overview of Plasma Physics	10
2.1.1 Single Particle Motion	11
2.1.2 The Loss Cone	14
2.1.3 Waves in Plasmas	17
2.2 Lightning Illumination Model	22

2.3	The Ionosphere	23
2.3.1	Trans-Ionosphere Attenuation	23
2.3.2	Models of the Ionosphere	26
2.4	The Earth’s magnetic field	28
2.4.1	Models of the magnetic field	28
2.5	The Plasmasphere	30
2.5.1	Ray Tracing	34
2.5.2	Landau Damping	38
2.6	The Radiation Belts	40
2.7	Wave-Particle Interactions	41
2.7.1	Resonant Interactions	44
2.7.2	Recovering Wave Amplitudes from Poynting Flux	46
2.8	The GLD360 Lightning Dataset	47
3	VLF energy in the Near-Earth Environment	51
3.1	Methodology	51
3.2	Persistent Energy from a Single Flash	52
3.2.1	Radiated power above the ionosphere	52
3.2.2	Gridding and Interpolation	54
3.2.3	Energy imparted by a single flash	61
3.3	Global Energy Density	61
3.3.1	Results of the global model	65
3.4	Longitude Dependence	68
4	Global and Seasonal Estimates of LEP	74
4.1	Resonant Interactions	74
4.1.1	Calculating pitch-angle scattering vs time	76
4.1.2	Example energy-time spectra	79
4.2	Calculating flux from pitch-angle perturbations	81
4.3	LEP stencils and the behavior of a single flash	85
4.4	Coordinate deformation	89
4.5	Global and Seasonal Energy Fluxes	92

4.6	Lifetime Estimates	96
4.7	Comparison to other research	100
5	Satellite Instrumentation	103
5.1	VPM Mission Overview	104
5.2	Hardware Architecture	107
5.2.1	FPGAs	108
5.2.2	Power and GPS	110
5.2.3	DPU	111
5.2.4	VLF Receiver Boards	112
5.2.5	Deployable Antennas	114
5.3	Firmware Architecture	117
5.3.1	Reduced-Resolution (Survey) Data	118
5.3.2	Full-Resolution Burst Data	122
5.3.3	GPS Timestamps	124
5.3.4	System Status Messages	125
5.3.5	Memory and Data Storage	127
5.3.6	System Control	129
5.4	Concluding Remarks	129
6	Conclusions	131
6.1	Suggestions for Future Work	131
A	Reference Equations	132
A.1	Landau Damping	132
	Bibliography	135

List of Tables

3.1	Simulation Parameters	53
4.1	Stencil Simulation Parameters	85
5.1	Burst mode duty cycle modulation settings	124

List of Figures

1.1	Diagram of the various regions of the space environment	2
1.2	An example of a lightning-generated whistler wave	6
2.1	An example of a “magnetic bottle” particle trap	13
2.2	Adiabatic motion in the Earth’s magnetic field	15
2.3	Loss cone illustration	16
2.4	An ω -K diagram for the cold, four-component dispersion relation, for parallel propagation at $L \approx 3$	21
2.5	Time and frequency profiles of the lightning illumination model	24
2.6	Trans-Ionosphere attenuation curves for day and night	27
2.7	Ionosphere density profile	28
2.8	Magnetic field models	31
2.9	L-shell contours on the Earth’s surface	32
2.10	Histogram of K_p data	33
2.11	Model of plasmapause location	34
2.12	A Comparison of three plasmasphere electron density models	35
2.13	Example ray tracing	37
2.14	Phase-space density functions	40
2.15	AE8 integral flux model	42
2.16	Pitch-angle distribution functions	43
2.17	Illustration of resonant wave-particle interactions	44
2.18	Distributions of peak current and MLT for the GLD360 dataset . .	49
2.19	Average global flash rate	49
2.20	Average global peak current rate rate	50

3.1	Energy density calculation block diagram	52
3.2	Illumination pattern below the ionosphere	54
3.3	Illumination pattern above the ionosphere	55
3.4	Energy above the ionosphere due to a single flash	56
3.5	Illustrations of the interpolation scheme	57
3.6	Delaunay interpolation method	58
3.7	Fine-scale frequency interpolation	59
3.8	Illustration of a convex hull in two dimensions. (a) A simple polygon, shown in orange, for which the convex hull and concave hulls differ substantially. (b) A collection of random points, and their concave hull.	60
3.9	Energy density in the meridional plane for a single flash	62
3.10	Energy density vs time vs L-shell	63
3.11	Energy density stencils	64
3.12	Average energy density vs longitude and L	66
3.13	Average energy density vs L, longitude-averaged	67
3.14	Average energy density vs L for multiple K_p	67
3.15	Average energy density vs L and frequency	68
3.16	2D vs 3D longitude scaling geometries	70
3.17	Relative longitude scaling factors per latitude	71
3.18	Difference between 2d and 3d longitude scaling	72
3.19	Total percent error in 2D scaling	73
4.1	Resonant frequency vs particle energy for resonant modes 0, 1, and 2	76
4.2	test particle sim	77
4.3	Pitch angle scattering matrix along a fieldline with L=3, for a 10 kA flash at 35° latitude, through a nightside ionosphere at $K_p = 0$. Scattering is centered directly over the input flash longitude, within a width of ±0.25°.	80

4.4	(a) Reflection altitude vs L-shell for a particle, for an array of equatorial pitch-angle perturbations. (b) The minimum perturbation required to drive a particle with pitch angle $\alpha = \alpha_{lc}$ to a fixed reflection altitude, as a function of L-shell, for an array of target altitudes.	81
4.5	Pitch angle perturbation vs gyrophase, and corresponding PDF	82
4.6	Perturbed pitch-angle distribution	83
4.7	Precipitating flux density E-t spectra for $\lambda_s = 35^\circ$ and L=3	84
4.8	Precipitating flux density stencils for a range of input latitudes and magnetospheric conditions (nightside)	87
4.9	Precipitating flux density stencils for a range of input latitudes and magnetospheric conditions (dayside)	88
4.10	Total precipitated energy for a single flash	89
4.11	Energy spectrum of LEP stencils	90
4.12	Comparison of Magnetic Dipole (MAG) and Corrected Geomagnetic (CGM) coordinates	91
4.13	GLD average peak current density, adjusted using AACGM coordinates	93
4.14	Global energy deposition “hot spots” for maximal and minimal radiation belt populations	95
4.15	Global energy deposition due to LEP	96
4.16	Global energy deposition due to LEP over the continental United States	97
4.17	Energy spectrum of LEP stencils, drawn from a uniform radiation belt population	99
4.18	Estimated lifetime of radiation belt electrons subject to LEP losses only	100
4.19	Precipitation at 123 keV over the continental United States, for summer and winter	101
4.20	Electron lifetime estimates compared against <i>Meredith et al. (2007)</i> .	102
5.1	Drawing of the assembled VPM payload on a 6U cubesat bus	107
5.2	On-orbit alignment of the VPM payload	108
5.3	VPM payload hardware instrument arrangement	109

5.4	Simplified schematic of the μ BBR signal conditioning and data conversion chain	113
5.5	Pseudo-random calibration signals	115
5.6	Frequency response and noise floor of the μ BBR analog processing chain	116
5.7	Characteristics of the search coil and associated preamp	117
5.8	Approximate detectable field magnitudes	118
5.9	Block diagram of VPM firmware modules	119
5.10	Block diagram of the fixed-point log scaling module	122
5.11	Interleaving scheme for survey data	123
5.12	24-bit command structure for burst experiments	125
5.13	Example of a frequency-domain burst experiment and corresponding survey data	126
5.14	Structure of packets returned by VPM	129

Chapter 1

Introduction

1.1 The Space Environment

Surrounding the Earth there exists a sparse gas of ions and electrons called a *plasma*. These particles reside in a state of constant flux, resulting from a tenuous and dynamic balance of energy fluxes – streaming in from the sun, and back and forth within the Earth’s terrestrial atmosphere. Every human-made satellite has passed through it; the vast majority of satellites, with the exception of deep-space probes, live out their entire existence within it. Aside from the lunar astronauts of the Apollo era, every single human in space has spent the duration of their journey within this constantly-evolving cloud of matter. The technology ubiquitous in our day-to-day lives – instant international communication, satellite-aided global positioning systems – all require signals to be transmitted through it. We call this region, from say, an altitude of 100 km on out to the moon, the *Space Environment*.

The space environment is largely defined by the Earth’s magnetic field, which serves to constrain plasma to a toroidal shape. The region in which the Earth’s magnetic field impacts significant action is called the *magnetosphere*, and the region of constrained plasma immediately surrounding the Earth the *plasmasphere*. The majority of the particles within the plasmasphere are cold, with energies less than ~ 1 eV. However, a sparse population of high-energy particles exist, with energies approaching 10 MeV, and velocities approaching the speed of light. These so-called

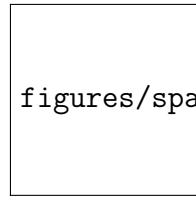


Figure 1.1: Write me pls

‘killer electrons’, while sparse in number, present a significant hazard for both electrical systems, and to living organisms in space(*Barth et al.*, 2003). The populations of these particles form two shells, known as the Van Allen radiation belts, separated by a depleted ‘slot’ region. Understanding the behavior of these high-energy particles are key to sustained human activity in space.

The population of high-energy particles is driven by a complex balance of sources, acceleration mechanisms, and loss processes. This thesis considers the effect of one such loss mechanism: the action of radio waves generated by terrestrial lightning through a resonant scattering process known as *Lightning-induced Electron Precipitation* (LEP), and examines the regions of the space environment in which losses due to LEP may be substantial. We perform this study through extensive numerical simulation of single LEP events, under a variety of space weather conditions, and examine global trends by extrapolating over a global lightning activity dataset.

1.2 Motivation

1.2.1 The Radiation Belts

The Van Allen radiation belts, first measured in 1958 by *Van Allen* (1958) on the Explorer I and III satellites, represent one of the earliest major discoveries of the American space program. The belts are an enhancement in very-high-energy particles ($E > 100$ keV), which extend from 1.2 to 7 earth radii along the equator, and follow the Earth’s magnetic field to $\sim \pm 65^\circ$ latitude (*Walt*, 1994). While the location and population of the belts are highly dynamic, it is customary to divide the population of

high-energy particles into two toroidal shells: an inner belt below ~ 3 Earth radii; an outer belt between ~ 3 and 7 Earth radii; and a ‘slot’ depletion region between 2 and 3 Earth radii. The radiation belts are dominantly populated by electrons (e^-) and Hydrogen ions (H^+). Geomagnetically-trapped particles are confined by the Earth’s magnetic field, and exhibit a helical bouncing motion, reflecting between fixed points near the northern and southern poles.

It was recognized early on that the ionizing effects of high-energy electrons represented a hazard for both humans and electronics in space. The Apollo manned spaceflight missions dealt with the risk of ionizing radiation both by incorporating additional aluminum shielding, and by designing their orbit trajectory to minimize time spent in the Van Allen belts (*English et al.*, 1973). Astronauts aboard the International Space Station wear passive dosimeters to measure total exposure; furthermore, the ISS includes radiation-safe regions which are better-shielded to the space environment, for use in cases of extreme solar or geomagnetic activity (?).

As silicon gate sizes continue to shrink, electronics have become increasingly susceptible to radiation-related failures. Single-event upsets (SEU) can occur when a high-energy particle impinges on a volatile memory circuit, imparting enough energy to erroneously change a bit from 0 to 1, or 1 to 0. The effects of SEU can be mitigated through specialized design practices, including triple-redundant systems and larger gate sizes, and are regarded as ‘soft’ failures from which a system can be designed to survive. Of additional risk are catastrophic failure events – for instance, in which an energetic particle can impinge on the oxide layer of a FET transistor, and create an electrical short, either temporary or permanent. Such an event can render spaceborne electronics useless.

1.2.2 Sources and Loss Processes

The radiation belts are generally populated by the stream of particles arriving from the solar wind, which provides a steady flow of cold electrons (velocities ~ 300 km/sec, and temperatures $\sim 10^{-5}$ Kelvin) (*Montgomery et al.*, 1974; ?). These particles are then gradually accelerated to relativistic energies through a variety of acceleration

processes within the magnetosphere, (itself a very open research topic) such as resonant interactions with ULF waves, chorus waves, and magnetotail processes (*Shprits et al.*, 2006; *Bortnik and Thorne*, 2007; *Thorne et al.*, 2013).

The dynamics of the radiation belts are marked with periodic filling events, in which the distribution of high-energy particles rapidly increase *Baker et al.* (2014). In the absence of other interactions, these particles would remain trapped by the Earth's magnetic field, and populations would continue to increase indefinitely. However the influx of new particles is balanced by an equally-complex set of loss processes.

Throughout the 1960s and 1970s, a wealth of research was performed on the lifetime of energetic radiation belt particles, most notably through a series of atmospheric nuclear experiments known as the *Starfish* project¹. *Starfish* was a 1.4 megaton nuclear device, detonated 400 km above Johnson Island on July 9, 1962, which provided an artificial, local enhancement to the inner radiation belt, at approx 1.2 Earth radii (*Hess*, 1963). Data from particle detectors aboard several early satellites (Telstar, Injun, Ariel, and Tracc) were then used to study the lifetime of energetic protons and electrons. *Starfish* electrons were found to be very long-lived, with lifetimes on the order of ~ 2 years (*Beall et al.*, 1967). In the months following the *Starfish* detonation, seven satellites, (including Telstar 1, the first commercial communications satellite, launched one day after the *Starfish* detonation) experienced catastrophic failures (*Wenaas*, 1978; *Barth et al.*, 2003; *Conrad et al.*, 2010), inspiring a decades-long research interest in the lifetime of radiation belt particles, and anthropogenic techniques for the mitigation of nuclear-injected particles.

The earliest loss-mechanism theories considered Compton scattering against the nuclei of atmospheric neutral constituents (*Walt*, 1964). This model showed reasonable agreement with *Starfish* particles at the lowest altitudes (~ 1.1 Earth radii), but greatly overestimated particle lifetimes for the majority of inner-belt electrons, indicating that other, unaccounted-for loss processes must be present.

¹While the *Starfish* detonation was the greatest yield and highest-altitude, and thus of the greatest interest in radiation belt physics, it was not by far an isolated event. Between 1955 and 1962, with a lapse following an international armistice between 1958 and 1961, the United States performed twelve atmospheric nuclear tests, at altitudes ranging from 6 to 540 kilometers, with yields in the kiloton range, reaching a maximum with *Starfish* at 1.4 megatons. Simultaneously, between 1961 and 1962, the Soviet Union performed five high-altitude detonations between 1.2 and 300 kilotons.

1.3 Previous Work

1.3.1 Wave-Particle Interactions

Recognizing the need for additional loss mechanisms, It was soon theorized that resonant interactions with radio waves could significantly alter the reflection height of trapped particles, and in turn drive these particles further into the neutral atmosphere, where they stood a much higher chance of colliding with neutral constituents, and eventually precipitating into the neutral atmosphere. Unlike in free space, the charged medium of the plasmasphere allows propagation of only certain frequencies and modes of radio wave (see section ??). Right-hand, circularly-polarized waves in the VLF band ($\sim < 30$ kHz) are common in the plasmasphere, and arise from a variety of generation mechanisms. These waves are known as *whistlers*, named for the descending, whistle-like tones originating from distant, broadband impulses. Terrestrial lightning is a persistent source of whistlers, with ~ 50 flashes/sec occurring globally; each whistler can propagate through the magnetosphere and persist for several seconds. Within literature, whistler waves are often divided into two categories: “ducted” waves, which follow temporary enhancements in plasma density, with wavenormal vectors nearly parallel to the background magnetic field, and “magnetospherically reflecting” whistlers, which are not constrained to a duct, and generally have a much more-oblique wavenormal angle.

Figure 1.2 shows an example of a whistler wave and its causative lightning stroke. Whistler waves can also be generated naturally within the plasmasphere (*chorus* and *hiss*) or be induced via high energy, ground-based VLF transmitters (Graf, 2009). (It should be noted that whistlers are not the only category of waves relevant to the radiation belts – see the review paper by Thorne (2010) for an overview of various other waves).

The concept of lightning as a loss mechanism for radiation belt electrons was first proposed by Dungey (1963), and subsequently by Cornwall (1964), through resonant interactions with whistler-mode waves. Dungey provided order-of-magnitude

An international moratorium on high-altitude detonations took place in 1963 with the High Altitude Nuclear Test Ban Treaty (Hess, 1964; Schwelb, 1964; Hoerlin, 1976; Norris and Cochran, 1996).

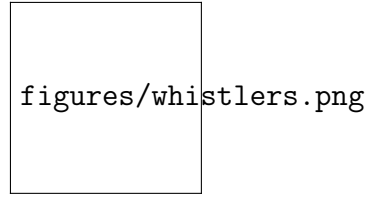


Figure 1.2: Write me pls

estimates for electron lifetimes, arguing for the significance of LEP in the inner radiation belt, and against for the outer radiation belt, and proposed an anthropogenic source of whistlers as a provisional loss mechanism in the event of further nuclear enhancements.

Shortly thereafter, *Kennel and Petschek* (1966), and subsequently *Lyons and Thorne* (1973), provided an alternative mathematical framework for the diffusion of radiation belt particles due to random-walk interactions with incoherent whistler mode waves known as *plasmaspheric hiss*. From here, studies of wave-induced precipitation mechanisms can be grouped into two categories: coherent studies (the “Liouville” approach), in which known particles are subjected to a known wave event, and incoherent studies (the “Fokker-Planck” approach), in which distributions of particles evolve through repeated, stochastic interactions with broadband radio wave activity.

1.3.2 LEP measurements

The first one-to-one measurements of precipitating electrons associated with causative whistlers were made by *Voss et al.* (1984), confirming the feasibility of LEP as a radiation belt loss mechanism. However, due to the sporadic nature of LEP and the dearth of space vehicles to measure it, one-to-one measurements of LEP are somewhat rare. LEP can be measured terrestrially across a great distance by examining the perturbations to VLF-band transmitter signals as they propagate in the waveguide formed by the Earth and the charged ionosphere. Additional charges imparted by LEP to the ionosphere can perturb this waveguide, and in turn affect the measured amplitude and phase of transmitted signals. These sporadic events (frequently known as “Trimpí” events, a nod to their discovery by *Helliwell et al.* (1973)), have

been studied for several decades (*Helliwell et al.*, 1973; *Carpenter et al.*, 1984; *Inan et al.*, 1988; *Burgess and Inan*, 1993). These works further confirm the existence and frequency of LEP events; however due to the nature of the waveguide sensing method, it is difficult to obtain direct electron flux estimates without substantial modeling.

1.3.3 Modeling of single LEP events

A substantial history of numerical modeling of LEP exists at Stanford, beginning with the thesis work of *Inan* (1977), who performed numerical simulations of pitch-angle scattering due to short-duration, monochromatic, ducted whistler waves. This work was then elaborated on throughout the 1980s in a series of test-particle simulations (?*Chang and Inan*, 1985; *Inan et al.*, 1989), which directly simulate the effect of whistler waves on discrete collections of electrons in the time domain.

Gyrorotation-averaged equations of motion for the interaction of waves and trapped particles were derived by *Bell* (1984). Combining the derivations of *Ristić Djurović et al.* (1992), the thesis work of *Ristić Djurović* (1993) and subsequently *Ristić Djurović et al.* (1998) provided a mathematical framework for the interaction of generic whistler waves and trapped particles, and demonstrated the relative importance of oblique wave interactions.

The thesis work and subsequent publications of *Lauben* (*Lauben*, 1998; *Lauben et al.*, 1999, 2001) represented a full numerical treatment of precipitation due to a single lightning stroke, combining test-particle simulations with a numerical raytracing scheme to estimate whistler wave intensity vs. location, frequency and time. The thesis work of *Bortnik* (2005) brought further detail to the simulation of LEP, again using a raytracing scheme, and incorporating (among others) Landau damping calculations and multiple resonant modes. The work of *Lauben* and *Bortnik* primarily differ in their treatment of the resonant interaction: *Lauben* uses a test-particle approach to track the change in particle pitch angles across long distances; *Bortnik* uses a hybrid coherent / incoherent scatter model, in which the coherent interactions of a collection of particles along a field line is considered independent from other locations and wave frequencies; the resulting resonant interaction is then summed in

quadrature across all frequencies and latitudes, to provide a pseudo-incoherent, RMS scattering approximation.

The wave-particle interaction model of *Bortnik* (2005); *Bortnik et al.* (2006) was then applied to narrowband, transmitter-generated waves by *Kulkarni* (2009) to examine the efficiency of spaceborne VLF transmitters as a remediation tool for radiation belt electrons; *Cotts* (2011) further expanded on the *Bortnik* model by incorporating the effects of atmospheric backscatter.

The work presented here in this thesis is based off of the original model from *Bortnik* (2005); however we provide several model improvements, including an elaborated treatment of the background plasma; a more-accurate model of variation along the longitudinal axis; and various practical code improvements.

1.3.4 Behavior of whistler waves in the magnetosphere

The study of LEP is complex, in that it requires study of both the interaction of particles and waves, as well as the behavior of the waves and particles before and after the interaction. [Ray tracing, landau damping histories here]

1.3.5 Electron lifetime estimates due to LEP

1.4 Scientific Contribution

1.5 Thesis Organization

This thesis is divided into the following chapters.

- Chapter 2 describes the background physics of the LEP process, the numerical methods used within this study, and the mathematical models of the various environments which we examine.
- Chapter 3 presents a study of the persistent VLF radio energy within the magnetosphere, resulting from terrestrial cloud-to-ground lightning discharges.

- Chapter ?? provides a simulation of electron precipitation resulting from a canonical cloud-to-ground lightning discharge, and a discussion of various model improvements, notably with our treatment of the longitudinal axis.
- Chapter 4 provides seasonal estimates of the global impact of LEP resulting from the GLD360 dataset and a reduced-complexity model.
- Chapter 5, admittedly a bit of a tangent, presents the design of a CubeSat-based instrumentation suite, designed for direct, *in-situ* measurements of LEP by taking time-and-space-coincident measurements of electron loss cone distributions, and incident VLF waves. The design provides some interesting on-board signal processing to reduce the data bandwidth significantly, and is implemented entirely in fixed-point logic using an FPGA (and *no* onboard CPU). I worked on this design in the earlier years of my time at Stanford; at time of writing it is due to be launched in early 2019.

Chapter 2

Background Physics and Description of Methods

2.1 Overview of Plasma Physics

A *plasma* is a quasi-neutral gas of ions, electrons, and neutral particles, which exhibit collective behavior. Plasmas can behave in similar ways to a conventional fluid – they can flow, they can be compressible, they can be turbulent, and so on – however the addition of charged particles facilitates many behaviors unique to a plasma. Charged particles can interact with each other not just through ballistic collisions, but at a distance through electromagnetic forces. The bulk motion of a plasma can be manipulated through electric and magnetic fields; conversely a plasma can have a substantial effect on the propagation of radio waves passing through it.

A plasma can be analyzed in several different domains: Single particle motion; fluid approximations; and full kinematic solutions. In this work we treat the motions of electrons in the single particle domain, which is a natural choice for the sparse densities and small gyroradii of radiation belt electrons. To understand the behavior of radio waves propagating through a plasma, we treat the background as a smooth dielectric medium.

2.1.1 Single Particle Motion

The high energies and sparse densities of the radiation belts lend themselves very well to a single-particle approximation. Many of the basic behaviors and quantities in plasma physics can be understood through studying the motion of a single particle.

The fundamental equation of motion for a charged particle in an electromagnetic field is given by the Lorentz force:

$$\mathbf{F} = \frac{d\mathbf{p}}{dt} = q(\mathbf{E} + \mathbf{v} \times \mathbf{B}) \quad (2.1)$$

Where q represents the particle's charge, \mathbf{E} and \mathbf{B} represent the electric and magnetic fields, and \mathbf{v} the particle's velocity, shown here in a non-relativistic frame.

Electric fields simply apply a force in the direction of the field. However, note that a cross product is perpendicular to both terms – therefore any forces induced by the magnetic field will be perpendicular to the particle's velocity. The magnetic field is a *conservative* force, in that a stationary magnetic field cannot directly impart energy into a particle, but can alter a particle's trajectory. The particle will therefore have a net drift in the direction of the electric field, while exhibiting a helical motion around the magnetic field.

We can then split the velocity vector into two quantities – v_{\parallel} parallel to the magnetic field, and v_{\perp} perpendicular to the magnetic field. Two characteristic values arise from this motion: the radius of the particle's rotation around the magnetic field, known as the *gyroradius* or the *Larmor radius*:

$$r_l = \frac{mv_{\perp}}{qB} \quad [\text{m}] \quad (2.2)$$

and the rotation frequency, known as the *gyrofrequency* or *cyclotron frequency*:

$$\omega_c = \frac{v_{\perp}}{r_l} = \frac{qB}{m} \quad [\text{rad/sec}] \quad (2.3)$$

By integrating the particle's momentum over a single gyrorotation, we arrive at a third fundamental quantity known as the magnetic moment, or the *first adiabatic*

invariant:

$$\mu = \frac{mv_{\perp}^2}{2B} \quad (2.4)$$

In situations where the magnetic field varies slowly (e.g., on spatial scales much greater than the gyroradius), μ remains a constant of motion.

A final parameter to describe a particle's motion is its *pitch angle*, the angle between the velocities perpendicular and parallel to the magnetic field:

$$\alpha = \tan^{-1}\left(\frac{v_{\perp}}{v_{\parallel}}\right) \quad (2.5)$$

The first adiabatic invariant describes an implicit relationship between the magnetic field strength and a particle's pitch angle at a given point. Combining the first adiabatic invariant with conservation of kinetic energy, we can deduce an expression for magnetic trapping – that is, the magnetic field strength in which a particle exhibiting helical motion along a magnetic field line will turn around.

$$E = \frac{1}{2}mv^2 \quad (2.6)$$

$$= \frac{1}{2}m(v_{\parallel}^2 + v_{\perp}^2) \quad (2.7)$$

$$= \frac{1}{2}mv^2(\cos^2\alpha + \sin^2\alpha) \quad (2.8)$$

At a reflection point, the particle's kinetic energy will be entirely in the perpendicular mode:

$$\frac{v_{\perp 0}^2}{B_0} = \frac{v_{\perp 1}^2}{B_1} \quad (2.9)$$

$$\frac{v^2 \sin^2(\alpha)}{B_0} = \frac{v^2}{B_1} \quad (2.10)$$

$$\sin^2(\alpha) = \frac{B_0}{B_1} \quad (2.11)$$

A charged particle in a magnetic field will therefore be constrained to rotate around a field line, and feel an opposing longitudinal force as the field intensity increases.

If the magnetic field is such that there are two regions of increasing intensity, separated by a reasonable distance, the particle may bounce back and forth, reflecting at turning points given by equation 2.11. Such a field configuration is known as a “magnetic bottle” particle trap, as shown in figure 2.1. A key observation is that the reflection point is independent of energy, and depends only on the ratio of magnetic field strengths and the particle’s initial pitch angle.

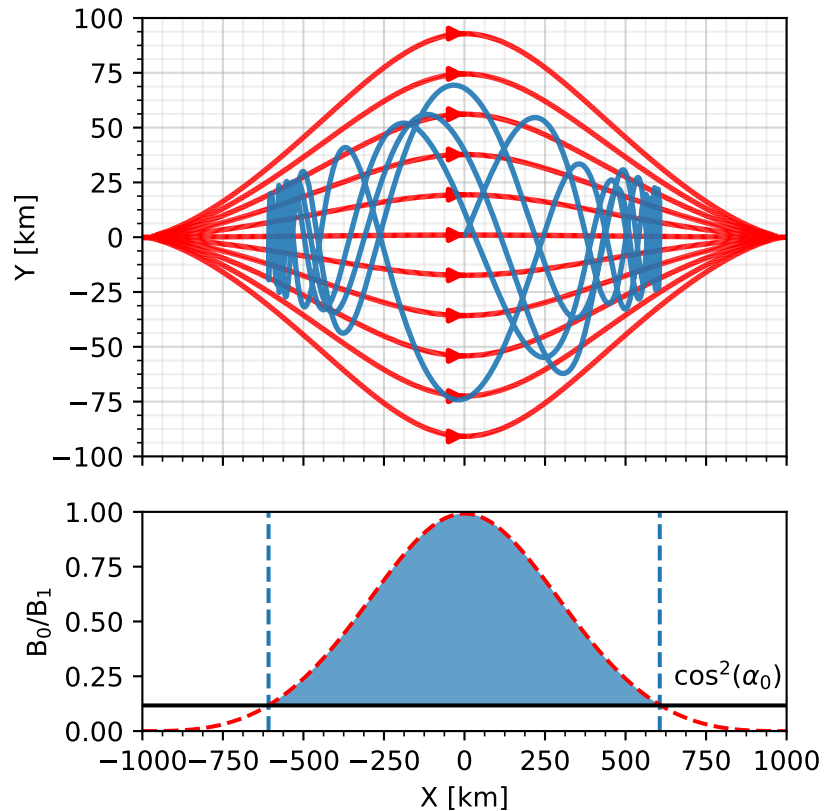


Figure 2.1: An example of a “magnetic bottle” particle trap. The top plot shows the trajectory of an electron with an initial pitch angle $\alpha_0 = 20^\circ$. The bottom plot shows the magnetic field ratio B_0/B_1 , with the particle’s reflection points shown as vertical lines.

2.1.2 The Loss Cone

A magnetic bottle trap need not be linearly-arranged, as it is in figure 2.1; we require only that the magnetic field be slowly-varying with respect to the particle's gyroradius. The Earth's dipole magnetic field forms a natural and effective particle trap, which dominates the morphology of charged particle populations surrounding the Earth. The motion of a charged particle in the Earth's magnetic field can be broken into three components (see figure 2.2):

- a rapid gyrorotation around the background magnetic field
- a “bouncing” motion between the north and south poles, with periods ranging from milliseconds to several seconds; and
- a slower, longitudinal drift, causing the particles to precess around the earth on the order of minutes to days, resulting from the magnetic field gradient

We can average the particle's motion over a single gyrorotation to define a *guiding center*, the trajectory of which follows the background magnetic field line.

As described previously, a trapped particle's reflection points are defined by the particle's initial pitch angle, and the strength of the magnetic field. In the case of the Earth, however, these turning points are limited in feasibility as well – for instance, a particle naturally cannot have a reflection point lower than the Earth's surface. Moreover, the Earth's neutral atmosphere becomes exponentially more-dense with decreasing altitude; particles reflecting at an altitude below ≈ 100 km will encounter a significant neutral molecule population, and stand a very good chance of colliding. A collision with atmospheric constituents can result in the particle losing some, or all, of its kinetic energy through ionization, and may be completely lost from the system, or return onto a different fieldline, with a different energy and/or pitch angle (Cotts, 2011).

With an understanding of the dense neutral atmosphere, we can define a critical altitude – 100 km here and in previous work – and thus a critical pitch angle, known

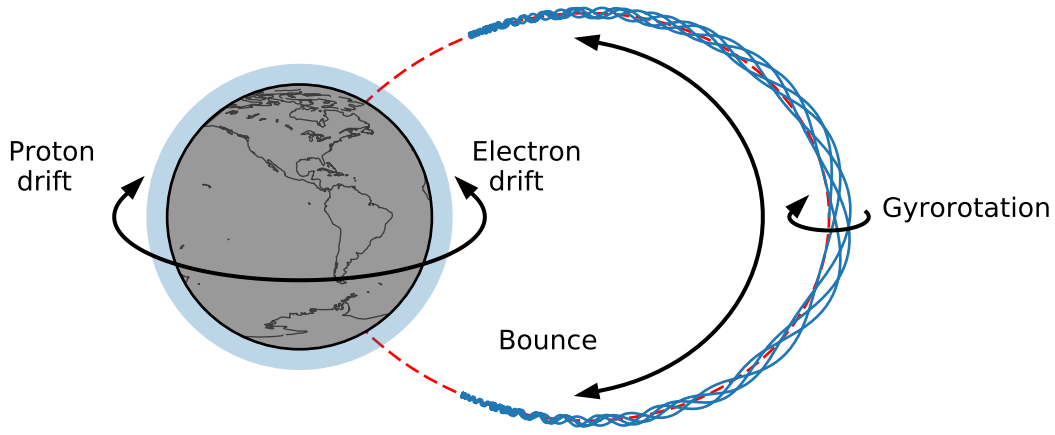


Figure 2.2: Illustration of the various motions exhibited by a charged particle in the Earth’s magnetic field

as the (bounce) *loss-cone angle*:

$$\sin \alpha_{lc} = \sqrt{\frac{B(\mathbf{r})}{B_{h_m}}} \quad (2.12)$$

where h_m is the reflection height, and $B(\mathbf{r})$ is measured at the reference point – either the particle’s current location for a *local loss cone angle*, or at the equator along the field line for the *equatorial loss cone angle*.

In the case of a dipole magnetic field model, we can determine the equatorial loss cone explicitly:

$$\sin \alpha_{lc} = \sqrt{\frac{\zeta_m^3}{\sqrt{1 + 3(1 - \zeta_m)}}} \quad \zeta_m = (R_e + h_m)/(LR_e) \quad (2.13)$$

where $R_e = 6371$ km is the radius of the Earth, and L is the *L-shell* of interest (see

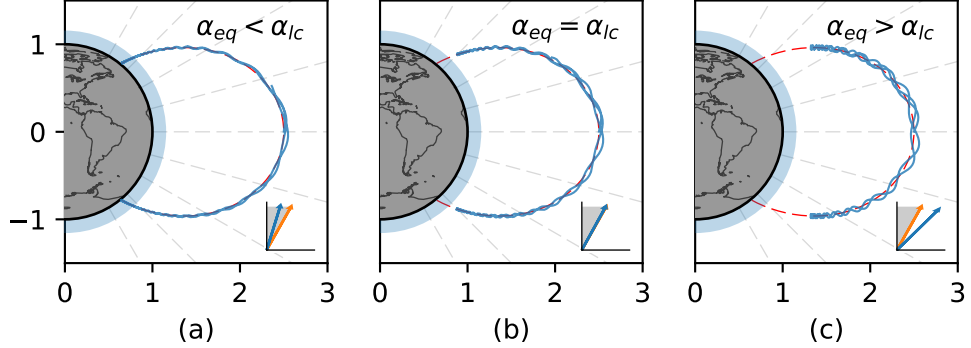


Figure 2.3: An illustration of the loss cone. The trajectory of a test electron is shown in blue, for three different equatorial pitch angles: (a) a precipitating particle with a pitch angle within the loss cone, (b) at the edge of the loss cone, and (c), a stably-trapped particle with a pitch angle well outside the loss cone.

section 2.4.1).

Bounce and Drift Loss Cones We have discussed what is known as the *bounce loss cone*. Also of interest in the study of the space environment is the *drift loss cone*. The drift loss cone is the largest loss cone along the same L-shell, as it varies longitudinally. Conceptually, as a particle drifts longitudinally, it may encounter a different loss cone, and could precipitate at certain longitudes, but not others. At some point along this longitudinal precession, the particle will encounter the maximum bounce loss cone, and precipitate (see *Cotts (2011)*, figure 2.3).

Under a simple dipole magnetic field model, the bounce loss cone is uniform around the globe, and the bounce and drift loss cones are identical. Within this dissertation, we primarily work with a dipole magnetic field model, and consider only the bounce loss cone.

2.1.3 Waves in Plasmas

Previously, we have described the motion of a charged particle under the influence of an electromagnetic field. the single-particle approximation provides enormous insight into the dynamics of a sparsely-populated plasma. Next, we must consider the corresponding case: how the charged particles in a plasma dictate the characteristic behaviors of an electromagnetic wave propagating through it.

An electromagnetic wave can accelerate a charged particle; conversely, an accelerating or decelerating particle induces its own electromagnetic field. It would seem, then, that the behavior of an electromagnetic field in a plasma is simply the summation of the contributions of each particle and some incident wave source. However, the complexity of this brute-force approach quickly becomes intractable for even a handful of particles. One common approach taken is to abstract the complicated interplay of waves and particles into a wave moving through a dielectric medium, described only by the various constituent densities, temperatures, and background fields within a given volume.

As with any electromagnetic problem, we begin with Maxwell's equations, shown here in their non-relativistic, differential form, in SI units:

$$\nabla \cdot \mathbf{E} = \frac{\rho}{\epsilon_0} \quad (2.14)$$

$$\nabla \cdot \mathbf{B} = 0 \quad (2.15)$$

$$\nabla \times \mathbf{E} = -\frac{\partial \mathbf{B}}{\partial t} \quad (2.16)$$

$$\nabla \times \mathbf{B} = \mu_0 \mathbf{J} + \frac{1}{c^2} \frac{\partial \mathbf{E}}{\partial t} \quad (2.17)$$

\mathbf{E} and \mathbf{B} denote the electric and magnetic fields; μ_0 and ϵ_0 denote the magnetic permeability and electric permittivity of free space; and $c = \sqrt{\frac{1}{\mu_0 \epsilon_0}}$ is the speed of light in vacuum. The terms ρ and \mathbf{J} represent the local charge density and current density, both of which may be functions of position and time.

By taking the curl of equation 2.16 and substituting in the time derivative of equation 2.17, and making use of the vector identity $\nabla \times \nabla \times \mathbf{E} = \nabla(\nabla \cdot \mathbf{E}) - \nabla^2 \mathbf{E}$,

we have:

$$\nabla^2 \mathbf{E} - \frac{\nabla \rho}{\epsilon_0} = \mu_0 \frac{\partial \mathbf{J}}{\partial t} + \frac{1}{c^2} \frac{\partial^2 \mathbf{E}}{\partial t^2} \quad (2.18)$$

In the absence of charges or currents ($\rho = 0, \partial \mathbf{J} / \partial t = 0$), the equation reduces to the free-space wave equation:

$$\nabla^2 \mathbf{E} = \frac{1}{c^2} \frac{\partial^2 \mathbf{E}}{\partial t^2} \quad (2.19)$$

Next, we search for harmonic perturbations of the form:

$$\mathbf{E}(\mathbf{r}, t) = \mathbf{E}_1 e^{i(\omega t - \mathbf{k} \cdot \mathbf{r})} \quad (2.20)$$

$$\mathbf{B}(\mathbf{r}, t) = \mathbf{B}_0 + \mathbf{B}_1 e^{i(\omega t - \mathbf{k} \cdot \mathbf{r})} \quad (2.21)$$

$$\mathbf{J}(\mathbf{r}, t) = \mathbf{J}_1 e^{i(\omega t - \mathbf{k} \cdot \mathbf{r})} \quad (2.22)$$

where ω is the wave angular frequency, \mathbf{k} is the wave vector, or spatial frequency, and \mathbf{r} is the spatial coordinate. Two fundamental parameters of an electromagnetic wave are the *phase velocity*, ω/k , and the *group velocity*, $\partial\omega/\partial k$. The relation between the temporal and spatial frequencies is known as the *dispersion relation*, expressible as either $\omega(k)$ or $k(\omega)$.

From here we follow the derivation and convention used by *Stix* (1992) and *Bitencourt* (2004). In general, a plasma is comprised of several different species of constituent particles – positively and negatively charged particles necessary to maintain a quasi-neutral plasma. While the dispersion relations of different species cannot be simply added, their effects can be summed to form the displacement current \mathbf{J} :

$$\mathbf{J} = \sum_s \mathbf{J}_s = \sum_s n_s q_s \mathbf{u}_s \quad (2.23)$$

where n , q , and \mathbf{u} represent the (number) density, charge, and velocity of a particular species s .

We make the assumption that the plasma is *cold* – that is, that all particles of a particular species are moving with the same velocity \mathbf{u}_s , with no thermal variation. Were we to relax this assumption, each species density would have a distribution

function in both position and momentum, $n = n(\mathbf{r}, \mathbf{p})$; the total current would then be an integration over momentum for each species. For a treatment of a hot plasma, see the work by *Sazhin* (1993).

Next, we note that, in a cold plasma assumption, the Lorentz force (equation 2.1) can be written for each species:

$$m_s \frac{d\mathbf{u}_s}{dt} = q_s (\mathbf{E} + \mathbf{u}_s \times \mathbf{B}) \quad (2.24)$$

Combining equations 2.20 – 2.22, 2.23, and 2.24, and assuming a coordinate system with the background magnetic field \mathbf{B}_0 aligned with the z-axis, we arrive at an expression for the *cold-plasma dielectric tensor*:

$$\boldsymbol{\epsilon} \cdot \mathbf{E} = \begin{pmatrix} S & -iD & 0 \\ iD & S & 0 \\ 0 & 0 & P \end{pmatrix} \begin{pmatrix} E_x \\ E_y \\ E_z \end{pmatrix} \quad (2.25)$$

The various summations over each constituent species are incorporated into the so-called Stix parameters (*Stix* (1992)):

$$S = \frac{1}{2}(R + L) \quad D = \frac{1}{2}(R - L) \quad (2.26)$$

$$R = 1 - \sum_s \frac{\omega_{ps}^2}{\omega(\omega + \omega_{cs})}; \quad L = 1 - \sum_s \frac{\omega_{ps}^2}{\omega(\omega - \omega_{cs})}; \quad P = 1 - \sum_s \frac{\omega_{ps}^2}{\omega^2} \quad (2.27)$$

where $\omega_{ps} = n_s q_s^2 / \epsilon_0 m_s$ and $\omega_{cs} = q_s B_0 / m_s$ are the plasma and cyclotron frequencies for species s .

Dispersion Relation

With the dielectric tensor now determined, we can derive the relationship between ω and \mathbf{k} , known as the dispersion relation. Equation 2.18 can be written as:

$$\boldsymbol{\eta} \times \boldsymbol{\eta} \times \mathbf{E} + \boldsymbol{\epsilon} \cdot \mathbf{E} = 0 \quad (2.28)$$

where $\eta = \mathbf{k}c/\omega$ is the wave refractive index. Assuming a wave propagating with some angle θ between η and the background magnetic field, we arrive at:

$$\begin{pmatrix} S - \eta^2 \cos^2 \theta & -iD & \eta^2 \cos \theta \sin \theta \\ iD & S - \eta^2 & 0 \\ \eta^2 \cos \theta \sin \theta & 0 & P - \eta^2 \sin^2 \theta \end{pmatrix} \begin{pmatrix} E_x \\ E_y \\ E_z \end{pmatrix} = 0 \quad (2.29)$$

Taking the determinant of 2.29 yields the *cold-plasma dispersion relation*:

$$A\eta^4 - B\eta^2 + C = 0 \quad (2.30)$$

$$A = S \sin^2 \theta + P \cos^2 \theta \quad (2.31)$$

$$B = RL \sin^2 \theta + PS(1 + \cos^2 \theta) \quad (2.32)$$

$$C = PRL \quad (2.33)$$

Equation 2.30 is biquadratic – we can solve for $\eta^2 = k^2 c^2 / \omega^2$ using the quadratic formula.

Finally, it is worth noting that when considering a single-species plasma (e.g., electrons only), equation 2.30 reduces to the well-known single-species *Appleton-Hartree Equation* (Appleton (1932)):

$$\eta^2 = 1 - \frac{\frac{\omega_{pe}^2}{\omega^2}}{1 - \frac{\omega_{ce}^2 \sin^2 \theta}{2(\omega^2 - \omega_{pe}^2)} \pm \left[\left(\frac{\omega_{ce}^2 \sin^2 \theta}{2(\omega^2 - \omega_{pe}^2)} \right)^2 + \frac{\omega_{ce}^2}{\omega^2} \cos^2 \theta \right]^{1/2}} \quad (2.34)$$

The dispersion relation in equation 2.30 reveals a wealth of information about the characteristics of waves in plasmas. For various plasma densities and background magnetic field strength, we can infer which wave frequencies may propagate, if any, and with which wave polarizations. Through the remainder of this work, we will be concerned with the *whistler* mode – a right-hand, circularly-polarized (RHCP) wave. Within a typical magnetospheric plasma, the whistler mode spans the VLF band, roughly between 30 Hz and 300 kHz.

It is difficult to gain much insight directly from the dispersion relation (equations 2.30 or 2.34). However, we can plot the spatial vs temporal frequencies for a fixed angle with respect to the background magnetic field, known as an ω - k diagram, to reveal the various modes of propagation.

Figure 2.4 shows a typical dispersion relation for a magnetospheric plasma ($L \approx 2$) by plotting frequency vs wavenumber ($\eta = kc/\omega$). The whistler mode is the lower branch of the RHCP mode.

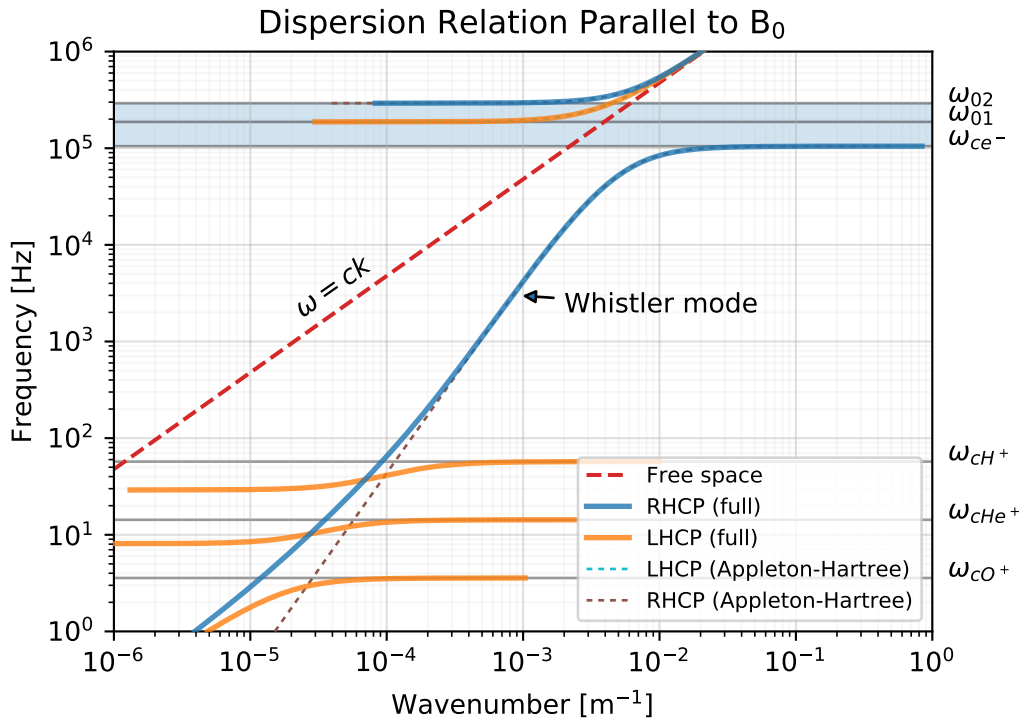


Figure 2.4: An ω - K diagram for the cold plasma dispersion relation, shown here for a wave propagating parallel to \mathbf{B} , in four-component plasma with $N_e \approx 6 \times 10^8 e^-/m^3$, and $B \approx 4 \mu T$. For higher frequencies the dispersion relation asymptotes to the free-space solution, with slope c . The whistler mode is the right-hand, circularly-polarized mode which spans the majority of the frequency band. The shaded region marks the characteristic band in which the right-hand mode cannot propagate. At lower frequencies, the left-hand circular mode resonates with the various ion constituents, known as the *Ion Cyclotron* modes.

2.2 Lightning Illumination Model

A single lightning flash is a stochastic dielectric breakdown process. While a terrestrial lightning flash consists of several repeated strokes at varying incident angles, we adopt the simplified model used by *Lauben* (1998), *Bortnik* (2005), and subsequent workers, and encapsulate the entire discharge process in a single return stroke.

The lightning flash is modeled as a single, vertical current pulse from a height H_E , with a double-exponential time profile given by equation 2.35. The double-exponential current profile is simple and common in the literature, originating with *Bruce and Golde* (1941):

$$I(t) = I_0(e^{-at} - e^{-bt}) \quad (2.35)$$

We relate the time-domain current profile to radiated power using the far-field approximation for an arbitrary source, given by *Griffiths* (1999), page 457:

$$S(t) \frac{1}{\mu_0} (\mathbf{E} \times \mathbf{B}) = \frac{\mu_0}{16\pi^2 c} \left[\frac{d^2 p(t)}{dt^2} \right]^2 \left(\frac{\sin^2 \theta}{r^2} \right) \hat{\mathbf{r}} \quad (2.36)$$

where $p(t)$ is the dipole moment given by $p = 2H_E \int_0^t I(t) dt$, r is the distance from the flash in meters, and θ is the angle to the flash. Taking the second derivative of the dipole moment (the first derivative of the current profile) gives us the far-field time-domain power equation:

$$S(t) = \frac{1}{Z_0} \left(\frac{\mu_0 H_E I_0}{2\pi} \right)^2 \left(\frac{\sin^2 \theta}{r^2} \right) (ae^{-at} - be^{-bt})^2 \hat{\mathbf{r}} \quad (2.37)$$

where we have used the relation $Z_0 = \mu_0 c$. Equation 2.37 gives energy flux density in units of Watts per square meter ($J/m^2/\text{sec}$).

To determine the frequency spectrum of the radiated power, we take the Fourier transform of equation 2.37:

$$S(\omega) = \frac{1}{Z_0} \left(\frac{\mu_0 H_E I_0}{2\pi} \right)^2 \left(\frac{\sin^2 \theta}{r^2} \right) \frac{\omega^2(a-b)^2}{\pi(\omega^2 + a^2)(\omega^2 + b^2)} \hat{\mathbf{r}} \quad (2.38)$$

which gives spectral energy flux, in units of $J/m^2/\text{Hz}$.

Throughout this work we assume a flash height $H_e = 5$ km, and model parameters $a = 5 \times 10^3$ sec $^{-1}$ and $b = 1 \times 10^5$ sec $^{-1}$, resulting in a spectrum peaked at approximately 4 kHz; any lightning flash can then be parameterized solely by its peak current I_0 and its location on the surface of the Earth. Figure 2.5 shows the current profile and associated spectrum.

The total energy released in a single discharge is determined by integrating equation 2.37 over time and a half-sphere surface:

$$E = \int_{t=0}^{\infty} \int_{\phi=0}^{2\pi} \int_{\theta=0}^{\pi} S(t) r^2 \sin \theta d\theta d\phi dt \quad (2.39)$$

$$= \frac{1}{Z_0} \left(\frac{\mu_0}{2\pi} \right)^2 \frac{(a-b)^2}{2(a+b)} \frac{4\pi}{3} H_e^2 I_0^2 \quad (2.40)$$

$$\approx 1.9 \times 10^{-14} H_e^2 I_0^2 \quad [\text{Joules}] \quad (2.41)$$

2.3 The Ionosphere

The ionosphere, extending from ≈ 85 km to 1000 km, is the highly-variable transition region between the terrestrial neutral atmosphere and the sparse plasmas of the space environment. The relatively-sharp rise in electron density at the bottom of the ionosphere makes it highly-reflective within the VLF band, forming a waveguide between it and the conductive surface of the Earth. However, In studying LEP, we are primarily concerned with the fraction of energy which does not reflect, and instead propagates through the ionosphere and out into the plasmasphere.

2.3.1 Trans-Ionosphere Attenuation

The ionosphere is a region of high variability, and a significant factor in the LEP process. As discussed earlier, the majority of VLF energy emitted by a lightning flash propagates efficiently in the Earth-Ionosphere waveguide; however a fraction of emitted energy can propagate upwards through the ionosphere, where the wave

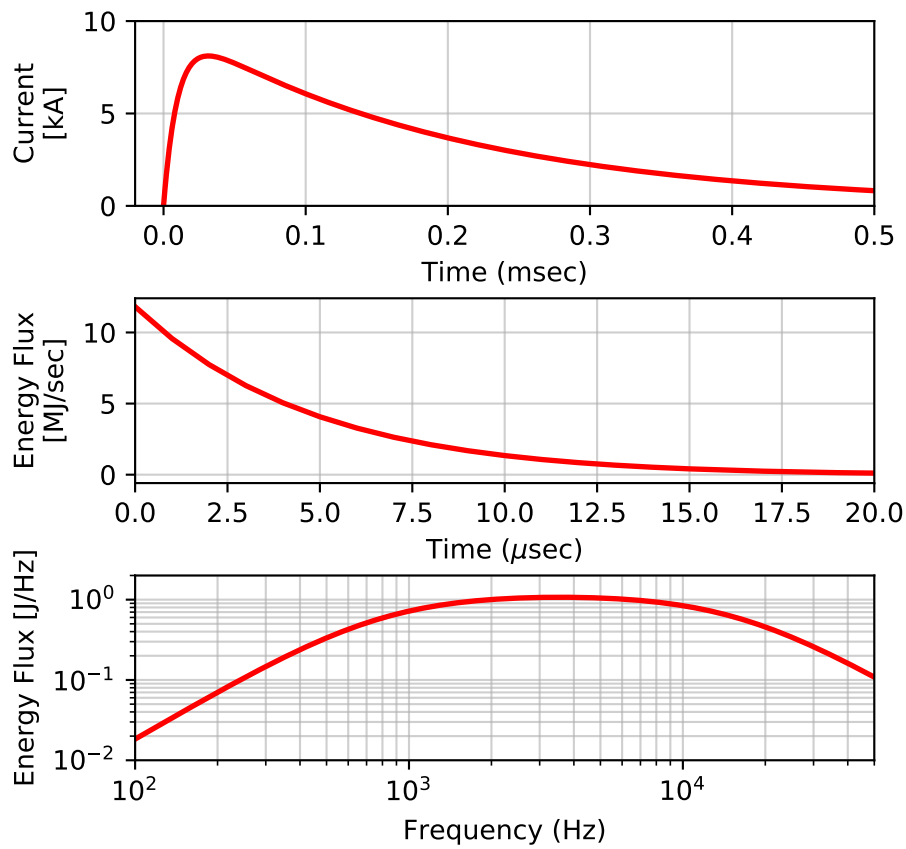


Figure 2.5: Double-exponential current pulse model of a lightning stroke. The top panel shows the stroke current vs time; the middle panel shows the total energy flux, integrated over space, vs time; the bottom panel shows the energy flux in the frequency domain.

experiences significant losses via Joule heating in the D-region ionosphere (*Graf*, 2009; *Blaes et al.*, 2016).

Propagation through the ionosphere can be studied using a raytracing approach; however the techniques required differ substantially from the raytracing implementation used in section 2.5. First, a key assumption in raytracing is that the background medium is smoothly-varying over each timestep (known as the WKB approximation ?). Maintaining this assumption requires different time steps and error bounds than within the plasmasphere, and would need to be computed separately. Second, the Landau calculations used to compute ray damping are designed for warm, but collisionless plasmas; the ionosphere is collisional, and only partially ionized, requiring different treatment.

Ionospheric propagation is further complicated by reflection and transmission at the lower boundary layer, as well as mode-coupling between incident plane waves, the whistler mode, and various others.

For computational simplicity, and to more-easily generalize to a variety of conditions, we treat the ionosphere as a single absorbing slab, ranging from 100 to 1000 km in altitude. We assume that waves propagate directly upwards (normal to the Earth’s surface), and are not deflected by ionospheric irregularities or the inclination of the background magnetic field.

Numerous researchers (*Lauben*, 1998; *Bortnik*, 2005; *Kulkarni*, 2009; *Graf*, 2009) have used the classic “Helliwell” curves, taken from *Helliwell* (1965), figure 3-35. Helliwell performs an analysis similar to Landau damping – first deriving a dispersion relation for a collisional plasma, then separating out the imaginary component, which will result in a real-valued attenuation term. The resulting attenuation term is dependent on electron density as a function of altitude, which was extrapolated from sounding rocket campaigns for day and night. The net attenuation is then computed by integrating from 65 to 1500 km in altitude.

Helliwell’s curves have persisted as the default record of trans-ionospheric attenuation; however it has been shown that Helliwell’s curves overestimate trans-ionosphere attenuation by 10 to 20 dB (*Starks et al.*, 2008), due mainly to the coarse measurement of the ionosphere electron density profile.

Rather than Helliwell's curves, we use results from *Graf* (2009), which are derived from extensive full-wave simulations using the International Reference Ionosphere (IRI) plasma density profile. Related work using the same full-wave model has been experimentally verified at \sim 20 kHz using DEMETER satellite measurements of VLF transmitters (*Cohen et al.*, 2012). *Graf* reports a set of curves in the same manner as Helliwell – power attenuation as a function of latitude, for two frequencies (2 kHz and 20 kHz), for dayside and nightside ionospheres. We then interpolate (or extrapolate) in log-space to find an attenuation factor for any latitude or frequency of interest ($\approx 10^\circ - 70^\circ$, and 200 Hz - 30 kHz).

We transition between the dayside and nightside attenuation curves using a Sigmoid function, with an approximate 1-hour transition width.

Figure 2.6 compares the *Graf* (2009) and *Helliwell* (1965) attenuation curves, which model the integrated wave power losses between 65 km - 1500 km altitude as a function of frequency and geomagnetic latitude. Both models exhibit similar trends – higher attenuation towards the equator, and higher attenuation on the dayside – however the Helliwell curves report significantly greater attenuation overall. We can attribute this due to the electron density profile used in their calculation.

2.3.2 Models of the Ionosphere

In general, our treatment of wave propagation in the ionosphere is abstracted using the method described in section 2.3.1. However, in raytracing through the plasmasphere, we require a smoothly-varying transition between the plasmasphere and ionosphere models. Here we discuss two models of ionosphere electron density.

IRI The International Reference Ionosphere (IRI) is a standard model of several key plasma parameters – electron density, electron and ion temperatures, ion composition, and so forth. IRI provides detailed outputs as a function of location, altitude, and local time. The GCPM plasma model (a comprehensive model of the plasmasphere, described in section 2.5) uses the IRI-2007 implementation (*Bilitza and Reinisch*, 2008); the simplified IRI model is derived from the IRI-2016 model (the most-current available version at time of writing).

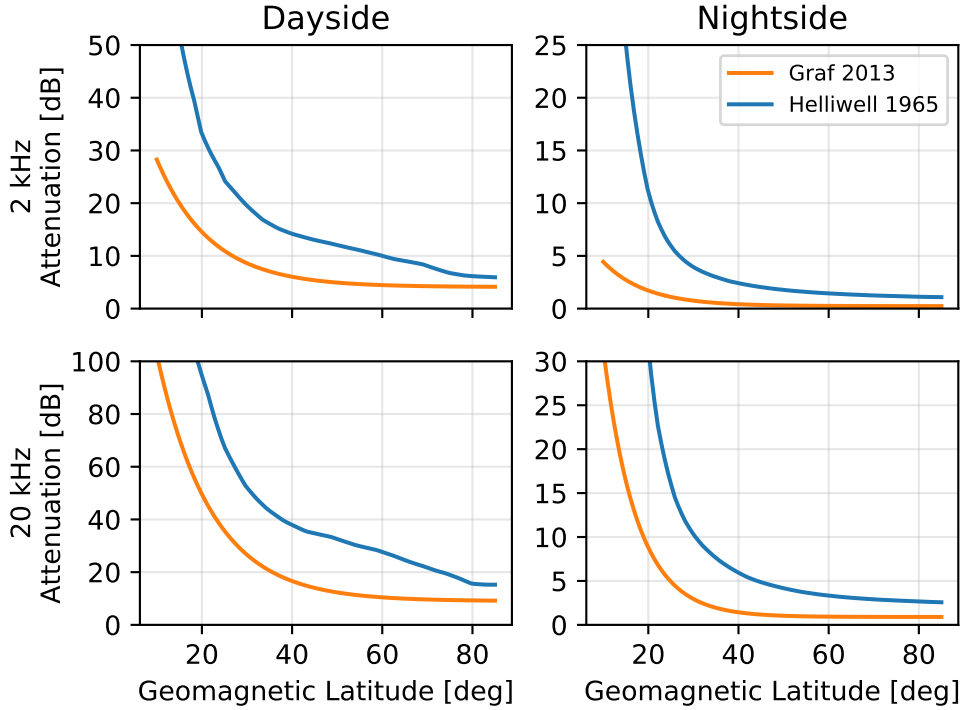


Figure 2.6: Trans-Ionosphere attenuation curves for the dayside and nightside, at 2 kHz and 20 kHz. Reproduced from *Graf* (2009), figure 7. The *Graf* curves show markedly less attenuation than the previously-used *Helliwell* curves, especially at equatorial latitudes, and on the day side.

Simplified IRI In order to both reduce our model parameter space, and to greatly decrease computation time, we pair a simplified version of IRI with a simplified version of GCPM. The IRI-2016 model was run for dayside and nightside ionospheres (12 and 0 MLT), using all default settings, for January 1st, 2000. We then fit a multiple-Gaussian function to the electron density vs latitude, at an altitude of 1500 km, and at the F_2 peak. Electron density variation with respect to altitude is approximated by a log-linear fit between 1500 km and the F_2 peak. Finally, longitudinal variation is smoothed with a sigmoid function with a width of ~ 1 hr. Figure 2.7 shows both the IRI electron density and the derived curve fits.

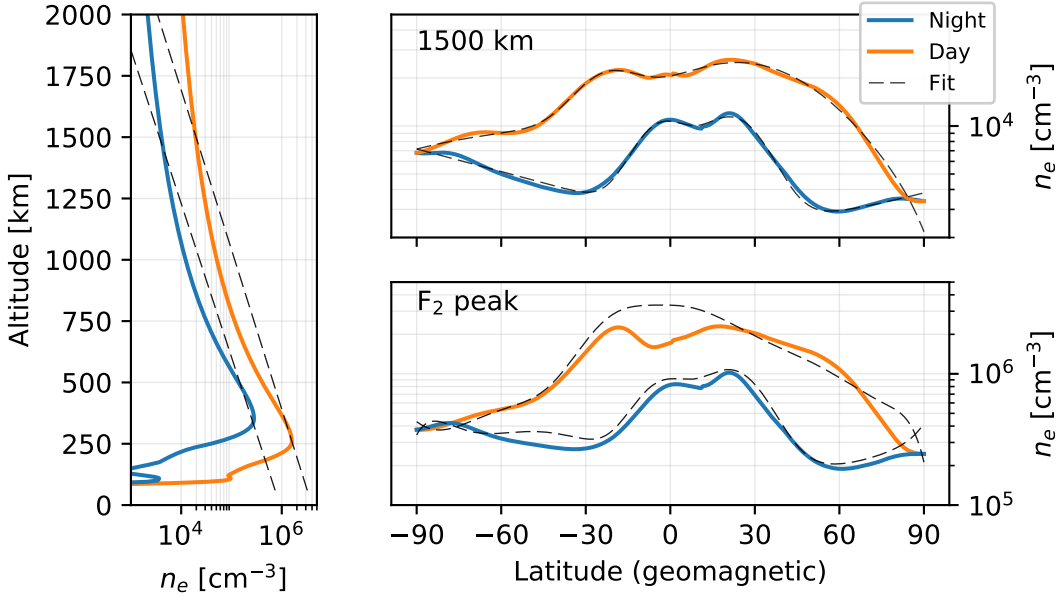


Figure 2.7: The IRI electron density model and derived curve fits. The left panel shows electron density variation as a function of altitude, for day and night. The right panels show electron density variation with respect to latitude, for (top) 1500 km and (bottom) the F_2 peak (approx. 300 km). Dashed lines indicate the fitted curves used by the simplified IRI model.

2.4 The Earth's magnetic field

The Earth's magnetic field dictates the morphology and natural coordinate systems used in studying the near-Earth space environment. Here we discuss three models of the Earth's magnetic field, with increasing complexity and realism.

2.4.1 Models of the magnetic field

Dipole To first order, the Earth's magnetic field can be approximated as a dipole, with origin at the Earth's center, and a tilt of $\approx 11^\circ$ from the axis of rotation. The dipole model, sometimes referred to as the “centered dipole” or “tilted dipole”, is reasonably accurate for midlatitude field measurements over the continental United

States, but can deviate significantly from the true field elsewhere. Similarly, the dipole field model is reasonably accurate for middle latitudes, below ≈ 10 Earth radii, but becomes increasingly inaccurate at higher latitudes, and at larger distances from the Earth, where the Earth's internal field is no longer dominant.

The dipole model, however, excels in its simplicity – the dipole magnetic field can be completely described in a closed form, and can be computed rapidly and reliably.

The magnetic dipole potential is given by:

$$\psi_{dip} = B_0 \left(\frac{R_e}{r} \right)^2 \cos \theta \quad (2.42)$$

The individual components of the magnetic field are given by the negative gradient of the scalar potential:

$$\mathbf{B} = -\nabla \psi \quad (2.43)$$

$$B_r = -2B_0 \left(\frac{R_e}{r} \right)^3 \cos \theta \quad (2.44)$$

$$B_\theta = -B_0 \left(\frac{R_e}{r} \right)^3 \sin \theta \quad (2.45)$$

$$B_\phi = 0 \quad (2.46)$$

Within this work we use $B_0 = 31.5 \mu\text{T}$ and $R_e = 6371 \text{ km}$.

A single fieldline, determined by integrating the direction of the field vector, can be described by it's *L-shell* – the fieldline's altitude, in units of Earth radii, measured at the equator.

For the dipole field, the radius of a field line at any latitude is related by:

$$R(\lambda) = R_e L \cos^2 \lambda \quad (2.47)$$

The dipole field can then be used as an orthogonal coordinate system, with any location being specified by a latitude, longitude, and L-shell (McIlwain, 1961).

Within the plasmasphere, the dipole model works well. However, closer to the

Earth's surface the model becomes increasingly inaccurate, necessitating a higher-order model.

IGRF The International Geomagnetic Reference Field (IGRF) is a 13th-order spherical expansion model, with coefficients updated every few years based on terrestrial measurements (*Thébault et al.*, 2015). Within this work we use the IGRF-12 model as a realistic representation of the Earth's internal magnetic field.

IGRF is quick and simple to calculate at any given location, and is much closer to reality than a simple dipole field. However, due to the added complexity, there are not closed-form expressions for field line trajectories or L-shells, which can make dealing with IGRF (and any higher-order model) more cumbersome.

Figure 2.9 contrasts lines of constant L-shell between the dipole and IGRF models.

Tsyganenko Corrections The dipole and IGRF models represent the Earth's internally-generated magnetic field. However, as one moves further away from the Earth ($L > \sim 8$), the Earth's internal field becomes less dominant, and external fields, namely forcing from the solar wind, cannot be ignored. The total field present in the space environment is the sum of both internal and external contributions.

Numerous models of the external field exist; within this work we consider the T05 external field model (*Tsyganenko and Sitnov*, 2005). The external field model exhibits seasonal and daily variation. However, for fieldlines below $L \approx 6$, the external field effects can be ignored.

Figure 2.8 contrasts the dipole, IGRF, and T05-corrected models in the meridional plane; Figure 2.9 illustrates the deviation in fieldline contours along the Earth's surface between the dipole and IGRF models.

2.5 The Plasmasphere

The plasmasphere is a region of the space environment surrounding the Earth, and a primary unknown within our modeling. The plasmasphere extends from the upper edge of the ionosphere (an altitude of 1000km) up to several Earth radii; typically

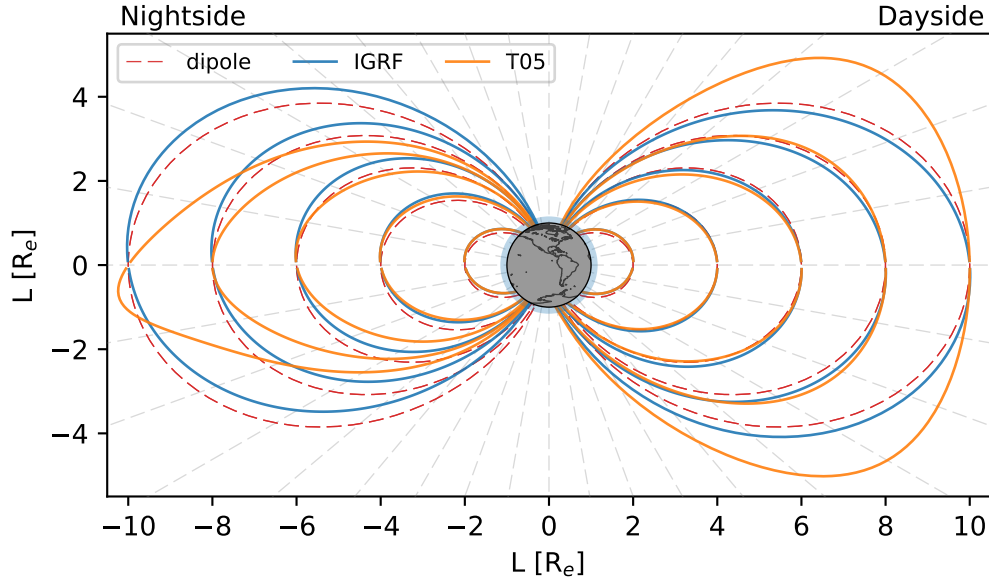


Figure 2.8: Three different magnetic field models, shown in the meridional plane, in geomagnetic coordinates: the tilted dipole, the IGRF model, and the Tsyganenko-Corrected IGRF model. Solar wind is incident on the right side.

it is divided into two separate regions: a dense, relatively cold *inner plasmasphere*, and a sparse, relatively hot *outer plasmasphere* or *trough*. The transition boundary between the two regions is a sharp dropoff in plasma density called the *plasmapause*. The location of the plasmapause varies with magnetic local time (MLT) and solar activity conditions, but generally occurs between $4 < L < 7$. Forcing on the sun side tends to bring the location closer to the Earth. Figure 2.11 shows the modeled location of the plasmapause as a function of K_p , a measurement of space weather activity. K_p is computed on a 3-hour period using ground-based measurements of local deviations from the background magnetic field. K_p can range from 0 (very quiet conditions) to 9 (extremely active conditions). Typically K_p is around 1 or 2. Figure 2.10 shows a distribution of K_p values.

Much like the ionosphere, the plasmasphere is a highly variable region, depending on geomagnetic conditions (K_p), location (latitude, longitude, field line), and time of day (MLT). The large spatial scales, high variability, and sparse availability of in-situ

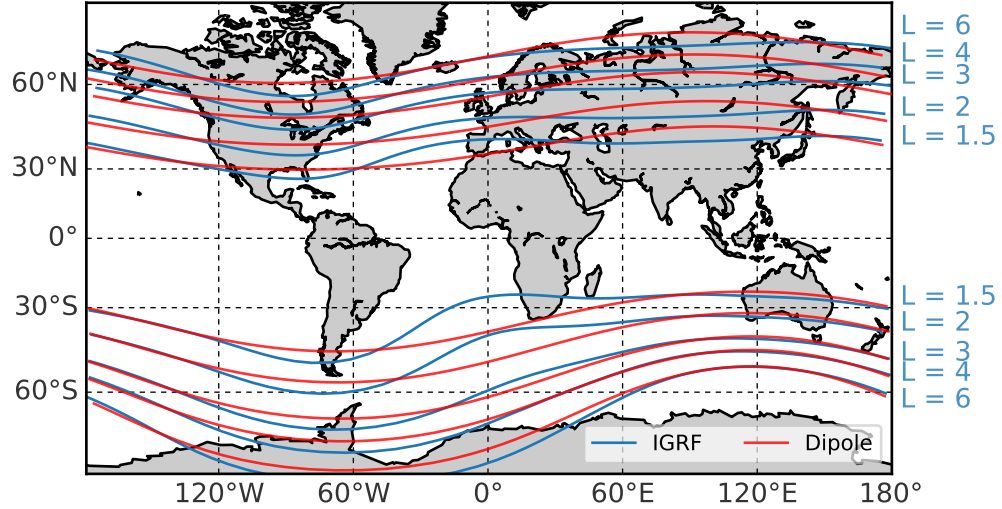


Figure 2.9: Fieldline contours along the Earth’s surface, shown for the dipole and IGRF models.

measurements require us to turn to empirical models of each region. We consider three primary models of electron and ion density.

Overview of Plasmasphere Density Models

Ngo Model The Ngo model is a legacy model used extensively in research at Stanford from the early 1980s through the mid-2000s, notably by *Lauben* (1998) and *Bortnik* (2005), and has heritage dating back to the early days of radiosciences at Stanford (*Kimura*, 1966). The model uses a Diffusive Equilibrium (DE) (*Angerami*, 1963) model for the inner and outer plasmasphere, onto which the *Carpenter and Anderson* (1992) inner plasmasphere model is overlaid. This model was integrated into the legacy Stanford VLF raytracing code, and provided several adjustable parameters, including plasmapause location, constituent ratios, and the ability to include ducts.

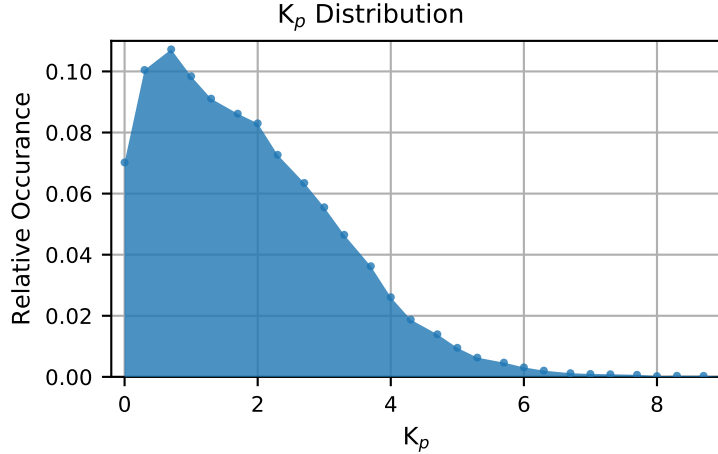


Figure 2.10: A histogram of K_p values, over a 5-year period between 2012 and 2017.

Global Core Plasmasphere Model (GCPM) The Global Core Plasmasphere Model, initially developed in 2000 by *Gallagher et al.* (1999) with significant updates through the following decade, smoothly transitions between several regional models to provide a continuous model of the plasmasphere. Within this work we use version 2.4, which was released in 2009 and made available by the Space Plasma Physics group at the NASA Marshall Space Flight Center (<https://plasmasphere.nasa.gov>). GCPM incorporates the *Carpenter and Anderson* (1992) inner plasmasphere model and the *Gallagher et al.* (1995) outer plasmasphere model, with an empirical fit of the plasmapause location between. The polar cap model is derived from *Persoon et al.* (1983) and *Chandler et al.* (1991). All models are connected smoothly to the IRI model of the ionosphere at lower altitudes. The combined GCPM model is parameterized by K_p and MLT.

Simplified GCPM GCPM aims to provide a dynamic, complete picture of the plasmasphere as a function of time and K_p ; however for our purposes GCPM provides too much variation. Additionally, the combination and smoothing between many models is computationally slow. In order to provide quicker computation and to reduce the number of parameters to adjust, we have implemented a simplified version

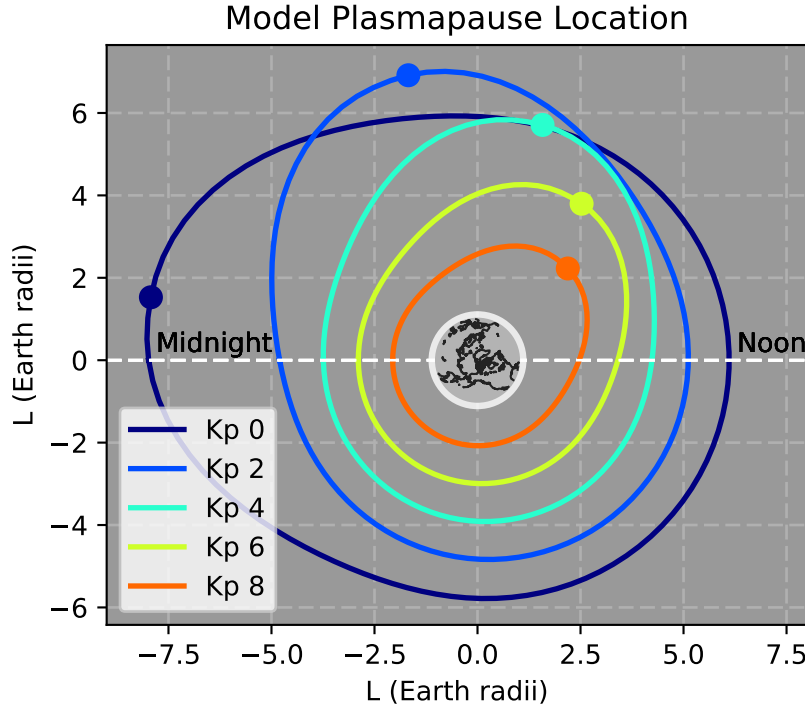


Figure 2.11: The *Gallagher et al.* (1999) model of the plasmapause location, as a function of K_p and magnetic local time.

of GCPM.

This model uses the equatorial-plane GCPM model, including the plasmapause location. However we omit any variation in electron density along latitude, and assume densities are constant along each field line. As our region of interest lies primarily within low and mid latitudes, we omit the polar cap model altogether and simply merge the ionosphere into the equatorial trough model. Finally to simplify computation, we model the ionosphere using an empirical fit to IRI – one for noon, and one for midnight, with a smooth transition along longitude. Figure 2.12 shows a side-by-side comparison of the three models, for $K_p = 2$.

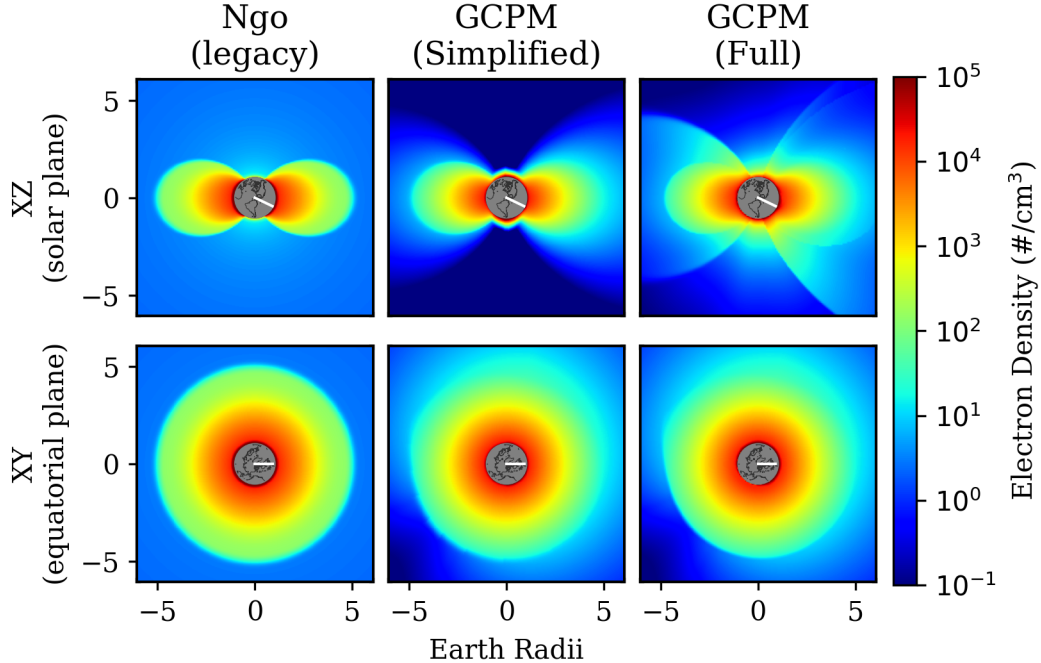


Figure 2.12: A comparison of three plasmasphere models: Ngo, simplified GCPM, and full GCPM, for a relatively quiet plasmasphere ($K_p = 2$). The top row shows electron density in-plane with the direction of solar influx; the bottom row shows a top down (equatorial cross-section) view. The white line indicates the solar axis. Only electron density is shown, as additional plasma constituents are derived from electron density.

2.5.1 Ray Tracing

Whistler-mode waves in the magnetosphere propagate for very large distances, and with relatively little attenuation. Under certain conditions, these waves can persist from a few seconds to 1 or more minutes. Simulating the propagation of these waves using a full-wave method would be extremely intractable with current computational resources. However we can use ray tracing to approximate their behavior.

Ray tracing is a technique from geometric optics which tracks the position and velocity of a coherent wave packet – essentially, approximate the behavior of a wave packet to that of a photon, and evaluate the packet’s group velocity and wavenormal vector with respect to time. Ray tracing is best suited for coherent, monochromatic

wave packets, with no attenuation, dispersion, or mode coupling.

Ray tracing was first applied to the whistler mode by *Haselgrove* (1954) using a graphical technique, then subsequently by *Haselgrove and Haselgrove* (1960) and *Kimura* (1966) for numerical computation. These papers worked in curvilinear coordinates with respect to a magnetic field line. Haselgrove's Equations have been used extensively by numerous magnetospheric scientists (*Kimura*, 1966; *Edgar*, 1972; *Ngo*, 1989; *RistićDjurović*, 1993; *Lauben*, 1998; *B.Peter*, 2007; *Bortnik*, 2005; *Kulkarni*, 2009), several using the so-called “Stanford Ray Tracing Program” – a legacy Fortran code which evaluated the Haselgrove equations in two dimensions. Our work uses a slightly different code originally developed by Dr. Forrest Foust (*Golden et al.*, 2010), and is designed for flexibility with respect to plasma density and magnetic field models. Rather than work in curvilinear coordinates with explicit derivatives, we adopt a more general formulation, using a three-dimensional Cartesian frame and numerically-evaluated derivatives.

We begin with the fundamental ray-tracing equations, as given by *Haselgrove and Haselgrove* (1960); *Stix* (1992):

$$\frac{d\mathbf{r}}{dt} = \frac{\nabla_k F}{\partial F / \partial \omega} \quad (2.48)$$

$$\frac{d\mathbf{k}}{dt} = \frac{\nabla_r F}{\partial F / \partial \omega} \quad (2.49)$$

constrained such that:

$$F = F(\mathbf{r}, t, \mathbf{k}, \omega) = 0 \quad (2.50)$$

Equation 2.48 is simply $\frac{\nabla_k F}{\partial F / \partial \omega} \approx \frac{\partial F / \partial k}{\partial F / \partial \omega} = \frac{\partial \omega}{\partial k} = v_g$, the group velocity of a wave packet. The corresponding equation describing the evolution of the wavenormal vector (2.49) is less intuitive, although an analogy can be drawn to Hamiltonian mechanics, in which ω represents a velocity, and k a momentum.

The function F , our “conserved quantity”, is simply the cold plasma dispersion relation given by equation 2.30.

The raytracing equations are a set of coupled, first-order differential equations; solutions to which require some subtlety, but can be addressed using standard numerical techniques.

First, note that we can solve the set at a given time, then evolve the system forward some finite time step. However, the constraint $F = 0$ may not be strictly held afterward. We assert that the error in this constraint must be small; which in turn implies that the background medium must be smoothly-varying (i.e., changing on a spatial scale much greater than our forward step and of the wavelength of interest). This assumption, known as the *WKB Approximation*, is fundamental to numerical methods for solving linear differential equations with spatially-varying coordinates ?.

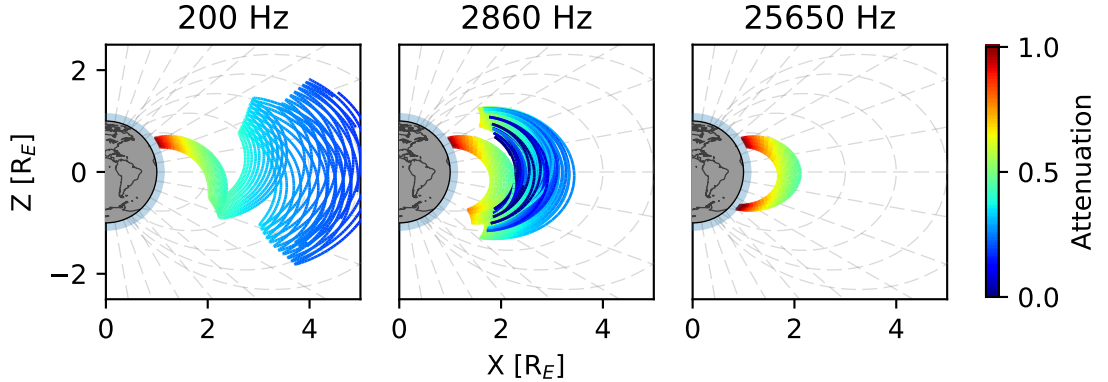


Figure 2.13: Example ray families as computed by the raytracer

Adaptive Timestepping

The process of raytracing, then, is to 1) solve the dispersion relation (2.30) to find the refractive index; 2) compute the velocity vector and step the system forward in time; and 3) re-evaluate at the new position to assure that the condition $F=0$ is satisfied. However, properly selecting the timestep is of critical importance – too large a timestep and positional errors will accumulate, or the ray will slip out of a propagating mode; too small and computational speed and memory usage suffers. We use an adaptive *Runge-Kutta-Fehlberg* (RK45) (Fehlberg, 1969; Mathews and Fink,

2004) method to continuously update the timestep as the raytracer progresses. RK45 is a common technique for solving ordinary differential equations.

The RK45 method approximates a solution with an initial stepsize dt using two spline fits: a fourth-order and a fifth-order. The error in the step is taken to be the difference between the two estimates. If the error is above a specified tolerance ϵ , the stepsize is reduced and the evaluation is repeated. Additionally, if the error is below a specified tolerance ($\epsilon/10$ in our implementation), the stepsize is increased. The result is a variable time axis with finer resolution in regions of high variability, while enabling longer timesteps in smooth regions for computational efficiency.

2.5.2 Landau Damping

The cold-plasma formulation of raytracing described above evaluates the trajectory and wavenormal angle of a wave packet. However, it assumes zero attenuation of wave energy. While it is possible to account for wave attenuation in ray tracing using warm plasma corrections (Sazhin, 1993; Henyey, 1980), we follow the same approximation as used in the legacy ray tracing code, and calculate attenuation along the cold-plasma raypath according to Landau damping.

Landau damping, originating in a seminal work by *Landau* (1946), is a resonant interaction between a wave and the distribution of electrons and ions comprising the background medium. The Landau mechanism is an interaction with parallel streaming particles and the wave's electric field. Resonant particles are accelerated or decelerated by the wave's electric field; if a majority of the resonant electrons have velocities slightly below that of the wave, then a coherent effect exists, the wavefront imparts some net energy to the plasma, and the wave is attenuated. Conversely, if the majority of resonant particles are moving faster than the wave, some of their energy can be imparted to the wavefront, inducing *wave growth* (Chen, 1983; Kulkarni, 2009).

Landau damping can have multiple resonances (in which the particle has multiple complete rotations per rotation of the wave). The lowest resonant mode is known as the *Landau* resonance, while the ± 1 modes are referred to as the *Cyclotron* resonances.

Higher-order modes remain nameless.

We use the expressions for Landau damping as formulated by *Brinca* (1972). *Brinca* derived expressions for Landau damping assuming a cold background plasma with a sparse warm distribution added, for whistler waves propagating at an arbitrary angle to the background magnetic field. Inputs to this formulation are the familiar Stix parameters (equations 2.26 - 2.27), which are in turn a function only of location and wave frequency; the wavenormal angle with respect to the background magnetic field; and a distribution function which specifies the energies (and thus velocities) of thermal electrons. The full set of Landau damping equations is given in Appendix A.1.

Interestingly, *Brinca*'s work was motivated by measurements of whistler-mode wave growth, rather than attenuation. Our implementation follows suit, and is equally capable of returning growth or damping, depending on the plasma model used. However, throughout this research, wave growth has been exceedingly rare.

Thermal electron distributions

The extent to which a wave is amplified or damped is heavily dependent on the energy distribution of background electrons. The energy distribution, or temperature profile, is specified as a normalized function in phase space – a function of position and velocity, which is normalized to 1:

$$f = f(\mathbf{r}, \mathbf{v}, t) \quad (2.51)$$

$$= f(\mathbf{r}, v_{\perp}, v_{\parallel}, t) \quad (2.52)$$

$$\int_0^{\infty} f dv_{\perp} = 1 \quad (2.53)$$

$$(2.54)$$

Two distribution functions are used in similar work – the *Bell* (2002) distribution, which was derived from POLAR spacecraft measurements of the inner plasmasphere,

and the *Bortnik et al.* (2007) distribution, which is based on CRRES spacecraft measurements above $L \approx 7$.

We use the phase space density function as described in *Golden et al.* (2010), which smoothly transitions between the *Bell* (2002) model inside the plasmapause, and the *Bortnik et al.* (2007) model outside the plasmapause. Figure 2.14 shows an example of the distribution function.

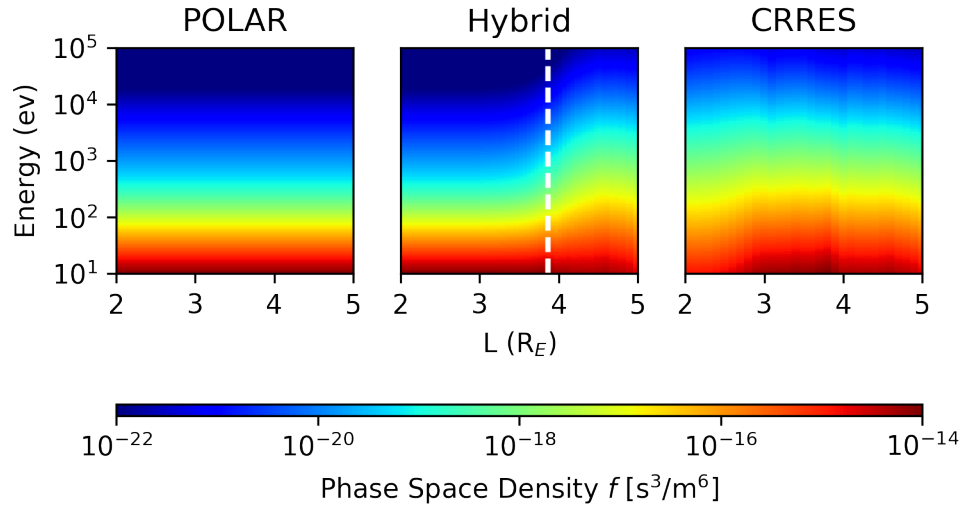


Figure 2.14: Example phase-space density functions, shown for $A_e=1.6$, $K_p=4$, $\alpha=45^\circ$, and $MLT=18$. The POLAR model is used inside the plasmapause, and the CRRES model outside the plasmapause. The hybrid model smoothly transitions between the two. The plasmapause, at $L \approx 4$, is marked by the dashed white line.

Figure 2.13 shows an example ray families, as computed using the above raytracing and Landau damping techniques. Each panel shows rays of a single frequency, launched from a range of latitudes. Higher frequency waves are more strongly deflected by the plasmasphere; for frequencies above $\sim 5\text{kHz}$, many of these waves are deflected strongly enough that they collide with the Earth without ever making a single turn. Lower frequency waves experience less deflection and can move further out into the plasmasphere, with the lowest frequencies propagating outward into space. Waves in between these two extremes ($\sim 1\text{kHz} - \sim 5\text{ kHz}$) are deflected

strongly enough to keep their energy close to the Earth, but not strongly enough as to lose their energy at the Earth’s surface, can bounce back and forth within the plasmasphere. These rays can persist for timescales up to several minutes before dissipating, and are prime candidates for wave-particle interactions.

2.6 The Radiation Belts

The term “Radiation Belts” or “Van Allen belts” refer to the trapped distributions of sparse, very-high-energy electrons, which exhibit two shell-like enhancements which comprise the inner and outer radiation belts. First measured in 1958 by Geiger counters aboard satellites 1958 α and 1958 γ of the Explorer program, the radiation belts were one of the earliest discoveries of the American space program (*Van Allen*, 1958). The vast majority of plasmasphere electrons are “cold”, and have kinetic energies well under ~ 1 eV. However, radiation belt electrons, while sparse in density, can be highly relativistic, with energies approaching 10 MeV.

Section 2.5 describes the density of electrons and ions in the near-Earth environment. Absent from these models, however, is a discussion of electron and ion energies. The model in section 2.5.2 assigns an energy distribution to electrons in the ~ 1 eV range to model a warm plasma; the higher energies of radiation belt electrons, however, necessitate a different model.

We model the trapped electron population using the AE8 density model (*Vette*, 1991). AE8 provides omnidirectional, integral fluxes of high-energy electrons as a function of L-shell energy. AE8 is the culmination of several decades of radiation belt studies by the National Space Science Data Center (NSSDC), with the first efforts originating with *Vette* (1966). AE8 combines measurements from ~ 94 different instruments across ~ 24 satellite missions from the 1960s and 1970s, which spanned a wide range of orbits, from LEO out to geostationary (*Cayton*, 2005).

Figure 2.15 shows the AE8 model output for minimally-populated and maximally-populated conditions.

The AE8 model reports omnidirectional, integral fluxes – that is, the total electron flux integrated over a spherical surface – at the geomagnetic equator. However we

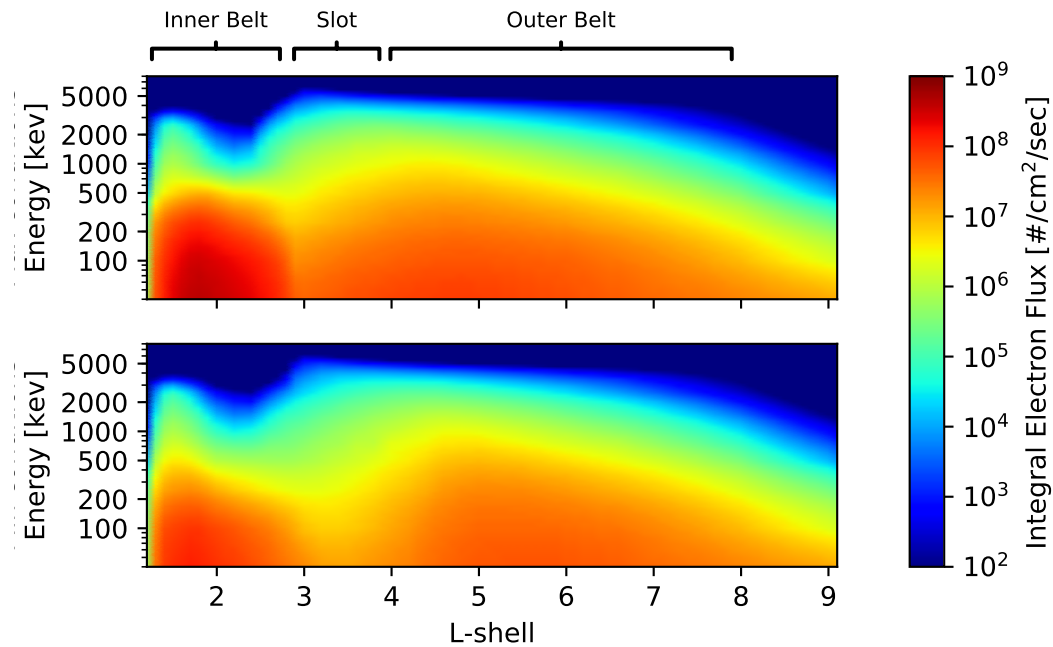


Figure 2.15: Integral flux for energetic electrons in the radiation belts, as reported by the AE8 model (*Vette*, 1991). The top frame shows the model of maximum conditions, and the bottom frame minimum conditions. The two radiation belts are visible as enhancements within $L \approx 2 - 3$ for the inner belt, and $L \approx 4 - 7$ for the outer belt. The belts are separated by a depletion known as the “slot” region.

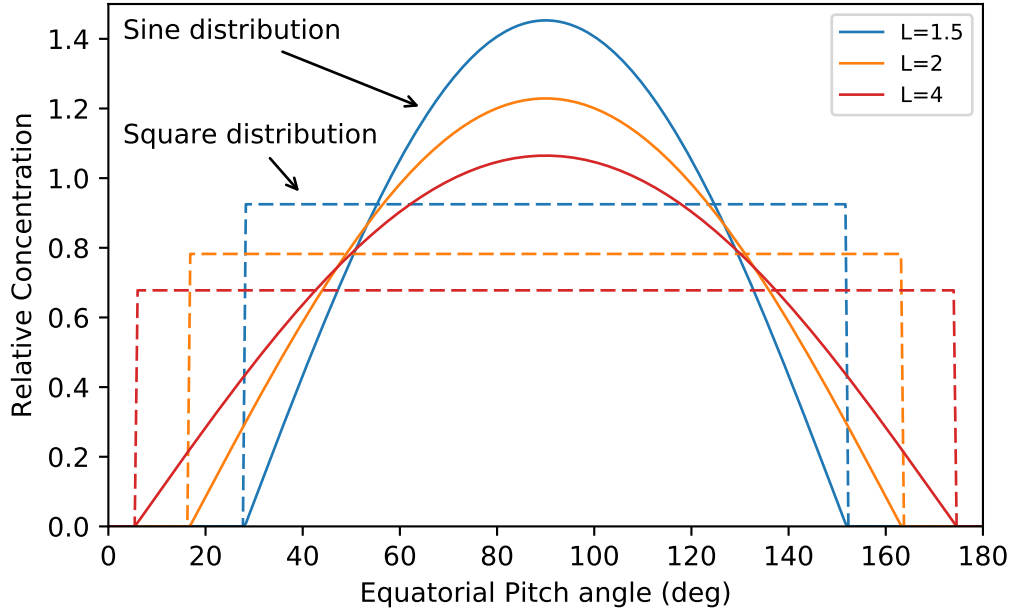


Figure 2.16: Two models of the distribution in pitch angle of radiation belt electrons. The simplest model is a square-shaped distribution, wherein pitch-angles are equally represented within the trapped population. A more realistic model is a sinusoidal distribution. Densities within the loss cone ($\alpha < \alpha_{lc}$) are assumed to be zero.

require finer detail in directional flux of electrons, which we model via a distribution of pitch angles. *Lauben* (1998) assumed the simplest distribution, with electrons uniformly-distributed in pitch angle up to the loss cone. *Bortnik* (2005) compared the square distribution to a more-realistic, sinusoidal distribution. Here we assume a sinusoidal pitch-angle distribution along with the AE8 flux density model. Figure 2.16 contrasts the square and sinusoidal distribution functions.

2.7 Wave-Particle Interactions

A trapped particle follows a fixed trajectory, bouncing indefinitely back and forth between its reflection points at the northern and southern hemispheres. The particle's local pitch angle varies with latitude; however in the absence of external interactions,

the pitch angle remains the same at each pass. For convenience, we can relate any local pitch angle back to the equatorial pitch angle through conservation of the first adiabatic invariant (2.4).

$$\sin^2 \alpha(\lambda) = \frac{B(\lambda)}{B_{eq}} \sin^2 \alpha_{eq} \quad (2.55)$$

A trapped particle's equatorial pitch angle remains a constant of the motion. However, it can be altered by means of a perturbation to the local magnetic field. Generally, small perturbations will be incoherent, and have negligible net effect on a particle's trajectory when compared to the background magnetic field. In the case of resonant wave-particle interactions, the particle's gyrorotation and the wave's magnetic field can be coherent, and have a significant effect on the particle's trajectory.

An essential characteristic of resonant wave-particle interactions is that while some energy can be imparted through the wave's electric field, no energy is exchanged through the magnetic field – rather, the perturbative effect of the wave magnetic field primarily shifts the particle's own kinetic energy between the parallel and perpendicular modes (v_{\parallel} , v_{\perp}).

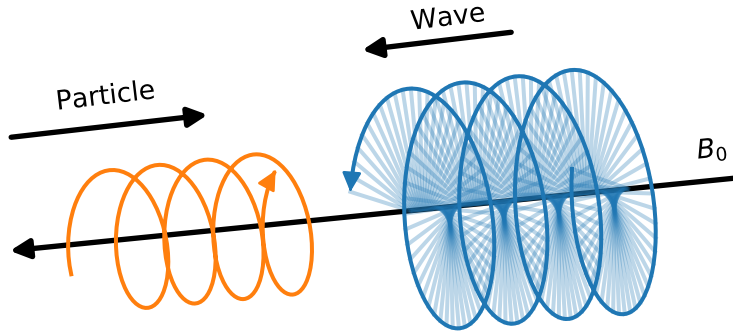


Figure 2.17: An illustration of a counter-streaming wave-particle interaction. At resonance, a gyrorotating particle sees an effective constant electric and magnetic field. Resonant interactions can occur in co-streaming (same direction) or counter-streaming (opposite direction) encounters.

2.7.1 Resonant Interactions

We begin by considering the resonant interaction between a monochromatic, elliptically-polarized wave, propagating obliquely (i.e., not strictly aligned with the background magnetic field). We can then calculate the resonant, doppler-shifted perturbative fields \mathbf{E}_w , \mathbf{B}_w , and calculate the change to a test particle's momentum using the relativistic Lorentz force. This analysis stems from *Bell* (1984), and has been used in numerous successive studies – *RistićDjurović* (1993); *Lauben* (1998); *Bortnik* (2005), and others.

The condition for resonance is given by *Chang and Inan* (1983):

$$\frac{d\eta}{dt} = \omega + v_z^{res} k_z - m\omega_c/\gamma \approx 0 \quad (2.56)$$

where η is the angle between the right-hand circular component of the wave magnetic field (B_r) and the resonant particle's perpendicular velocity vector (v_\perp), ω is the wave frequency, $m \in \mathbb{Z}$ is the resonance order, and $\gamma = (1 - (v^{res}/c)^2)^{-1/2}$ is the relativistic correction factor.

We use the *Bell* (1984) expression for change in pitch angle with respect to time, corrected for relativistic factors by *RistićDjurović* (1993); *Bortnik et al.* (2006):

$$\frac{d\alpha}{dt} = \frac{m_e \omega_{\tau m}^2}{k_z p_\perp} \left(1 + \frac{\cos^2 \alpha}{m \omega_c / \omega - 1} \right) \sin \eta + \frac{1}{m_e \gamma} \frac{p_\perp}{2\omega_c} \frac{\partial \omega_c}{\partial z} \quad (2.57)$$

with the following parameter definitions:

$$\beta = \frac{k_x p_\perp}{m_e \gamma \omega_c} \quad (2.58)$$

$$k_z = k \cos \theta = (\omega \mu / c) \cos \theta; \quad k_x = k \sin \theta \quad (2.59)$$

$$\omega_{\tau m}^2 = (-1)^{m-1} \omega_{\tau 0}^2 [J_{m-1}(\beta) - \alpha_1 J_{m+1}(\beta) + \gamma \alpha_2 J_m(\beta)] \quad (2.60)$$

$$\omega_{\tau 0} = \frac{\omega_1 k_z p_\perp}{\gamma m_e} \quad (2.61)$$

$$\omega_1 = \frac{e}{2m_e} (B_x^w + B_y^w); \quad \omega_2 = \frac{e}{2m_e} (B_x^w - B_y^w) \quad (2.62)$$

$$\alpha_1 = \frac{\omega_2}{\omega_1} \quad (2.63)$$

$$\alpha_2 = \frac{e E_z^w}{\omega_1 p_\perp} \quad (2.64)$$

$$R_1 = \frac{E_x^w + E_y^w}{B_x^w + B_y^w}; \quad R_2 = \frac{E_x^w - E_y^w}{B_x^w - B_y^w} \quad (2.65)$$

where e and m_e are the electron charge and rest mass, p_\perp is the perpendicular component of the particle's momentum, J_i are Bessel functions of the first kind, and $E_{x,y,z}^w$, $B_{x,y,z}^w$ are the vector components of the incident wave, oriented such that the z-component is parallel to the background magnetic field. The wavenormal angle (the angle between \mathbf{k} and the background magnetic field, taken to be along the z axis) is given by θ .

A full derivation of equations (2.57) - (2.65) is beyond the scope of this dissertation; however the full derivation is explained in the theses of *Bortnik* (2005), *RistićDjurović* (1993), and *Bell* (1984).

While the full set of equations (2.57) - (2.65) is complex, we can identify several broad trends: First, $\partial \alpha / \partial t \propto \sin \eta$, which implies that, when the resonance condition is not met, oscillating changes will have no cumulative effect. Second, $\partial \alpha / \partial t \propto \cos \alpha$, which increases the complexity of the solution space; however we can introduce a simplification by assuming that changes in pitch-angle are small, and therefore only particles with pitch angles very near the loss cone will be of significance.

2.7.2 Recovering Wave Amplitudes from Poynting Flux

Required in our modeling is the ability to link the results of raytracing to the wave-particle interaction model. However, raytracing tracks only coarse-grained wave parameters – wavenormal vector, propagation angle with respect to the background magnetic field, and the background plasma parameters. We use the formulation from *Bell* (1984), which has since been used by *RistićDjurović* (1993); *Lauben* (1998); *Bortnik et al.* (2006), to relate the Poynting flux and the individual wave components B_x^w, B_y^w, B_z^w .

Starting from the definition of Poynting flux $\mathbf{S}^w = (1/2)\text{Re}(\mathbf{E}^w \times \mathbf{H}^w)$, *Bell* (1984) finds a relation to a single magnetic field component, B_y^w :

$$\|B_y^w\| = \frac{2\mu_0\rho_2^2 X^2 \eta \cos \theta \|\mathbf{S}^w\|}{c\sqrt{(\tan \theta - \rho_1\rho_2 X)^2 + (1 + \rho_2^2 X)^2}} \quad (2.66)$$

$$X = \frac{P}{P - \eta^2 \sin^2 \theta} \quad (2.67)$$

$$\rho_1 = \frac{E_z^w}{E_y^w} = \frac{(\eta^2 - S)\eta^2 \sin \theta \cos \theta}{D(\eta^2 \sin^2 \theta - P)} \quad \rho_2 = \frac{E_x^w}{E_y^w} = \frac{\eta^2 - S}{D} \quad (2.68)$$

where ρ_1, ρ_2 are the wave polarization ratios, η is the wave refractive index, θ is the angle between the wavenormal and the background magnetic field, \mathbf{S}^w is the Poynting flux, and S, D , and P are the Stix parameters defined in (2.26) and (2.27).

The remaining five wave components are given by:

$$E_x^w = \frac{\|cB_y^w(P - \eta_x^2)\|}{P\eta_z} \quad (2.69)$$

$$E_y^w = \frac{\|E_x^w D\|}{S - \eta^2} \quad (2.70)$$

$$E_z^w = \frac{\|E_x^w \eta_x \eta_z\|}{\eta_x^2 - P} \quad (2.71)$$

$$B_x^w = \frac{\|E_x^w D \eta_z\|}{c(S - \eta^2)} \quad (2.72)$$

$$B_z^w = \frac{\|E_x^w D \eta_x\|}{c(X - \eta^2)} \quad (2.73)$$

2.8 The GLD360 Lightning Dataset

One could not study the global impact of LEP without a measurement of global lightning activity. Lightning is a persistent phenomenon, with an average of ~ 100 strokes per second globally at any given time of day or year (*Brooks*, 1925; *Orville and Spencer*, 1979).

Two primary techniques are used in the measurement of lightning distributions – optical / infrared detection from space, and geolocation techniques using surface measurements of the guided VLF emissions, or '*spherics*', which propagate in a waveguide-like manner between the Earth and the Ionosphere.

Early optical data measurements were performed in the 1970s by the U.S. Air Force, using the Defense Meteorological Satellite Program (DMSP) satellites, which served to reveal the global distribution of lightning – generally over land masses, and towards the equator. However, space-based optical techniques are limited to nighttime measurements, do not operate in real time, and must be performed amidst other parasitic light sources (*Orville*, 1995).

Surface-based radio detection of lightning has been in use as early as the 1920s, by magnetic direction finding (MDF) using crossed loop antennas (*Horner*, 1954, 1957). Such detection methods were primarily used for weather measurements before the advent of weather radar, and have seen use in early detection of forest fires (*Krider et al.*, 1980). Terrestrial measurements have an advantage in that they can operate during both daytime and nighttime, and have detection ranges on the order of hundreds of kilometers, due to the guided propagation of '*spherics*'.

Large-scale detection networks became available in the early 1990s, with the U.S. National Lightning Detection Network (NLDN). NLDN provides near-real-time measurements of lightning across the continental United States using a distributed array of 114 sensors in the VLF / LF (400 Hz - 400 kHz) range. NLDN reports cloud-to-ground detection efficiencies on the order of $\sim 90\%$ (*Nag et al.*, 2011).

Within the last decade, advances in processing techniques have fostered the ability to perform global lightning detection with a distributed array of sensors. We use the Global Lightning Dataset (GLD360), which uses a combination of time-of-arrival and

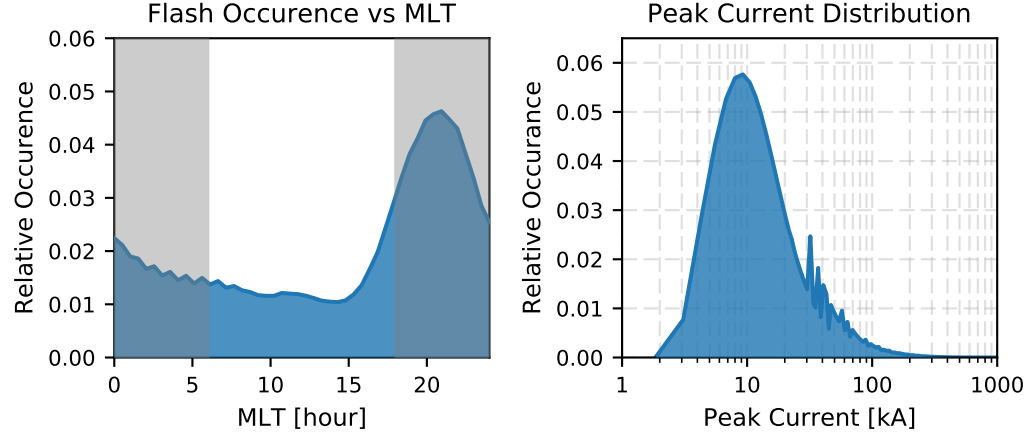


Figure 2.18: Histograms of MLT and peak current for the GLD360 dataset, shown for a period between August 2014 and April 2016. The grey shaded regions denote “nightside” flashes.

direction-finding techniques, along with a precomputed waveform bank, to achieve global cloud-to-ground detection ratios on the order of $\sim 60\%$ (*Said et al., 2010*). GLD360 is a commercial service operated by *Vaisala, inc..*

GLD360 parameterizes cloud-to-ground lightning discharges by their location (latitude, longitude), and their peak current, I_0 , as given in section 2.2. Figure 2.19 shows the annual flash rate density reported by GLD360 over a two-year period between August 2014 and April 2016; figure 2.20 shows the average squared current density (from equation (2.37), $S \propto I_0^2$). Figure 2.18 show the distribution of peak currents and time of day. Within this work we take the GLD360 dataset to be the ground truth measurement of global lightning activity.

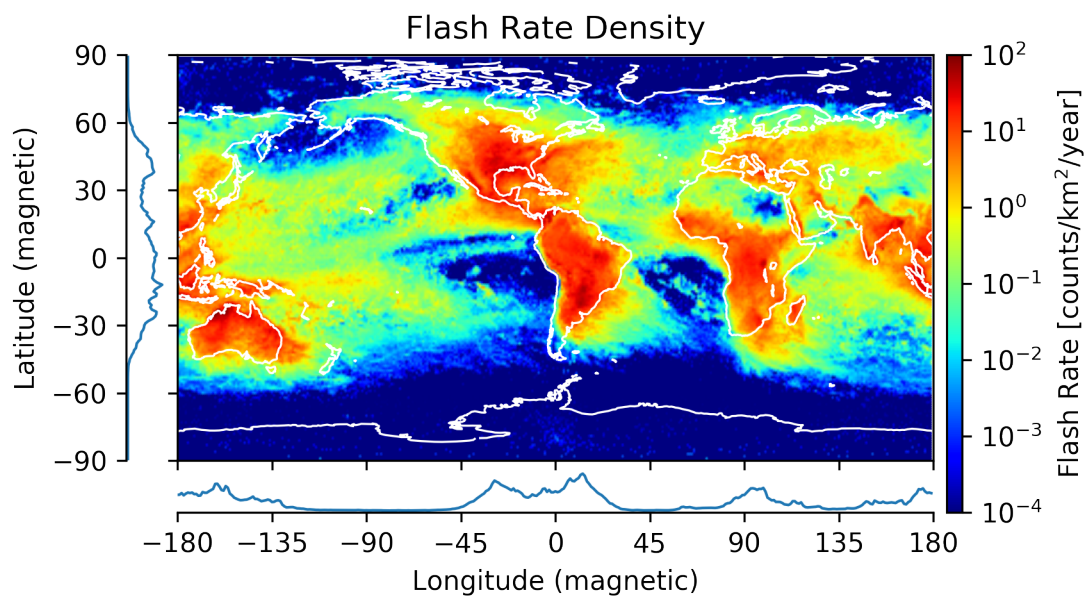


Figure 2.19: The average global flash rate distribution, as measured by the GLD360 sensor network, taken over a period between August 2014 and April 2016. The side plots show the relative density vs latitude and longitude.

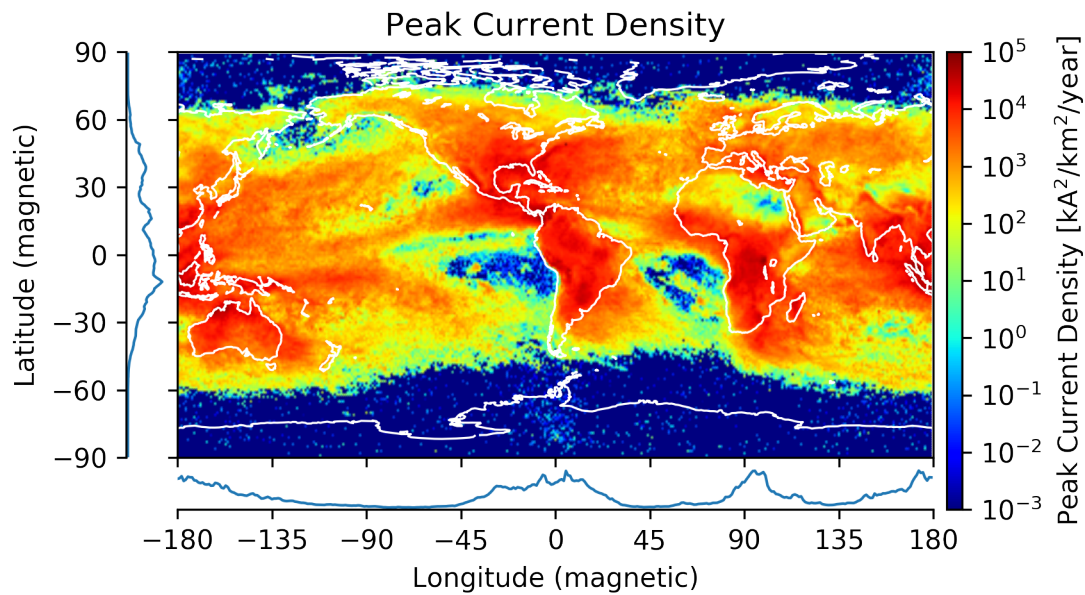


Figure 2.20: The average global peak current distribution, as measured by the GLD360 sensor network, taken over a period between August 2014 and April 2016. The side plots show the relative density vs latitude and longitude. While the morphology is similar to figure 2.19, scaling by the average peak current indicates a possible increase in energy over the oceans.

Chapter 3

VLF energy in the Near-Earth Environment

The purpose of this chapter is to provide a quantifiable assessment of the persistent radio wave energy in the near-Earth space environment due to lightning-generated whistlers. The morphology of LEP (time evolution, spatial extent at the Earth’s surface, and so forth) are primarily determined by the location of wave-particle interactions; additionally, wave-particle interactions with whistlers are hypothesized to be the primary cause of slot-region electron depletions, and the “impenetrable barrier” below $L \sim 2$.

Lightning-generated whistlers are sporadic, and exist alongside a multitude of radio wave activity, such as VLF chorus and plasmaspheric hiss, making a correlated *in-situ* measurement challenging. Within this chapter we simulate the relative VLF energy (L-shell, latitude, longitude) in the near-Earth space environment, in volumetric units [J/m^3], as a means of assessing their relative contribution to the persistent radio spectrum.

3.1 Methodology

Our simulation is divided into two portions: First, a simulation of persistent VLF energy due to a single flash originating at a fixed latitude, and second, an integration

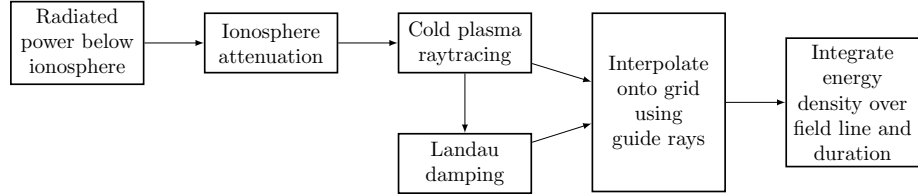


Figure 3.1: Block diagram of the average energy density calculation for a single flash.

over a measured lightning dataset, using scaled and shifted “stencils” for each flash.

3.2 Persistent Energy from a Single Flash

Figure 3.1 shows the steps required to compute the average energy imparted from a single lightning discharge. The resulting stencil has dimensions of L-shell and longitude.

1. First we model the sub-ionosphere power spectrum generated from a flash with a known peak current, using the methodology of section 2.2.
2. We then propagate the energies through the ionosphere, using the attenuating slab approximation method of section 2.3.1.
3. We map the time-integrated effective power above the ionosphere (J/m^2 at 1000 km altitude) to an energy density along a fixed grid using a set of pre-computed “guide rays” using the methodology in section 2.5, the Landau damping from section 2.5.2, and the novel interpolation scheme described below.
4. In order to account for multiple crossings at each grid point, and to reduce our output space across different latitudes, we store the time-averaged energy density along each field line.

3.2.1 Radiated power above the ionosphere

Figure 3.3 shows the illumination below the ionosphere resulting from a single 100 kA discharge, as a function of frequency and radial distance. The illumination pattern

Table 3.1: Simulation Parameters

Ray Tracing Parameters:	
Plasmasphere model	Simplified GCPM
Magnetic field model	Dipole
Maximum error tolerance	1×10^{-3}
Maximum timestep	5 ms
MLT	0 and 12
K_p	{0, 2, 4, 6, 8}
Latitude spacing	1°
Longitude spacing	1°
Frequency range	200 Hz - 30 kHz
Coarse Frequencies	33 (log-spaced)
Grid and Interpolation Parameters:	
Fine-scale Frequencies	50
Output L-shell range	1.2 - 8
Output L-shell spacing	0.05
Output fieldline latitude spacing	1°

given in equation (2.38) is independent of location along the Earth's surface. We multiply this illumination pattern by the absorption model in section 2.3.1 to determine illumination above the ionosphere. Figure 3.3 shows example illumination patterns for a set of flash latitudes and MLT.

By integrating over latitude, longitude, and frequency, we can estimate the total energy imparted to the magnetosphere by a flash at a given latitude, for daytime and nighttime conditions, as shown in figure 3.4. Our illumination model scales with peak current squared; when combined with the updated ionosphere attenuation curves from 2.6, we see significant overlap between day and night. A strong, midlatitude flash on the day side can easily impart similar energy as a less-intense or lower-latitude flash on the nightside.

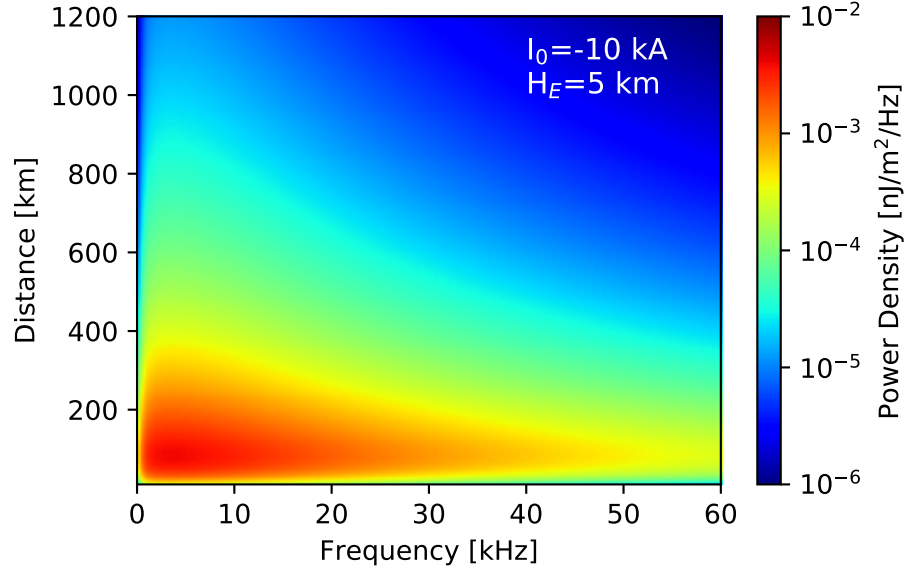


Figure 3.2: Vertically-propagating power density below the ionosphere from a single 100kA cloud-to-ground discharge with $H_E = 5$ km, as a function of frequency and radial distance. Adapted from *Marshall et al.* (2011).

3.2.2 Gridding and Interpolation

We now have a model of the total energy above the ionosphere, at an altitude of 1000 km, divided into gridded bins in latitude, longitude, and frequency. The next step required is to map the energy within each cell out into the plasmasphere. We accomplish this task using a “guide ray” formulation, as illustrated in figure 3.5.

Using the ray tracing and Landau damping technique from section 2.5, we compute rays in 1° steps in both latitude and longitude, within 1000 km of the incident flash, for 33 logarithmically-spaced frequencies between 200 Hz and 30 kHz. Rays are computed for 20 seconds. See table 3.1 for a list of various parameters used. In order to generalize across all longitudes, we use the dipole magnetic field model and the simplified GCPM plasmasphere model. Additionally, we restrict raytracing deviation to the meridional plane to omit any numerical instabilities introduced. The computed rays are then interpolated onto a uniform time axis using one-dimensional linear

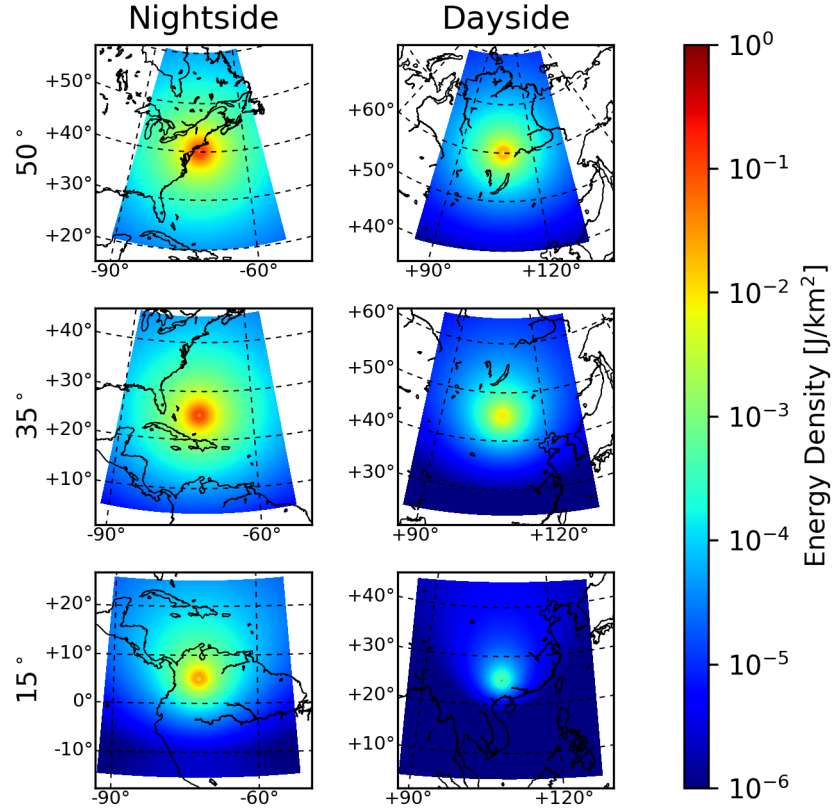


Figure 3.3: Illumination pattern, integrated over frequency, after ionospheric attenuation (altitude = 1000 km). The ionosphere imparts stronger attenuation at equatorial latitudes, and on the dayside. The pre-ionosphere illumination pattern is toroidal, with a central null directly over the incident flash.

interpolation for each parameter.

We make the assumption that the energy bounded by the set of 8 guide rays (two latitudes, two longitudes, two frequencies) remains bounded by these rays as they propagate. Furthermore, we assume that our interpolated timesteps are much larger than the envelope of the wave packet (see figure 2.5). Therefore, the initial energy within each cell is bounded by a four-dimensional voxel, determined by two adjacent timesteps t_{n-1}, t_n of the guide ray set $\{(lat_1, lat_2), (lon_1, lon_2), (f_1, f_2)\}$.

Next, we map the energy within each voxel to our output grid coordinates – chosen

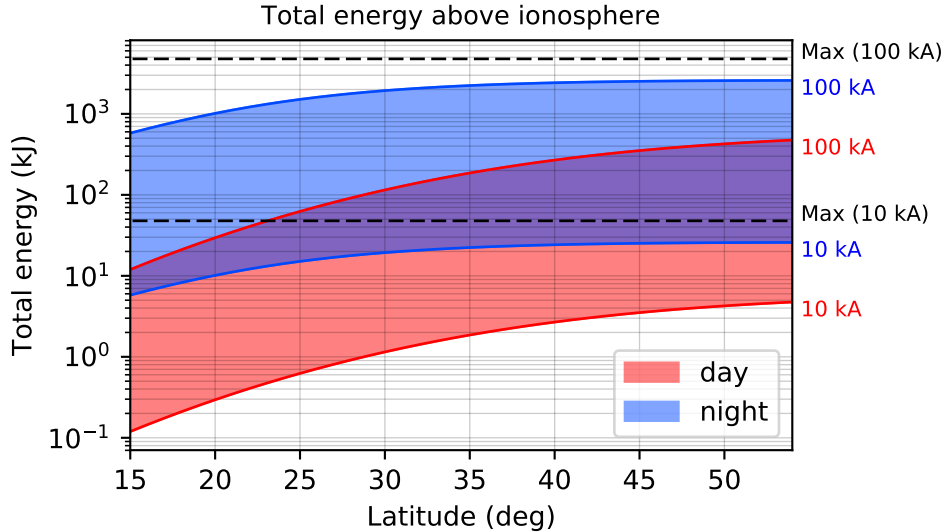


Figure 3.4: Integrated energy above the ionosphere from a single discharge, as a function of geomagnetic latitude. Energy scales quadratically with peak current; totals for 10 kA (an average flash), and 100 kA (a strong, but not unreasonable flash) are overlaid. The dashed lines indicate the total energy released below the ionosphere, before attenuation – ≈ 50 kJ for 10 kA, and ≈ 4 MJ for 100 kA.

here to be 1° steps in latitude, 0.25° in longitude, and 0.05 L-shell. We accomplish this task using an n-dimensional Delaunay triangulation construction (*Delaunay*, 1934; *Lee and Schachter*, 1980). A Delaunay triangulation breaks the convex hull of a volume, as defined by a set of points in \mathbb{R}^n , into a set of primitive shapes called “simplexes”. Each simplex is an n-dimensional triangle.

At each timestep, we compute a Delaunay triangulation for the 16 points defined by corners at $\{(t_{n-1}, t_n), (\text{lat}_1, \text{lat}_2), (\text{lon}_1, \text{lon}_2), (f_1, f_2)\}$. Once a Delaunay triangulation has been made, it is a computationally-efficient task to check whether or not an arbitrary new point is within any of the simplexes. We use the Scipy Delaunay implementation, which is based on the open-source *qhull* code (*Barber et al.*, 1996). For any point within the volume, we assign to it the average energy density in J/m^3 within the voxel at the given timestep, multiplied by the average Landau damping factor. Figure 3.6 illustrates the interpolation method.

Fine-scale frequency interpolation

Our output grid coordinates are given in three dimensions – latitude, longitude, and L-shell. However, our Delaunay construction adds an additional dimension, frequency. We can perform a fine-scale interpolation on the frequency axis by selecting a linearly-spaced grid of sub-frequencies between the two ray frequencies f_1, f_2 . Checking and logging whether or not each new point is within the four-dimensional voxel is equivalent to interpolating and checking in three dimensions, as illustrated in figure 3.7.

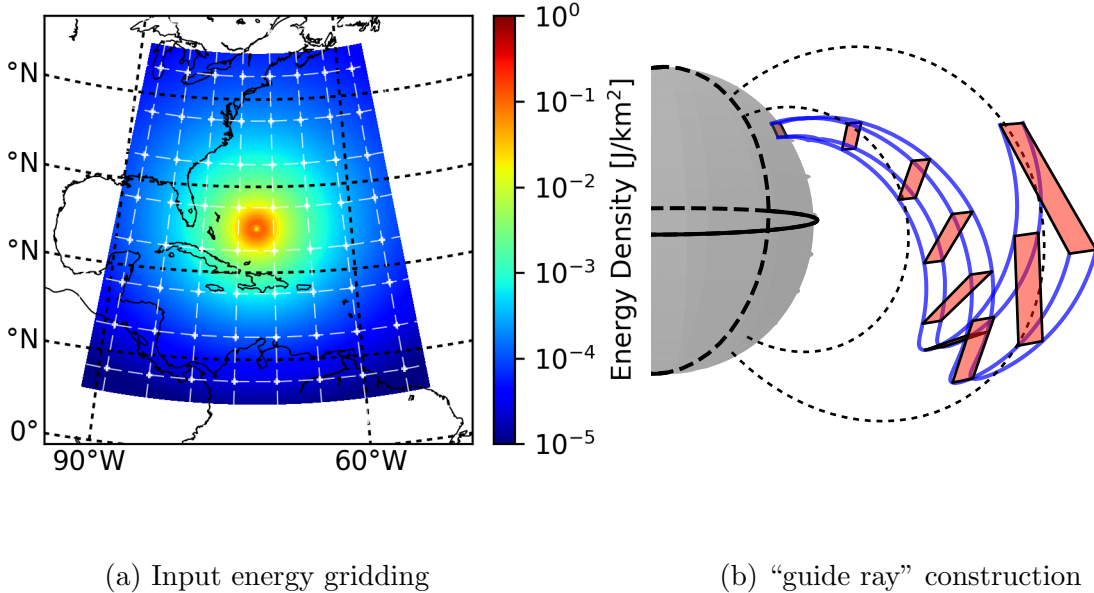


Figure 3.5: An illustration of the interpolation scheme. (a) Energy at the top of the ionosphere is divided into cells, in latitude, longitude, and frequency. Shown here with 5° cells (much larger than used in simulation). The plotted energy is integrated over frequency. (b) Illustration of the guide ray method. Input energy is integrated between a set of guide rays, spaced in latitude, longitude, and frequency. This energy is then averaged over a 4-dimensional volume, bounded by two adjacent timesteps t_{n-1}, t_n of the guide rays.

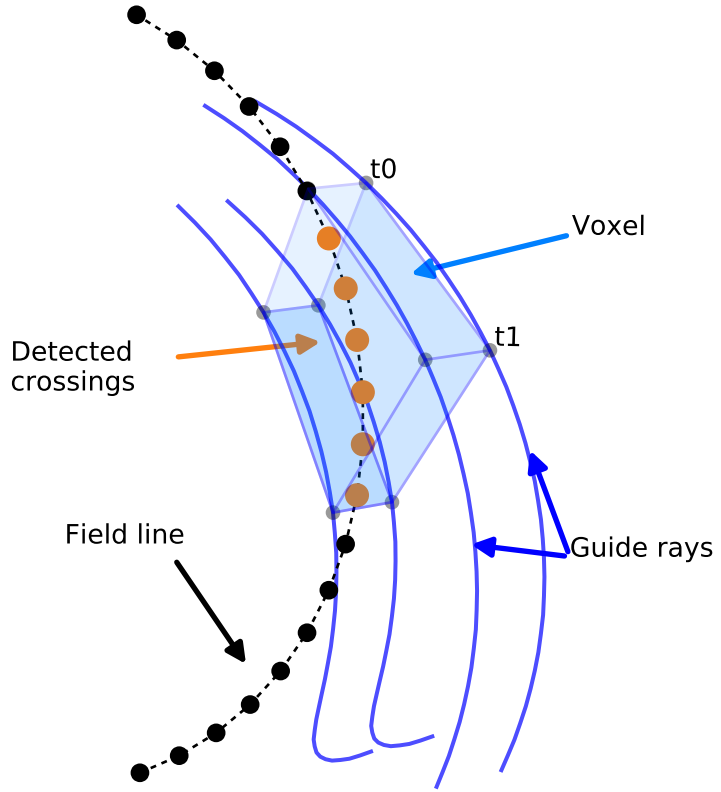


Figure 3.6: Illustration of the Delaunay interpolation method, shown here in three dimensions (e.g., for a single frequency).

Discussion

Our interpolation method differs substantially from *Bortnik* (2005) and related work. *Bortnik* performed an area-weighted interpolation between guide rays in latitude and frequency, and then looked for ray-segment intersections with cross-sectional areas perpendicular to a field line. Crossings, however, are exceedingly rare over the full set of guide rays and output cross-sectional area segments, which requires clever restriction of the output space, or high computational resources. Our method was selected for computational efficiency when relaxing the meridional-plane restriction,

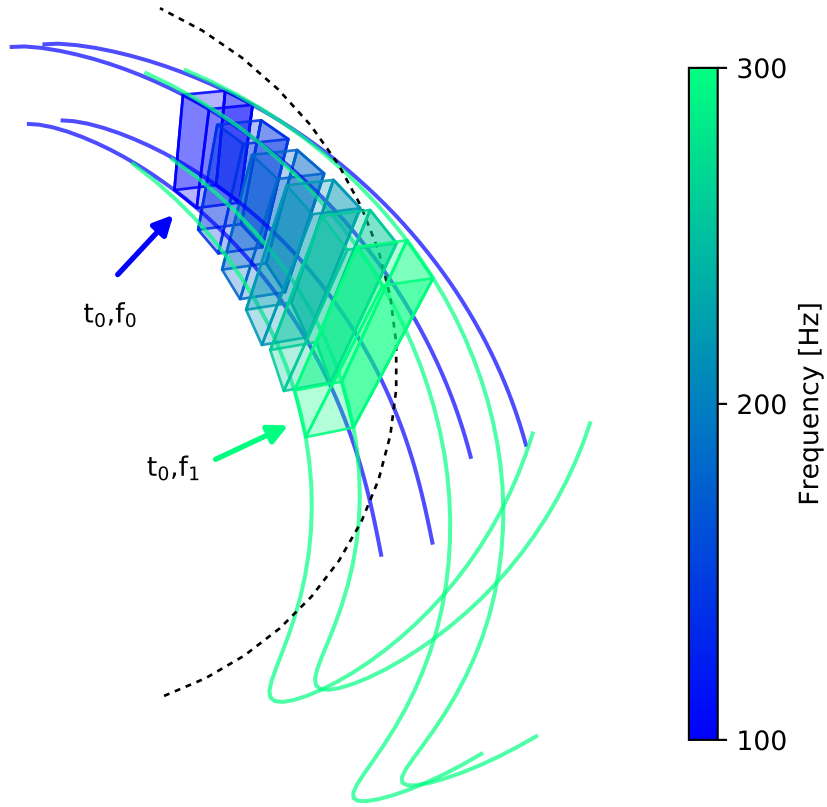


Figure 3.7: An illustration of fine-scale frequency interpolation. Here we show a three-dimensional voxel being linearly interpolated between two sets of guide rays, at $f_1 = 200$ Hz and $f_2 = 300$ Hz. Our implementation operates on a four-dimensional voxel, facilitating rapid checking across fine-scale frequency interpolation steps.

and to assure that all input energy is accounted for. Using the *Bortnik* (2005) method with larger intervals in latitude and longitude can result in undersampling the post-ionosphere illumination pattern, while our method integrates the input energy regardless of grid size.

One caveat of our interpolation algorithm is that the Delaunay triangulation implementation only checks whether or not a point is within the convex hull of the

voxel, rather than the voxel itself. For simple voxels, and at early timesteps (e.g., before any magnetospheric reflection), we can be confident that the voxel remains cubic, and the concave and convex hulls are equivalent. However at later timesteps, after the rays have spread and reflected substantially, the concave and convex hulls are likely not equivalent, in which case the interpolation algorithm may artificially disperse the energy over a larger volume, effectively underestimating energy density while overestimating energy spreading. Figure 3.8 shows some simple polygons and their convex hulls.

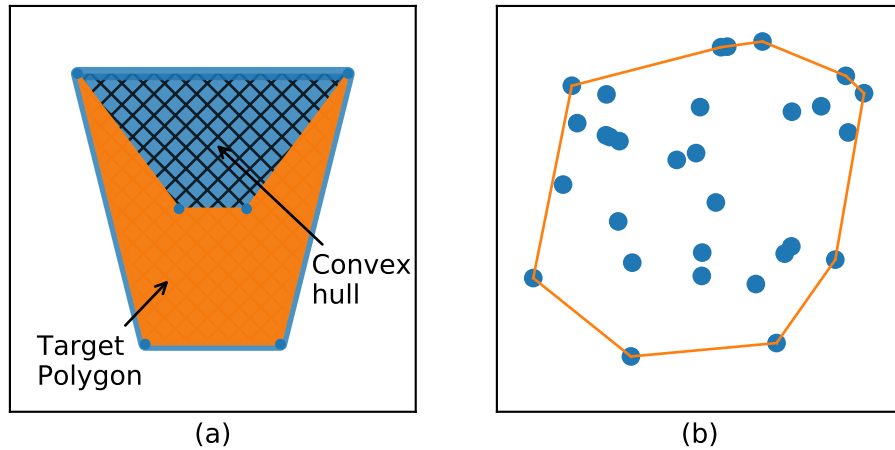


Figure 3.8: Illustration of a convex hull in two dimensions. (a) A simple polygon, shown in orange, for which the convex hull and concave hulls differ substantially. (b) A collection of random points, and their concave hull.

3.2.3 Energy imparted by a single flash

The assembled model of a single flash is parameterized by a flash location (latitude, MLT), and K_p ; the output space can be specified over time, latitude, longitude, L-shell, and frequency. We can reduce the parameter space by integrating over various axes.

Figure 3.9 shows the energy density in the meridional plane, integrated over time and frequency, and averaged over a 0.25° slab in longitude (Note that wave intensity is strongest with a slight offset (~ 100 km) in longitude – see section ??). Energy launched from lower latitudes remains bounded in latitude as it propagates outward; conversely, higher-latitude flashes exhibit more spread in latitude along a fieldline. Higher-latitude flashes also exhibit a stronger “duct-like” enhancement in which energy is well-guided along a fieldline, which we can attribute to the more-gradual curvature of the field line before the first magnetospheric reflection. Lower-latitude flashes encounter stronger field line curvature, and therefore begin to disperse earlier.

Figure 3.10 shows similar data, now volume-averaged over each fieldline, to show the time evolution. In all cases, the most-intense and most-coherent portion of the wave packet disperses within the first ~ 3 seconds. Again, lower-latitude flashes exhibit greater spread in L-shell. Increasing K_p , which brings the plasmapause closer to the Earth, constrains energy within the plasmasphere, both by reflection from the sharp density gradient, and by increased Landau attenuation due to the increased temperature outside the plasmapause from the thermal model in section 2.5.2. However the closer plasmapause has little effect until at least $K_p \sim 4$; for K_p values less than 4, the plasmapause remains well above the normal extent of wave energy.

3.3 Global Energy Density

In order to estimate the global persistent VLF energy density within the magnetosphere, we first precompute the average energy imparted by a flash at an array of latitudes, for the dayside and nightside, which form our stencil array. We note that our illumination model scales with peak current squared ($E \propto I_0^2$), and that the

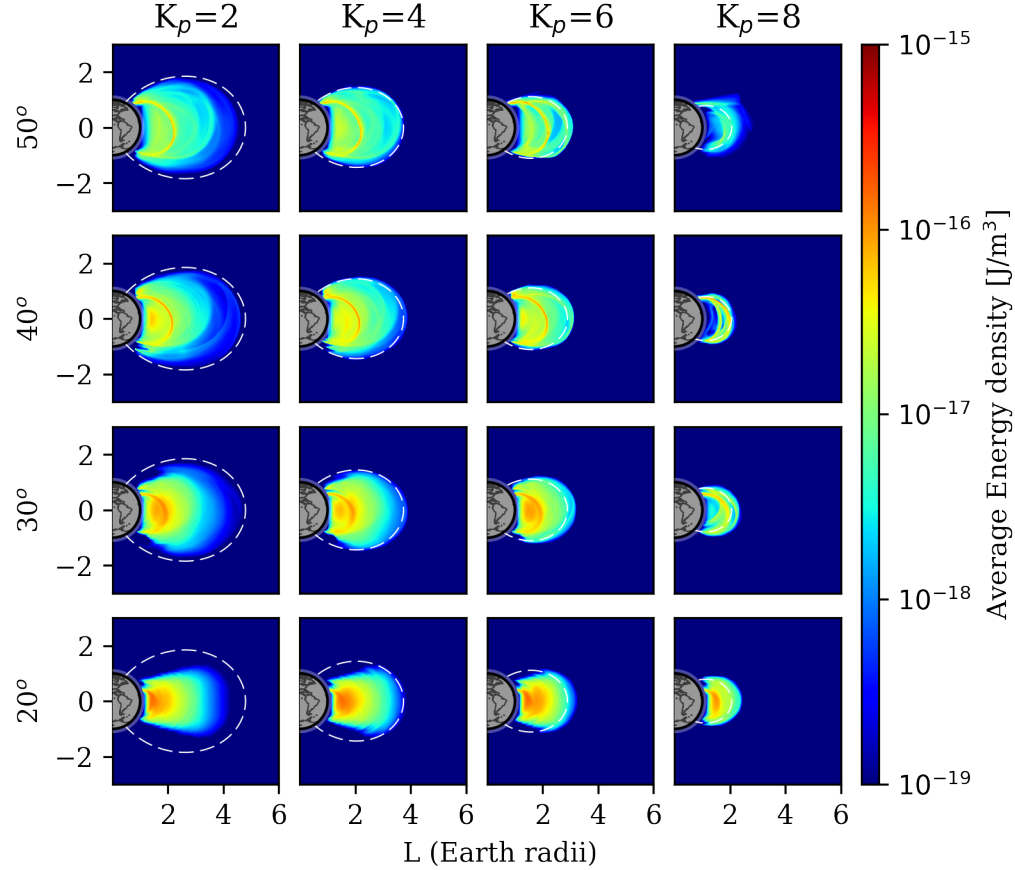


Figure 3.9: Meridional-plane energy densities for a single flash, shown for a variety of input flash latitudes and geomagnetic conditions.

propagation process is assumed to be linear – that is, spatially-coincident flashes have no cumulative effect on each other. We can then simply shift and scale our stencils according to lightning measured from GLD360, and sum / average the result.

Stencils are computed for 1° steps, ranging between 15° and 55° in geomagnetic latitude. Noting that the plasmasphere density model is symmetric north / south, and that the magnetic field model is symmetric with the exception of polarity, we assume the impact of a southern hemisphere flash is identical to that of a field-line-coincident northern hemisphere flash. Longitude variation is computed in 0.25° steps,

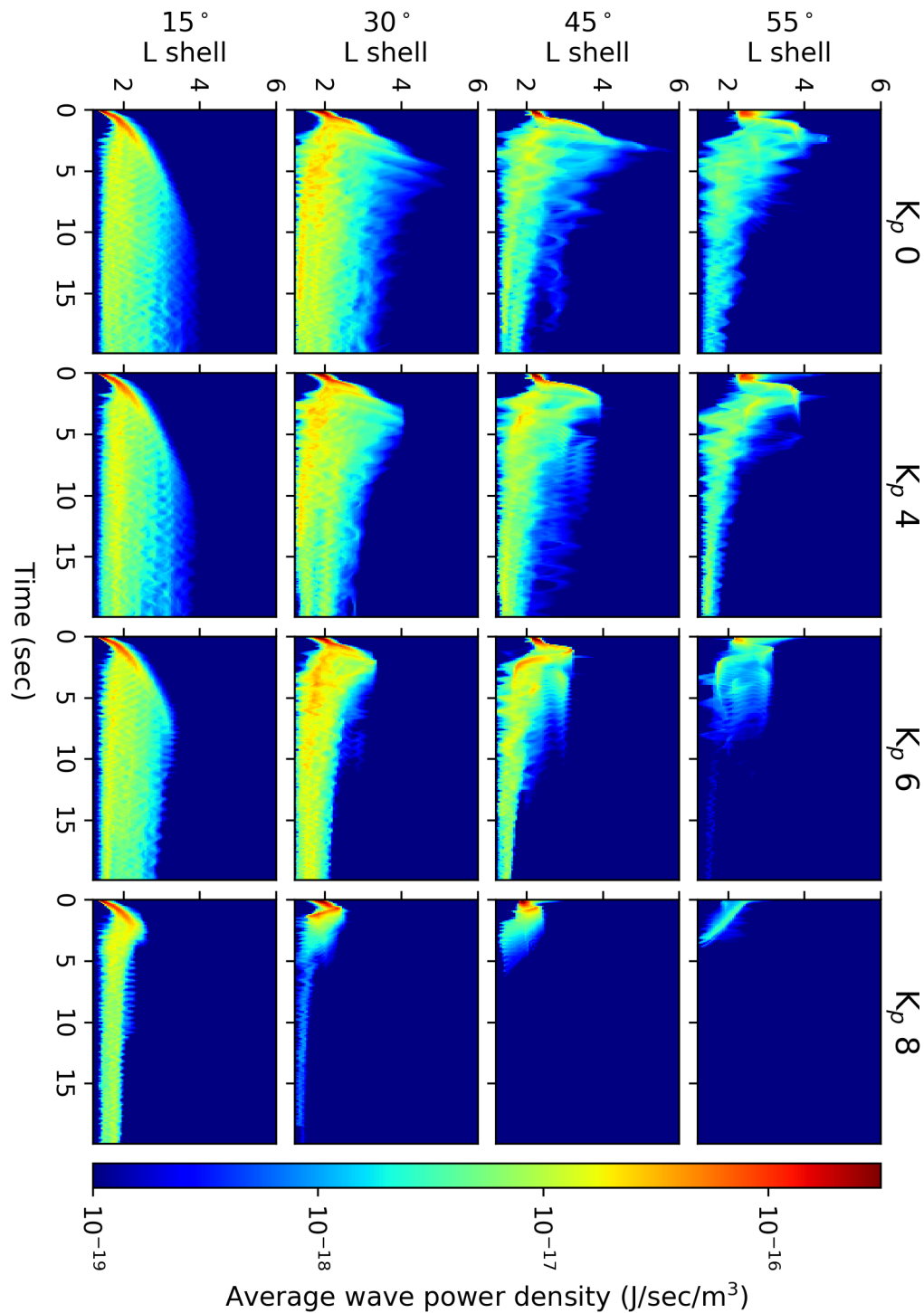


Figure 3.10: Energy density time series plots, for a range of flash latitudes and geomagnetic conditions. Energy is averaged over a 0.25° section in longitude, centered over the flash.

with a maximum extent of 20° from the flash location. We compute stencils for two MLT values, 0 and 12, representing the nightside and dayside, and select a stencil set accordingly for each flash. Finally, we compute stencils for an array of K_p values – $\{0, 2, 4, 6, 8\}$ – and linearly interpolate along this axis for measured values of K_p .

Figure 3.11 shows a grid of nightside energy stencils for several latitudes and several K_p .

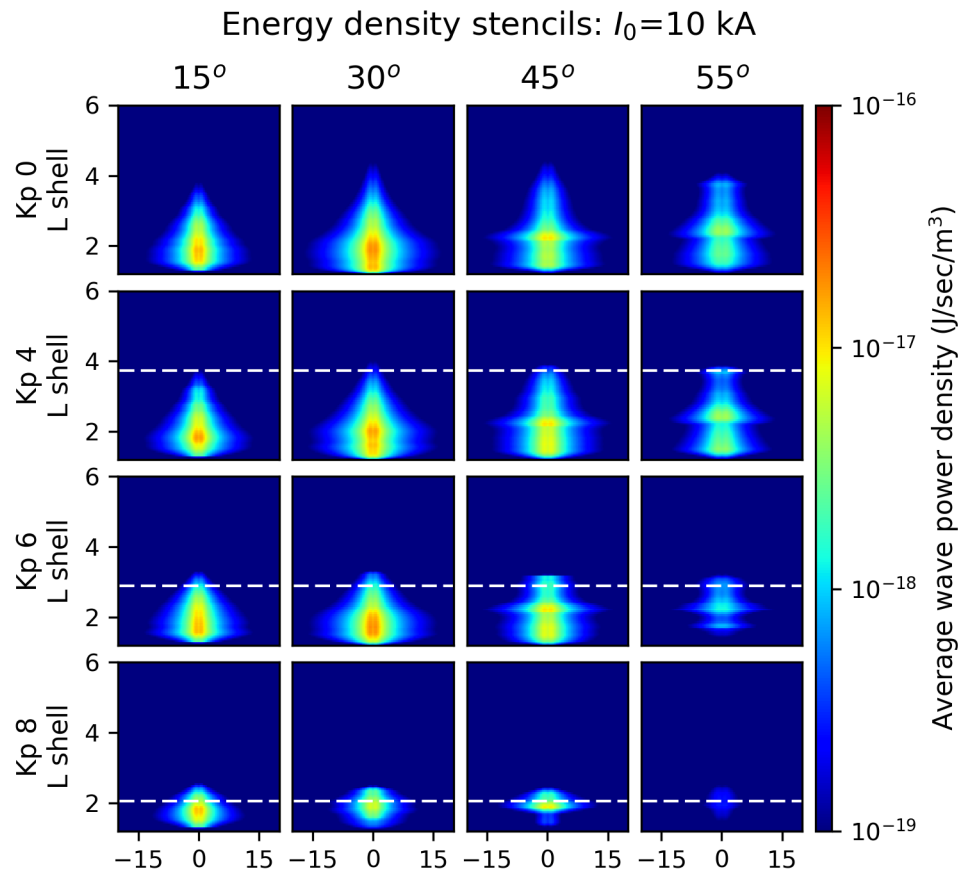


Figure 3.11: Energy density stencils for a range of flash latitudes and geomagnetic conditions, for a nightside, 10 kA flash. The dashed white lines indicate the location of the plasmapause, which is brought closer to the Earth with increasing K_p .

3.3.1 Results of the global model

We apply the shifted and scaled stencil technique to the GLD360 dataset, for all detected flashes between August 2014 and April 2016. Flashes are then binned into dayside and nightside by quantizing magnetic local time:

$$MLT = UT + (\phi_{flash} - \phi_{ut})/15 \quad (3.1)$$

$$\text{Day} \equiv 6 < MLT \leq 18 \quad (3.2)$$

$$\text{Night} \equiv (MLT \leq 6) \parallel (MLT > 18) \quad (3.3)$$

where ϕ_{flash} is the magnetic longitude of the incident flash, UT is the fractional hour of day in universal time, and ϕ_{ut} is the UT reference magnetic longitude of Greenwich (*Laundal and Richmond, 2016*).

We use historical K_p values corresponding to each flash. However we replace K_p with $K_{p(max)}$, as in *Carpenter and Anderson (1992)*, in order to better align with the plasmasphere model used. $K_{p(max)}$ is defined as the maximum value of K_p within the preceding 24-hour period.

Figure 3.12 shows the resulting energy density, averaged over the entire date range, broken out into day and night. Figures 3.13 and 3.14 show the results averaged across the all longitudes.

As shown in figure 3.13, energy density falls off logarithmically with respect to L. The cumulative effect of the plasmapause, the variance of which is taken into effect via multiple K_p values, results in an additional dropoff at $L \sim 4.8$. Energy along the nightside is an order of magnitude greater than the dayside; however outside the plasmapause, day and night are essentially equivalent.

When broken out over K_p as in figure 3.14, it is apparent that the moving plasmapause location effectively constrains energy to within the inner plasmasphere; however it has little effect on the average energy at lower L-shells, within the inner radiation belt and slot region.

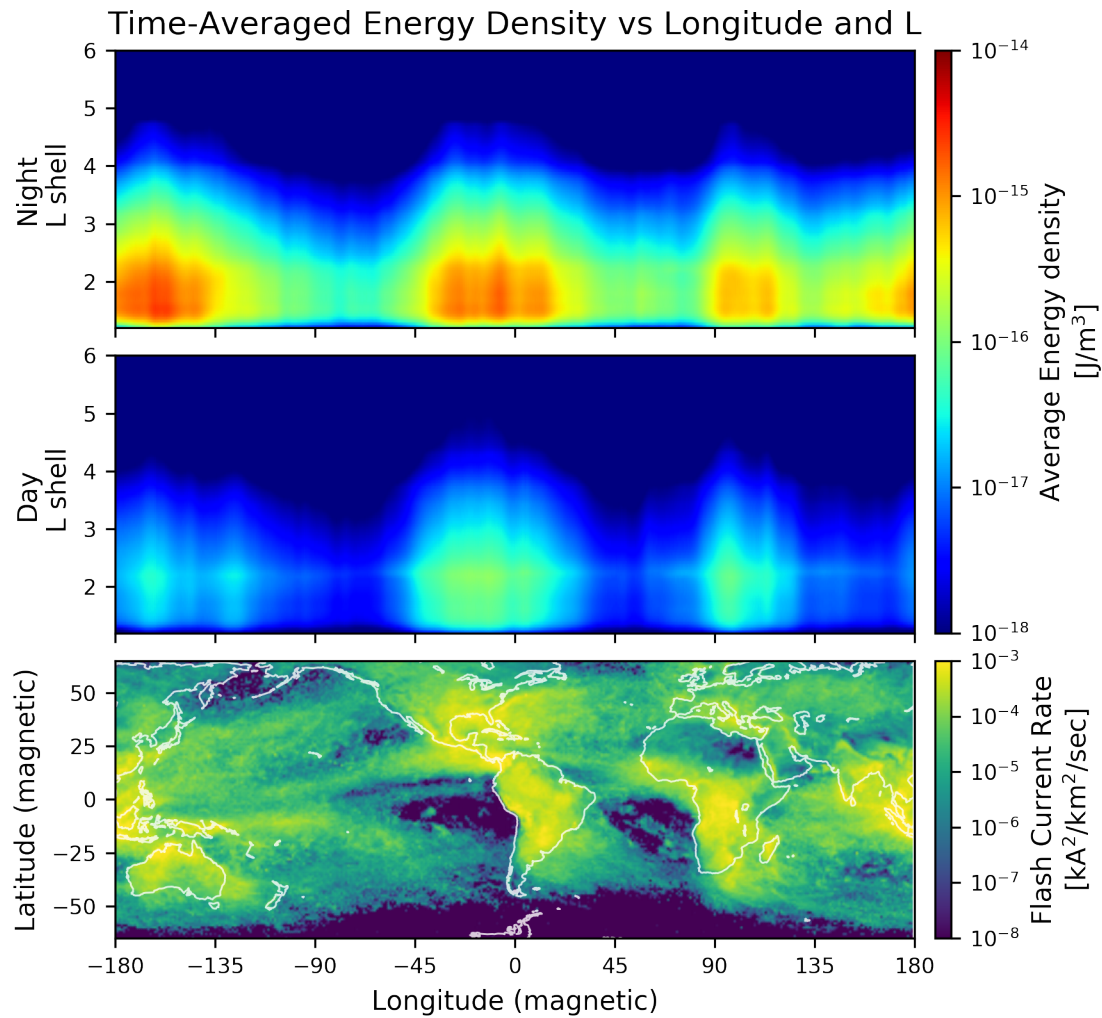


Figure 3.12: Average energy density as a function of L-shell and geomagnetic longitude. The top plot shows the nightside only, and the middle plot shows dayside only. The bottom plot shows the corresponding peak current distribution input into the model.

Frequency dependence We can examine the frequency spectrum resulting from lightning as a function of L-shell, as shown in figure 3.15. Generally, as seen in figure 2.13, lower-frequency rays propagate further out into the magnetosphere, while

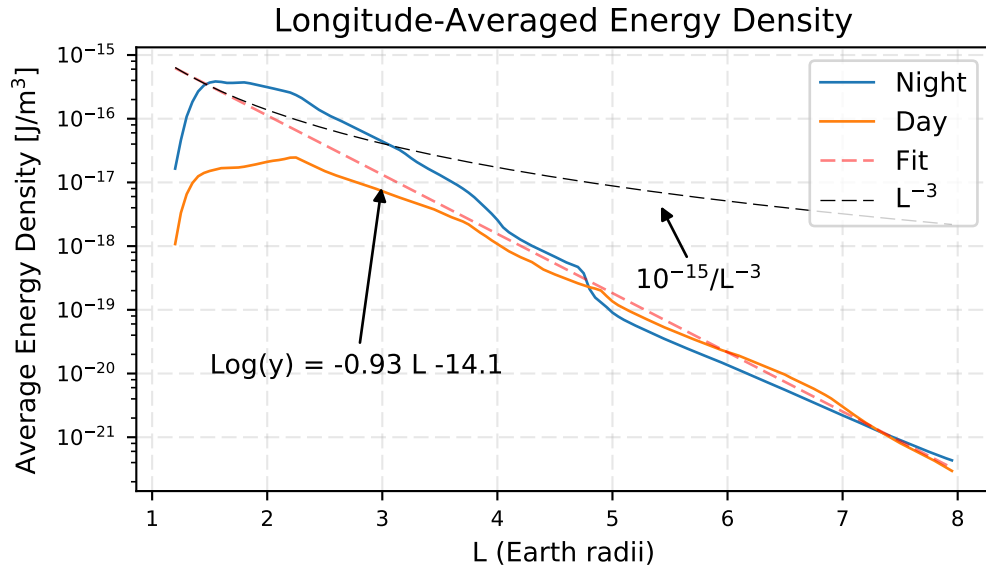


Figure 3.13: Global, longitude-averaged energy density for day and night. The energy density is logarithmic with increasing L . The dashed black line shows an approximate $1/R^3$ trend, in comparison with an isotropic radiator.

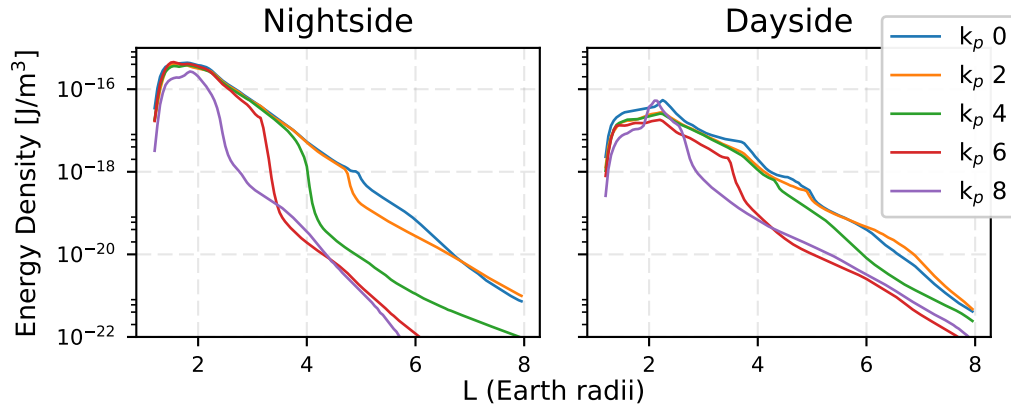


Figure 3.14: Average energy density for day and night, as in figure 3.13, broken out over multiple values of K_p . At higher K_p , the plasmapause effectively confines wave energy to the inner plasmasphere.

higher-frequency rays are strongly-deflected and impact the Earth before a single magnetospheric reflection. This trend results in rays “settling” onto specific fieldlines, dependent on frequency.

The relationship between peak frequency and L-shell is well-defined by a logarithmic fit:

$$\log_{10}(f_{peak}) = 4.56 - 0.48L \quad (3.4)$$

An additional feature of note in figure 3.15 is the broad range of frequencies present at $L \sim 2.3$, the location of which strongly supports the hypothesis of lightning as a key mechanism for slot region depletion.

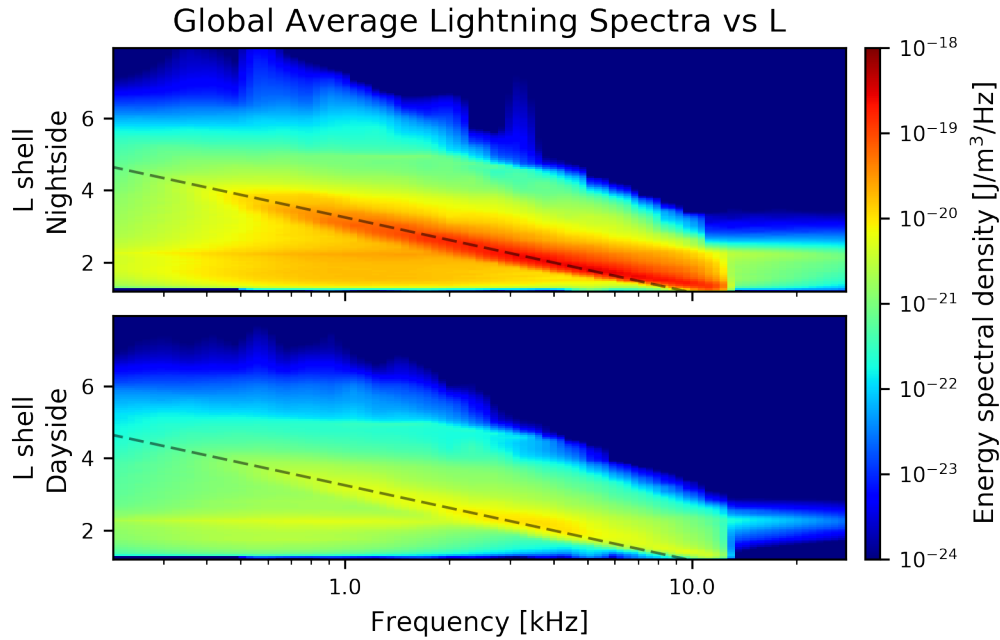


Figure 3.15: Average energy density as a function of L-shell and wave frequency. Dashed lines show a log-linear fit to the peak frequency as a function of L-shell in equation (3.4).

3.4 Longitude Dependence

As mentioned previously, our ray tracing is confined to the meridional plane axis, with no deviation along the longitudinal axis. In order to greatly reduce computation time and storage requirements, it is desirable to find a scaling function with respect to longitude, so that we need only compute power densities along a single meridional plane slice (e.g., a fixed longitude, offset from the initial flash), and simply weight it accordingly to compute a full 3D solution. *Lauben* chose a longitude scaling function according to the assumed peak resonance frequency; similarly, *Bortnik*, noting that the model is entirely linear, chose a longitude scaling function to be the ratio of input powers from equation (2.38)

$$F(\phi) = \frac{S(\phi)}{S(\phi_0)} \quad (3.5)$$

$$= \frac{\sin^2 \theta / r^2}{\sin^2 \theta_0 / r_0^2} \quad (3.6)$$

where ϕ and ϕ_0 are the offset and reference longitudes, θ and θ_0 are the zenith angles, and r and r_0 are the radial distance from the input flash. Note that the frequency dependence terms cancel out nicely, as there is no change in the frequency terms with respect to longitude. In order to avoid the central null directly above the incident flash, *Bortnik* uses a longitude offset of $\sim 1^\circ$ for the reference slice.

The power-ratio scaling factor is completely accurate, so long as we consider only rays launched from the same latitude as the incident flash. However, scaling our model *output* according to model *input* is somewhat of a compromise, as the total meridional-plane power is the result of a scaled family of rays, launched from a range of latitudes. Each latitude has a slightly different longitude offset, and will in actuality be further from the flash than the power scaling in equation (3.6) predicts; the net result will be a slight overestimation of power along the scaled longitudinal axis. Furthermore, the effect is more-prominent closer to the incident flash, where input energies are strongest. Figure 3.16 illustrates the scaling geometry.

Using the full 3D solution, we can examine whether or not a single scaling function

will work for all latitudes within a given stencil. Figure 3.17 shows the normalized scaling factor as a function of longitude offset from the incident flash, for each latitude in the stencil, for 5° increments in flash latitude. Lower-latitude flashes exhibit a wider spread in scaling; the spread reduces as the flash latitude increases, reaching a minimum at $\sim 35^\circ$, and broadening out again at higher latitudes.

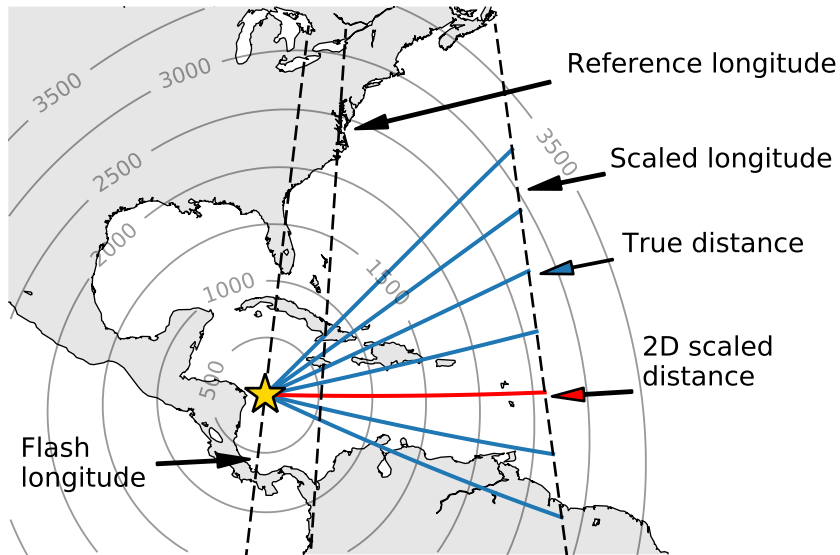


Figure 3.16: Illustration of the geometries involved in scaling along the longitudinal axis. The dashed black lines show the meridional plane slices above the flash, at the reference longitude, and at the target longitude to be scaled. Blue lines indicate the true distance from the flash, and the red line indicates the distance used in the 2D scaling. Contour lines denote radial distance from the flash, in kilometers.

Our 3D implementation computes the meridional-plane power density along each offset longitude, using true scaling for each set of guide rays. Figure 3.18 compares our full 3D weighting with the *Bortnik (2005)* scaling method. For longitudes less than the reference longitude, we use the reference longitude result, in order to compensate for the central null. Signed, relative errors are shown with respect to the mean of both models:

$$\epsilon = \frac{P_{2D} - P_{3D}}{(P_{2D} + P_{3D})/2} \quad (3.7)$$

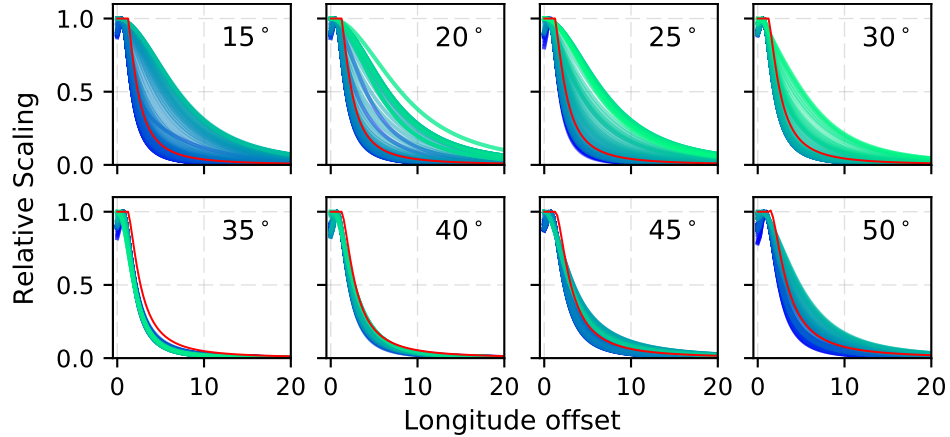


Figure 3.17: Plots of the relative longitude scaling factors for a set of flashes, between 15° and 50° , in 5-degree increments. Each line is normalized by its value at the reference longitude, for a given latitude offset from the flash. The spread in scaling factors is broad at lower-latitude flashes, becoming more-consistent at mid-latitudes, and broadening out again at high latitudes. Red lines indicate the 2D scaling function in equation (3.6)).

Figure 3.19 shows the average error across the entire stencil versus K_p and longitude. On average, the 2D scaling factor overestimates power density by $\sim 15\%$.

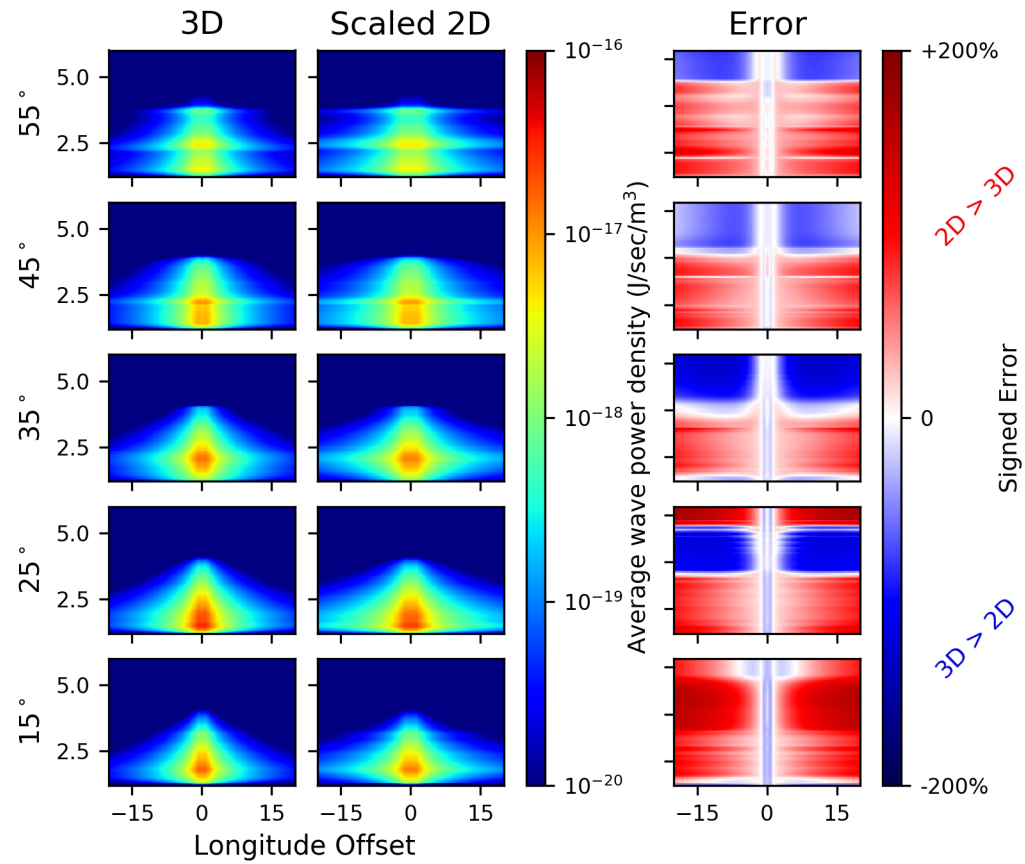


Figure 3.18: A comparison of meridional-plane power density stencils, using the full 3D solution and the scaled 2D solution, for $K_p = 4$. The rightmost column shows the signed relative error on a per-pixel basis.

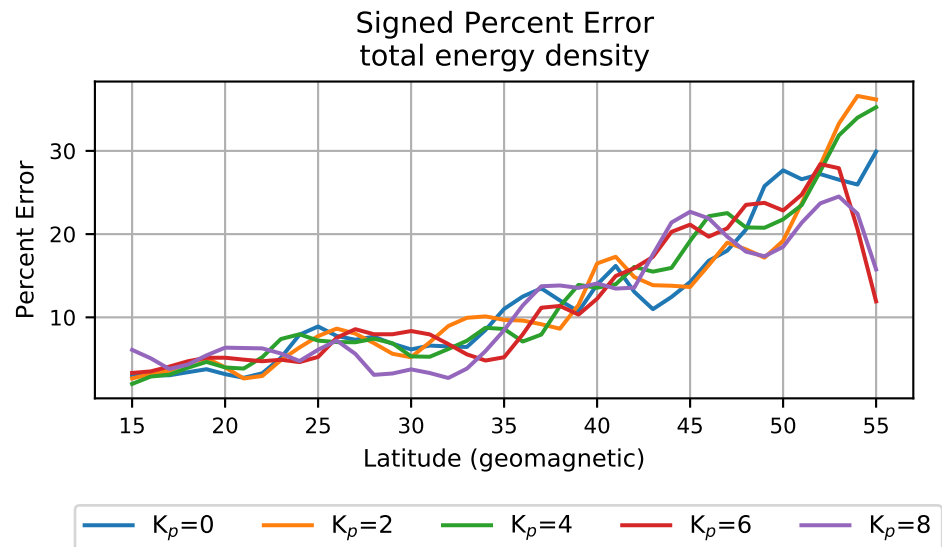


Figure 3.19: Total signed percentage error between stencils generated with the 2D scaling technique and the full 3D scaling method. On average, the longitude scaling function in equation (3.6) overestimates energy density by $\sim 15\%$.

Chapter 4

Global and Seasonal Estimates of LEP

The purpose of this chapter is to provide quantitative upper and lower-bound estimates on the expected electron flux due to LEP, as a function of location and time of year. We expand on the raytracing and interpolation method described in chapter 3, by incorporating a resonant-particle scattering code. We compute global electron fluxes in a similar manner as in chapter 3, using an array of precomputed stencils, which we scale and shift according to GLD360 data. Finally, we can examine the relative timescales on which LEP could deplete a populated magnetic field line, in the absence of any other loss processes.

4.1 Resonant Interactions

As discussed in section 2.7, the interaction between waves and trapped particles has a cumulative effect only when certain resonant conditions are met. The condition for resonance is given by:

$$\frac{d\eta}{dt} = m\omega_c/\gamma - \omega - k_z v_z = 0 \quad (4.1)$$

where m is the resonance order number, $\gamma = (1 - v^2/c^2)^{-1/2}$ is the Lorentz relativistic correction factor, ω_c is the local Cyclotron frequency, and k_z and v_z are the parallel

components of the wavenormal vector and particle velocity with respect to the background magnetic field. η represents the angle between the wave magnetic field vector and v_{\perp} .

We assume any perturbation in pitch angle is small, and can therefore only concern ourselves with particles very near the edge of the loss cone. We can therefore relate the total velocity v and the parallel velocity v_z via $v^2 = v_z^2 / \cos^2 \alpha_{lc}$ (*Lauben et al.*, 2001; *Bortnik et al.*, 2006).

Plugging in the above terms for γ and v_z gives us the following closed expression for the resonant particle velocity for an incident wave:

$$v_z^{res} = \frac{\pm \sqrt{\omega^2 k_z^2 + [(m\omega_c)^2 - \omega^2][k_z^2 + (\frac{m\omega_c}{c \cos \alpha_{lc}})^2]} - \omega k_z}{k_z^2 + (\frac{m\omega_c}{c \cos \alpha_{lc}})^2} \quad (4.2)$$

$$v_{res} = \|v_z^{res}\| \cos \alpha_{lc} \quad (4.3)$$

$$E = \frac{E_{rest}}{\sqrt{1 - v_{res}^2/c^2}} - 1 \quad (4.4)$$

where E_{rest} is the particle rest energy ($\approx 5.1 \times 10^5$ eV for an electron).

Equation (4.2) is a function of the incident wave, which is dependent on the wavenormal angle and the background plasma through k_z . We can illustrate broad trends by plotting resonant frequency vs E along the geomagnetic equator, for normal incidence ($k = k_z$). Figure 4.1 shows the resonant frequency for a range of L-shells, for $m = \{0, 1, 2\}$. Somewhat counterintuitively, lower-energy particles resonate with higher-frequency waves.

L-shell dependence is due both to the background electron density through k_z , and the background magnetic field through ω_c . particles along higher L-shells resonate with lower-frequency waves.

At lower energies, the resonant modes are integer multiples of each other; however as the particles become increasingly relativistic, the modes deviate substantially. Most significantly, when setting $m = 0$, the relativistic term vanishes completely, and the

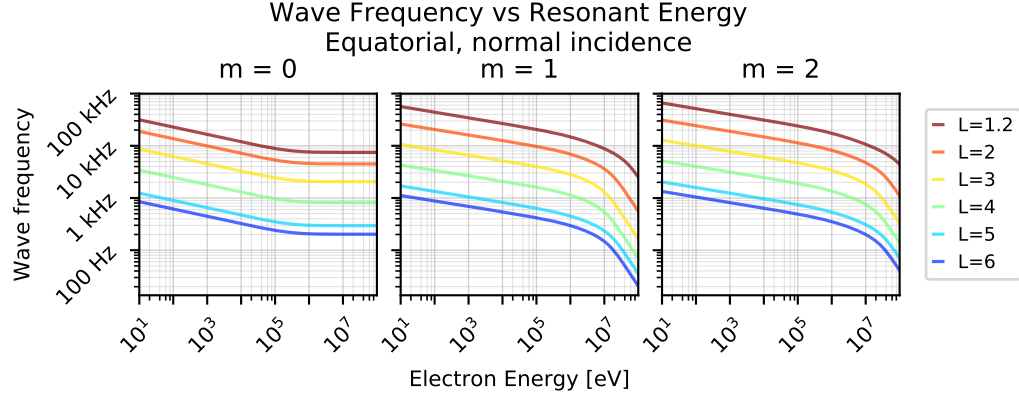


Figure 4.1: Resonant wave frequency vs trapped electron kinetic energy, for resonant modes $m = 0$, 1, and 2. Shown here for resonances along the geomagnetic equator, with normal incidence. The background plasma is modeled for $K_p = 0$ using the Simplified GCPM model in section 2.5.

resonant frequency asymptotes.

4.1.1 Calculating pitch-angle scattering vs time

Calculating pitch-angle perturbation incurs additional complexity as compared to the energy density estimate in section 3. Pitch-angle scattering is dependent on wave amplitude and frequency, as well as incident wavenormal angle θ and gyrophase η . Additionally, the formulation for pitch-angle scattering requires wave amplitudes with units $\sim 1/m^2/s$ cross-sectional area rather than volumetric densities, $\sim 1/m^3$.

The fundamental pitch-angle scattering equation is given in (2.57), and reproduced below:

$$\frac{d\alpha}{dt} = \underbrace{\frac{m_e \omega_{rm}^2}{k_z p_\perp} \left(1 + \frac{\cos^2 \alpha}{m \omega_c / \omega - 1} \right)}_{T_1} \underbrace{\sin \eta}_{T_2} + \underbrace{\frac{1}{m_e \gamma} \frac{p_\perp}{2 \omega_c} \frac{\partial \omega_c}{\partial z}}_{T_3} \quad (4.5)$$

Terms T_1 and T_3 are slowly-varying, and can be treated as pseudo-constant at a fixed position in space. Term T_2 in (4.5) is the resonant component. Outside of resonance this term varies from ± 1 . At resonance, however, this term remains constant, allowing coherent changes to accumulate over the interaction period. Resonance implies only that $d\eta/dt = 0$, and provides no information on the value of η . We

assume η is uniformly distributed, in which case the perturbation in pitch angle will be sinusoidally distributed, symmetrically about 0 (*Inan*, 1977). Since we are concerned only with the distribution of particles which are perturbed into the loss cone ($d\alpha/dt < 0$), we can then track the RMS-average pitch angle change $\Delta\alpha_{RMS}$, and calculate the precipitated fraction using the uniform distribution (see section 4.2). Figure 4.2 shows an example of a test-particle simulation, in which a set of particles with different initial η values are subjected to the same perturbing wave.

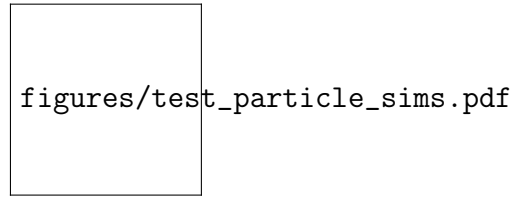


Figure 4.2: test particle sim

From here, we follow the numerical solution method from *Bortnik* (2005); *Bortnik et al.* (2006).

A key assumption in our scattering calculation is that the interactions on a single particle from each discrete frequency are independent from one another. Furthermore, we discretize each fieldline into 1° segments, and assume the scattering within each segment is independent from each other. While neither of these assumptions are exactly true, together they provide a critical and substantial reduction in complexity: we no longer have to track the action of the entire set of waves on a discrete set of particles (as in a test particle simulation such as *Chang and Inan* (1985)), but rather can track the stochastic pitch-angle change on a distribution of particles. Additionally, by assuming incoherent scattering across frequencies, the problem becomes much more well-suited to a parallel processing solution, as we can spread computation for each frequency across an array of nodes.

Thus, for each set of guide rays F , using the interpolation scheme from section 3, we can calculate $\Delta\alpha_{RMS}$ as a function of magnetic fieldline, particle energy, and time; the effective change in pitch angle is then determined by summing over the set

in quadrature:

$$\Delta\alpha(E, \mathbf{x}, t) = \frac{1}{2} \sqrt{\sum_F \Delta\alpha_{RMS}^2(E, \mathbf{x}, t, F)}. \quad (4.6)$$

The decision to calculate RMS pitch-angle scattering vs a full test-particle approach is the fundamental difference between *Lauben* (1998) and *Bortnik* (2005), the two most-closely related works to ours. *Bortnik et al.* uses the above method, while *Lauben* infers expected distributions from a set of test particles.

As noted by *Lauben* (1998); *Lauben et al.* (2001), a subset of particles, when subjected to ideal conditions, can “ride” a perturbing wavefront across several degrees in latitude, and experience sustained, coherent perturbation. These particles would then precipitate very deeply into the ionosphere, which may account for the lowest-altitude ionization as measured using VLF sub-ionosphere sensing. However these particles represent only a small fraction of the precipitating electrons, the bulk of which experience a random walk through the set of perturbing waves, and are well-modeled by the stochastic RMS formulation of *Bortnik*.

Bortnik makes several approximations which allow for quick numerical integration of (4.5), the details of which are beyond the scope of this dissertation. For a concise description of the methodology, see *Bortnik et al.* (2006).

Table 1 shows the algorithm in pseudocode. Using the assumptions of incoherence described above, we can independently calculate squared pitch-angle change for every enumerated combination of: a) guide ray sets F , b) latitudes along an output fieldline λ , c) time steps t , d) resonant modes m , and e) resonant particle energies E .

To account for variation in precipitation time, we record the perturbation in pitch angle at the time in which a perturbed particle would precipitate into the ionosphere. This time is dependent on both particle energy and the latitude along the field line where the perturbation occurred, and may be asymmetric between the northern and southern hemispheres.

We compute the time of flight from the interaction latitude λ to the ionosphere by assuming a perturbed particle continues along a fixed fieldline, by numerically evaluating the expression from *Walt* (1994), equation 4.25:

Algorithm 1 RMS change in pitch angle

```

1: for all output field lines do
2:    $d\alpha_N \leftarrow \text{Zeros}(E, t)$             $\triangleright$  Pitch angle change at northern hemisphere
3:    $d\alpha_S \leftarrow \text{Zeros}(E, t)$             $\triangleright$  Pitch angle change at southern hemisphere
4:   for all sets of guide rays do
5:     Scale input energy according to input flash location and frequency
6:     for all latitudes along field line  $\lambda$  do
7:       for all time steps  $t$  do
8:         for all resonant modes  $m$  do
9:           Calculate  $V_{res}$ ,  $E_{res}$ 
10:          for all grid energies within resonance band  $E$  do
11:             $\Delta\alpha_{cur} \leftarrow \int_{t1}^{t2} \frac{d\alpha}{dt}$ 
12:             $tN \leftarrow t + \tau_{f,N}$             $\triangleright$  flight time to northern ionosphere
13:             $tS \leftarrow t + \tau_{f,S}$             $\triangleright$  flight time to southern ionosphere
14:             $d\alpha_N[E, tN] += (\Delta\alpha_{cur})^2$ 
15:             $d\alpha_S[E, tS] += (\Delta\alpha_{cur})^2$ 
16:           $d\alpha_N \leftarrow \sqrt{d\alpha_N}$ 
17:           $d\alpha_S \leftarrow \sqrt{d\alpha_S}$ 

```

$$\tau_f = \frac{1}{v} \int_{s_1}^{s_2} \left(1 - \frac{B(s)}{B_{eq}} \sin^2 \alpha_{eq} \right)^{-1/2} ds \quad (4.7)$$

4.1.2 Example energy-time spectra

Figure 4.3 shows a typical pitch-angle scattering matrix, as a function of electron energy and time delay from a lightning flash at 35° latitude, with $I_0 = -10\text{kA}$. A similar scattering matrix must be computed for every point in the output space (L-shell and longitude offset).

Several key features are apparent: First, the descending curve shape is due to the time delay from the interaction region to the precipitation altitude, with slower moving electrons taking longer to reach the ionosphere. Two banded structures are visible with respect to energy: the dominant band, below $E \sim 10$ keV, is due to the 0-order resonance mode. The upper band with energies above $E \sim 100$ keV, is due largely to the ± 1 resonance modes. Scattering efficiency decreases with increasing resonance order. While some asymmetry exists between the northern and southern

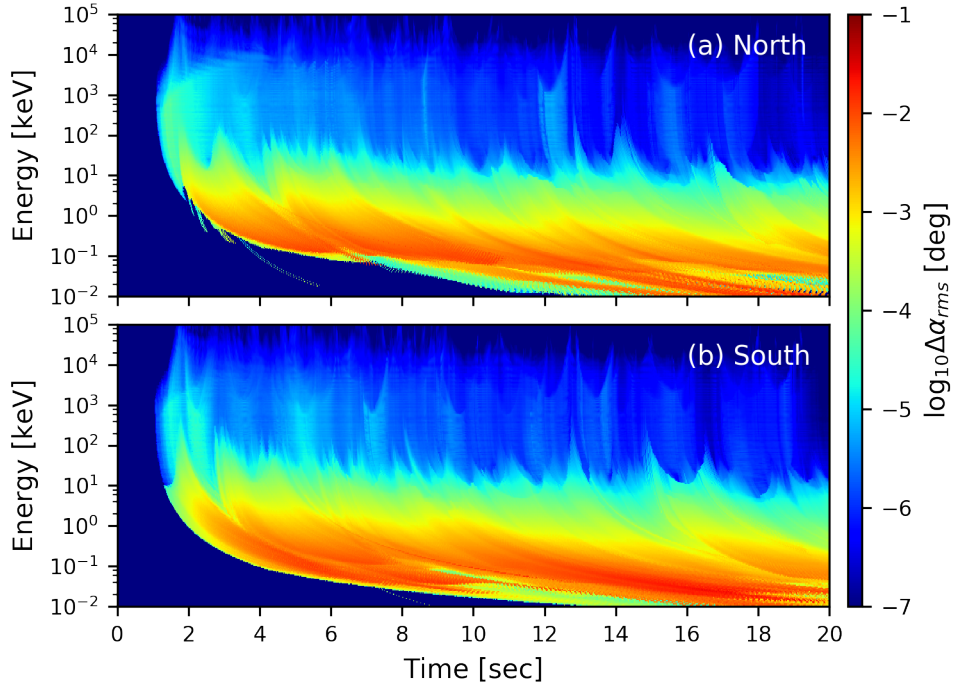


Figure 4.3: Pitch angle scattering matrix along a fieldline with $L=3$, for a 10 kA flash at 35° latitude, through a nightside ionosphere at $K_p = 0$. Scattering is centered directly over the input flash longitude, within a width of $\pm 0.25^\circ$.

hemispheres, the magnitude remains similar due to the numerous bounces of the incident waves, and that the higher-order modes resonate with particles traveling in either direction.

Perturbations in pitch angle due to LEP are generally small; well below 0.1° . However, due to the exponentially-increasing density of the ionosphere below our threshold height of 100 km, and thus the very small change in reflection altitude required, small changes in pitch angle can greatly increase an electron's likelihood of precipitating. Figure 4.4(a) shows the perturbed reflection altitudes versus L -shell, for an array of $\Delta\alpha$ values. Figure 4.4(b) shows the minimum perturbation value required in order for a particle to reflect at a given altitude.

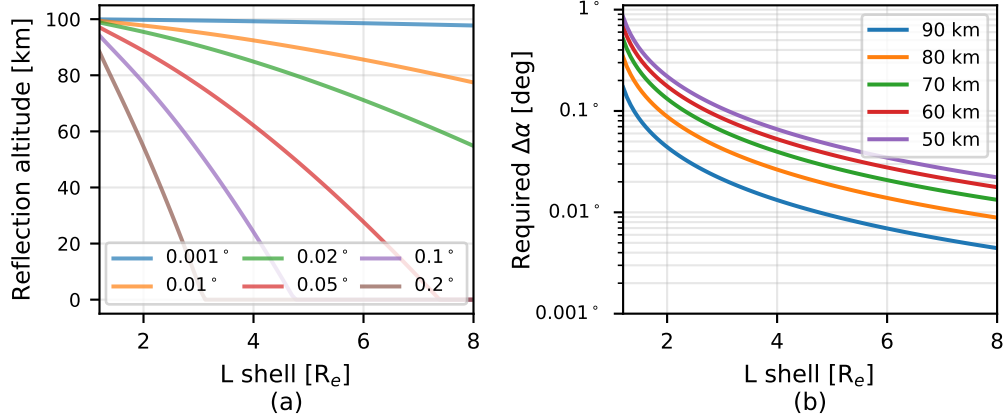


Figure 4.4: (a) Reflection altitude vs L-shell for a particle, for an array of equatorial pitch-angle perturbations. (b) The minimum perturbation required to drive a particle with pitch angle $\alpha = \alpha_{lc}$ to a fixed reflection altitude, as a function of L-shell, for an array of target altitudes.

4.2 Calculating flux from pitch-angle perturbations

We have now computed the RMS change in pitch angle along a single field line, as a function of electron energy and time, for a single lightning flash. Next we must convert our scattering matrices (figure 4.3) into electron fluxes (or energy fluxes). Again, we follow the method used by *Bortnik* (2005) (section 5.1.3).

Along each target fieldline, we use our calculated pitch angle changes $\Delta\alpha(E, t)$ to perturb a collection of electrons with an assumed distribution in pitch angle. Perturbation is accomplished by convolving an assumed distribution of particles $G(E, t, \alpha)$ with the perturbing function $\Delta\alpha(E, t)$ for each energy and time bin. The resulting particle flux is the number of electrons within the loss cone ($\alpha < \alpha_{lc}$) after perturbation. We assume that scattering is independent with respect to both the time and energy axes, and can thus be evaluated independently for each E-t bin. Solving the convolution analytically greatly improves computational efficiency.

We use the solution from *Bortnik* (2005) for a “ramp” distribution in pitch angle, which can be applied to any general pitch angle distribution by computing a series approximation about $\alpha = \alpha_{lc}$.

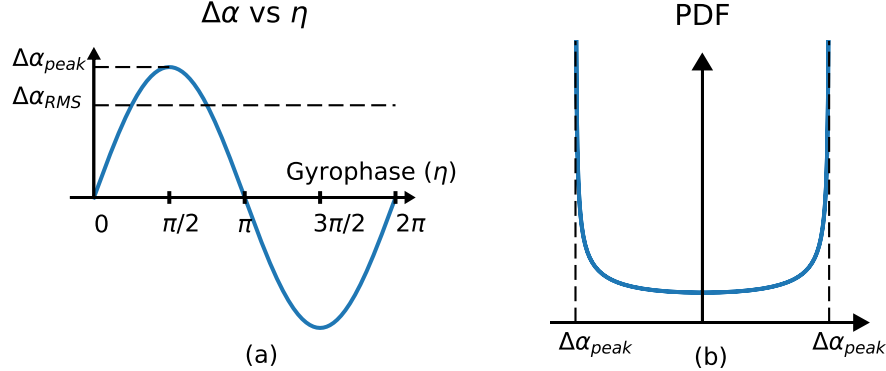


Figure 4.5: (a) Pitch angle perturbation vs particle gyrophase, with $\Delta\alpha_{rms}$ marked, and (b) The corresponding probability density function (PDF, equation 4.10). Modified from *Bortnik* (2005), figure 5.8.

(4.8)

Implicit in this calculation is the distribution in gyrophase, which is taken to be uniform. This allows us to use our RMS pitch angle perturbations in place of an explicit distribution of perturbations across gyrophase. Figure 4.5 (a) shows the assumed pitch-angle perturbation as a function of gyrophase, η , and $\Delta\alpha_{RMS}$. We then convert this distribution to its cumulative distribution function $F(\alpha)$, and its probability density function $f(x)$, shown in figure 4.5 (b):

$$\begin{aligned} F(\alpha) &= P(X < a) = \int_{-\infty}^a f(x)dx \\ &= P((\Delta\alpha_{peak} \sin Y) < x) \\ &= P(Y < \arcsin(x/(\Delta\alpha_{peak}))) \\ &= \frac{\arcsin(a/(\Delta\alpha_{peak}))}{\pi} + \frac{1}{2} \end{aligned} \quad (4.9)$$

$$f(x) = \frac{dF(a)}{dx} = \frac{1}{\pi\sqrt{(\Delta\alpha_{peak})^2 - (a)^2}} \quad (4.10)$$

While $\Delta\alpha(E, t)$ is computed only for particles at the edge of the loss cone, $\alpha = \alpha_{lc}$,

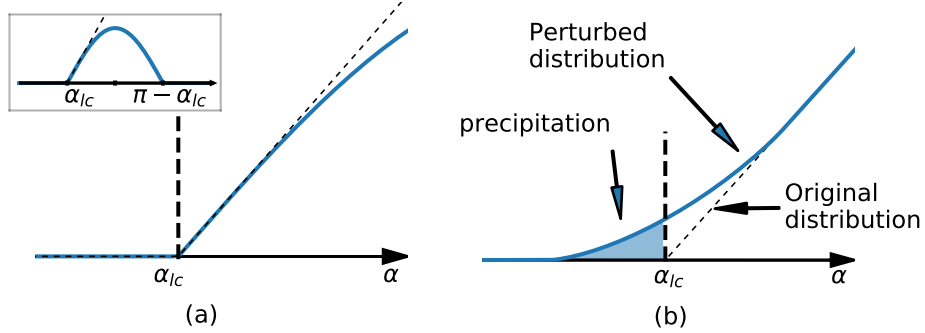


Figure 4.6: (a) The initial pitch-angle distribution function and its linear expansion at $\alpha = \alpha_{lc}$. (b) The perturbed distribution, resulting from the convolution of plot (a) with 4.5(b). The shaded region indicates particles which have been pushed into the loss cone ($\alpha < \alpha_{lc}$). Modified from *Bortnik (2005)*, figure 5.8.

we note that the perturbation varies slowly with respect to initial pitch angle, and that only particles within $\sim 0.1^\circ$ of the loss cone will be scattered into the loss cone, and can therefore apply the same perturbation to the distribution of electrons just inside the loss cone.

The unperturbed particle population is modeled by:

$$G(E, t, \alpha) = G_1(E, t_0)G_2(\alpha) \quad (4.11)$$

where $G_2(\alpha)$ is the dependence on pitch angle, and $G_1(E, t_0)$ is the energy-differential electron flux at the equator for a given energy band E , and time of day t_0 , along the target field line.

We model $G(\alpha)$ with a sinusoidal distribution between $\alpha = \alpha_{lc}$ and $\alpha = \pi - \alpha_{lc}$, as in figure 2.16. The background radiation belt density $G(E, t_0)$ is modeled using the AE8 numerical model for both maximal and minimal filling, as in figure 2.15.

The perturbed flux density $\Phi(E, t, \alpha)$ is given by convolving equations (4.10) and (4.11):

$$\Phi(E, t, \alpha) = f(\alpha) * G(E, t, \alpha) \quad (4.12)$$

Equation (4.12) is evaluated analytically using a linear expansion of $G(E, t, \alpha)$

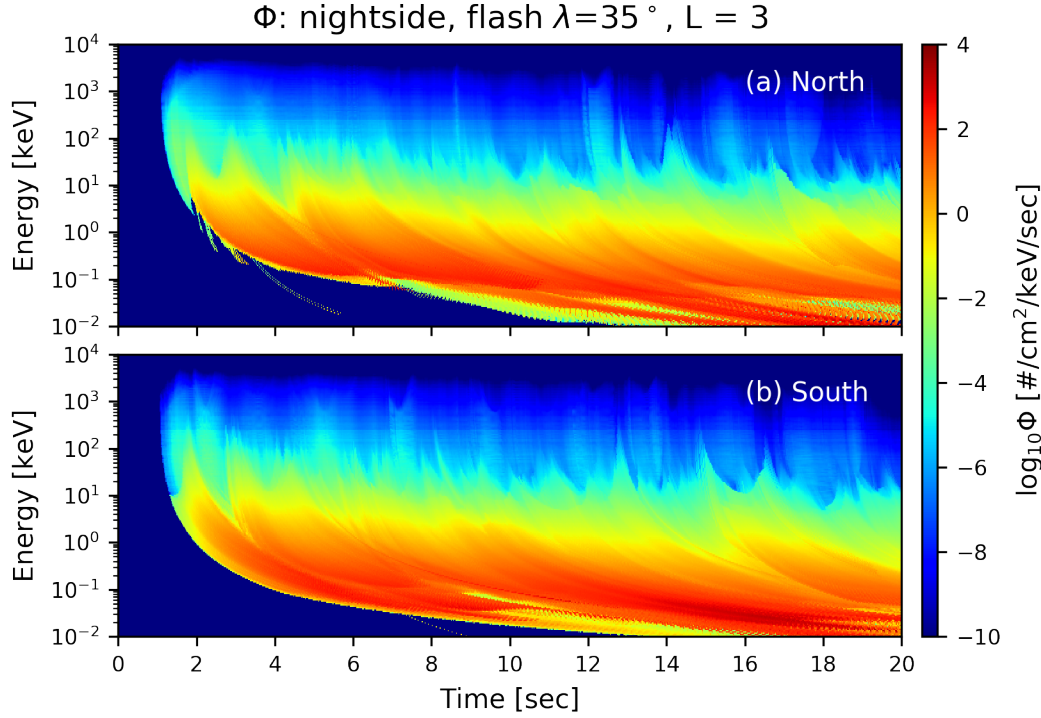


Figure 4.7: Precipitating flux density $\Phi(E, t)$ along a fieldline with $L=3$, for a 10 kA flash at $\lambda_s = 35^\circ$ latitude, through a nightside ionosphere at $K_p = 0$. Scattering is centered directly over the input flash longitude, within a width of $\pm 0.25^\circ$.

about $\alpha = \alpha_{lc}$ (*Bortnik* (2005), figure 5.8, section d).

Total fluxes are derived by integrating over the loss cone solid angle, again following *Bortnik* (2005), including a $\sin^{-2} \alpha_{lc}$ term to account for fieldline focusing, and $\cos \alpha$ to select the plane perpendicular to B_0 :

$$\Phi(E, t) = \frac{1}{\sin^2 \alpha_{lc}} \int_0^{2\pi} \int_0^{\alpha_{lc}} \Phi_p(E, t, \alpha) \cos \alpha \sin \alpha d\alpha d\phi \quad (4.13)$$

$$= \frac{1}{\sin^2 \alpha_{lc}} \int_0^{\alpha_{lc}} \Phi_p(E, t, \alpha) \sin 2\alpha d\alpha \quad (4.14)$$

Figure 4.7 shows an example $\Phi(E, t)$ matrix, as calculated with a 10-kA flash at $\lambda_s = 35^\circ$, for $L=3$.

Table 4.1: Stencil Simulation Parameters

Grid and Interpolation Parameters:	
Fine-scale Frequencies	50
Output L-shell range	1.2 - 8
Output L-shell spacing	0.2
Output longitude offsets	{0, 0.5, 1, 1.5, 2, 5, 10, 20}
Threshold distance from flash	1000 km
Resonant Interaction Parameters:	
Fieldline latitude spacing	1°
Resonant modes	{ -5 .. 5 }
Energy bands	256, log-spaced between 10 eV and 10 Mev

Finally, number flux N and energy flux Q can be calculated by integrating over a desired energy band of interest (E_1, E_2):

$$N(t) = \int_{E_1}^{E_2} \Phi(E, t) dE \quad (4.15)$$

$$Q(t) = \int_{E_1}^{E_2} E\Phi(E, t) dE \quad (4.16)$$

4.3 LEP stencils and the behavior of a single flash

Having developed a method of computing the precipitating electron energy-time spectrum along a single fieldline, we can compute the global precipitation flux due to terrestrial lightning, using a similar “stencil” structure as in chapter 3. We then sum over the time axis to compute the electron flux density in equation (4.14) for each flash, repeating the calculation for a grid of output L-shells and longitudes, for an array of input latitudes, MLT, and K_p .

Table 4.1 lists the various parameters used in the stencil simulation. The collection of guide rays are the same as those in chapter 3.

After integrating over the time axis, the resulting stencils each have dimensions

(lat \times lon \times energy), for both the northern and southern hemispheres. Figure 4.8 shows a set of energy-integrated number flux stencils for a variety of input latitudes and K_p for a 10kA, nightside flash. Figure 4.9 shows the corresponding stencils for the dayside.

By integrating over latitude and longitude, we can compute the total energy precipitated from a single flash, as shown in figure 4.10. A 10-kA flash precipitates on the order of 1 to 10 kJ on the nightside, and 1 to 1000 J on the dayside.

Several trends are apparent in figures 4.8 and 4.9: First, it is apparent that increased K_p has little impact on precipitation, up until high activity ($K_p > \sim 6$). We can attribute this to our plasmasphere density model, which is consistent across K_p values within the plasmapause. Generally, if a flash is launched within the plasmapause (at a latitude lower than that of the plasmapause), then the rays experience relatively little attenuation due to Landau damping in the cold medium, and reflect back and forth several times. Rays launched outside the plasmapause are attenuated much more quickly. The sharp gradient of the plasmapause constrains energy within the plasmasphere, as indicated by the sharp dropoff of precipitation around the plasmasphere latitude. At the highest values of K_p , the plasmapause is brought in to $L \sim$, about 45° , at which point substantial energy is launched outside the plasmapause (and quickly damped), or is very strongly deflected by the plasmapause gradient. The effect of the plasmapause is consistent in both the nightside and dayside stencils.

Examining the dayside stencils in figure 4.9, the increased attenuation of the ionosphere becomes apparent, notably at lower-latitude flashes. The effect of both ionosphere attenuation and of the lower-latitude plasmapause is apparent when looking at the integrated totals in figure 4.10.

Precipitation is not always symmetric between the northern and southern hemispheres. We can attribute any asymmetry in total flux to the relative efficiency of each resonant mode. Higher-order modes ($\pm 1, \pm 2\dots$) are symmetric, with the positive calculation resonating with particles moving in one direction, and the negative with particles moving in the opposite. However, the lowest resonant mode interacts only with counterstreaming particles. Accordingly, precipitation is strongest at the same hemisphere as the incident flash.

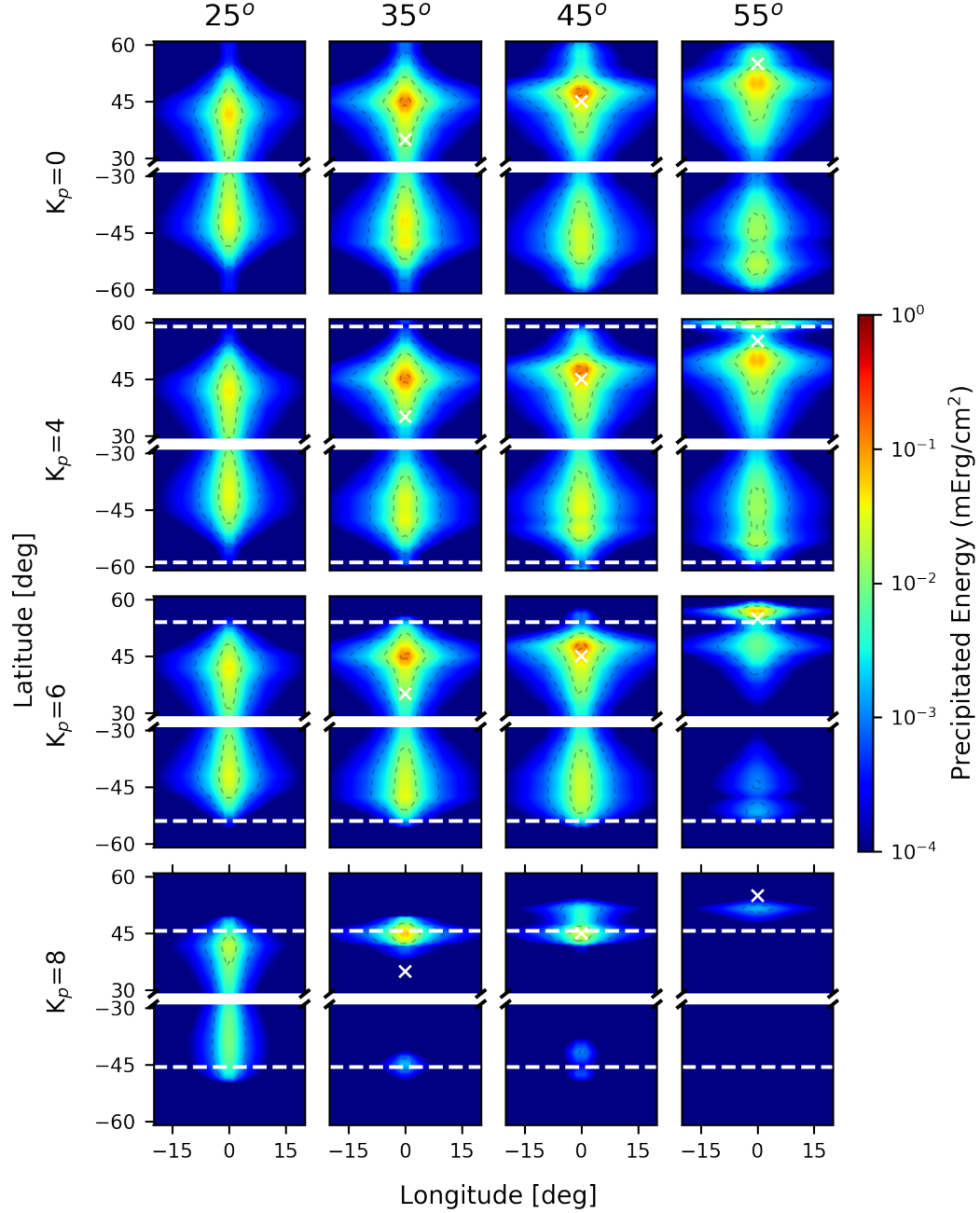


Figure 4.8: Precipitating energy density stencils from a maximally-populated radiation belt model, for a range of flash latitudes and magnetospheric conditions, for a 10 kA nightside flash. The location of the plasmapause is marked with a dashed white line, along the northern and southern hemispheres. The flash location is marked with a white X.

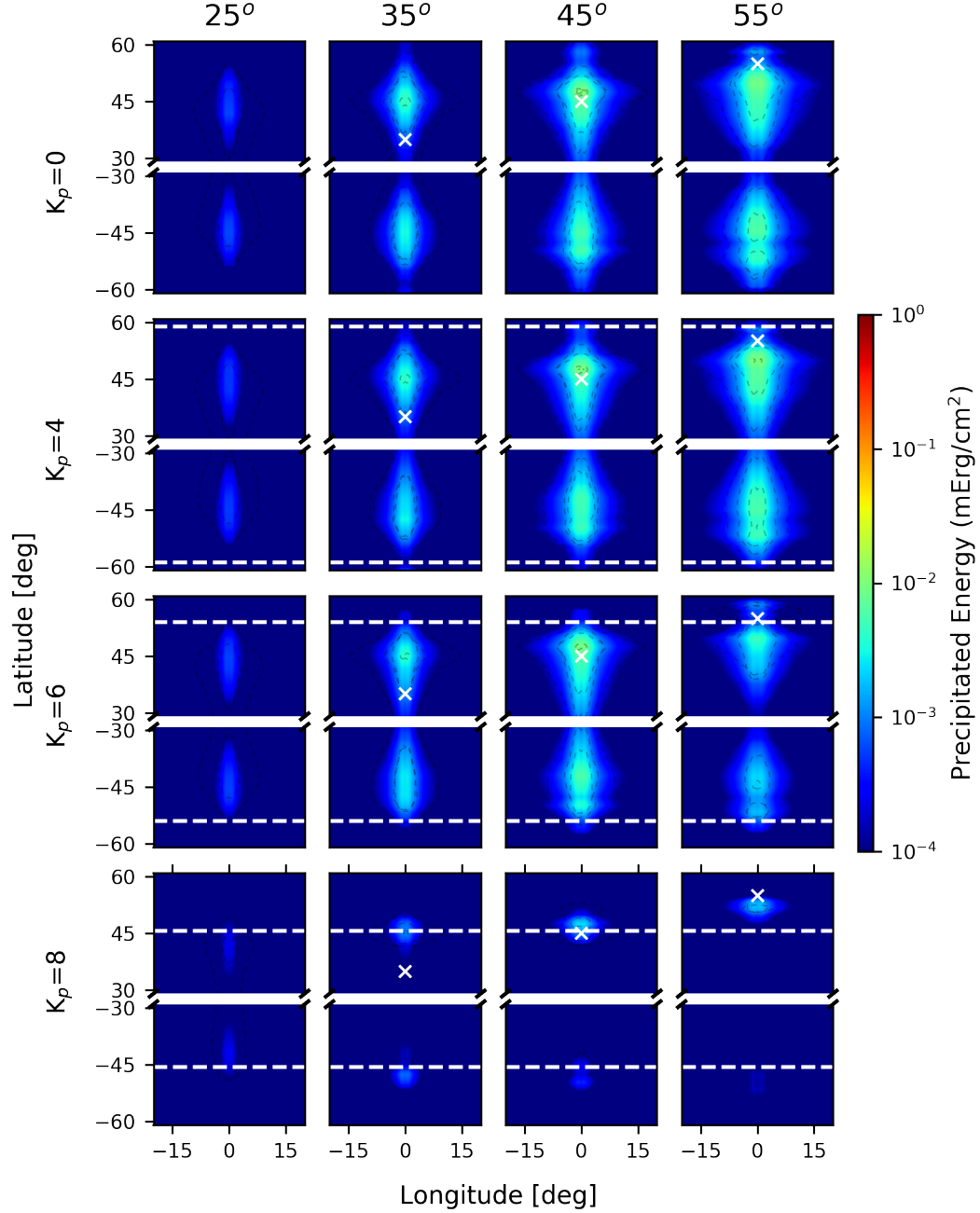


Figure 4.9: Precipitating energy density stencils from a maximally-populated radiation belt model, for a range of flash latitudes and magnetospheric conditions, for a 10 kA dayside flash. The location of the plasmapause is marked with a dashed white line, along the northern and southern hemispheres. The flash location is marked with a white X.

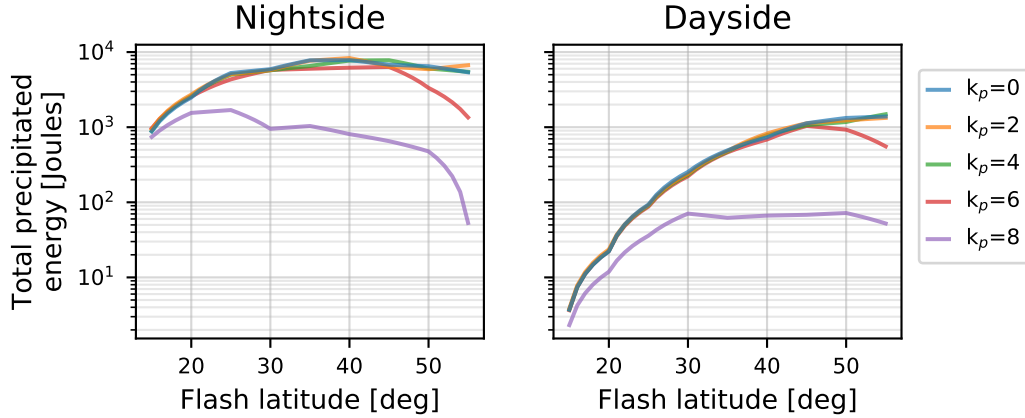


Figure 4.10: Area-integrated precipitation for a single 10 kA flash vs flash latitude, for a variety of magnetospheric conditions. Totals include precipitation in both hemispheres.

In both figures 4.8 and 4.9, precipitation is strongest along a $\sim 0.8^\circ$ offset in longitude, which results from the $\sin^2 \theta$ term in equation (2.38). In this case, θ represents the elevation angle from the flash to the lower ionosphere (taken to be 100 km), which is maximized at $\theta = 45^\circ$. The result is a central null in radiated energy directly above the flash, and maximal radiated energy offset by 100 km in the longitudinal direction.

An additional point of interest is the ratio of precipitated energy in figure 4.10 vs the radiated energy above the ionosphere in figure 3.4. Radiation on the order of megajoules will induce precipitation several orders of magnitude lower in energy.

Finally we can examine the energy spectrum of precipitating electrons, as shown in figure 4.11. As in the precipitation stencil maps, increasing K_p has little effect until very active conditions. The flux is dominated by lower-energy electrons, owing to the stronger scattering of the lowest resonant mode (also visible in figure 4.7).

4.4 Coordinate deformation

The stencils in section 4.3 are computed using a dipole magnetic field, and the simplified GCPM model, both to reduce computational complexity and to better generalize

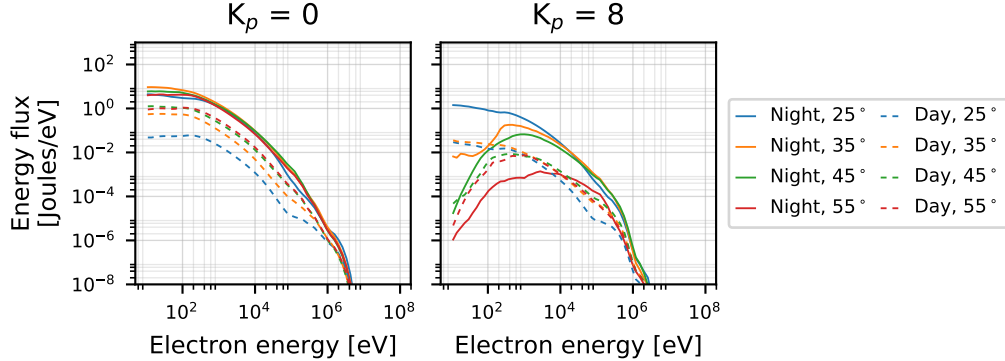


Figure 4.11: Energy spectrum of precipitating electrons, for $K_p=0$ and 8, for a range of input latitudes, for day and night. Fluxes are drawn from the AE8MAX population model.

to multiple longitudes. However, we can approximate the effect of a more-complex magnetic field model via a coordinate transformation, in which we rotate input coordinates to an equivalent dipole-model coordinate, and perform an inverse operation on the stencil output. On the stencil output, this approximation is justified by noting that trapped electrons are bound to their respective field lines, regardless of model used. Justification on the input side (deforming the input coordinates of a lightning flash) is less-concrete, but still a reasonable assumption. First, experimentation with the raytracer reveals that, given a longitudinally-symmetric plasma density model, rays generally follow the longitude deviation of the magnetic field model. Second, while the IGRF and Dipole models differ greatly in its footprint on the ground (as in figure 2.9), within the plasmasphere the two models have reasonable agreement (as in figure 2.8).

The *Corrected Geomagnetic Coordinate* (CGM) (Hakura, 1965) system is especially well-suited for this task. CGM coordinates are defined by fieldline tracing between the IGRF and Dipole models. To transform from geographic to CGM coordinates, we first trace a fieldline using IGRF from the surface, up to its intersection with the geomagnetic equatorial plane. We then follow the dipole model back down to the surface, to get an equivalent dipole-model coordinate. The inverse transformation is accomplished by following the dipole field line back up to the equator, and

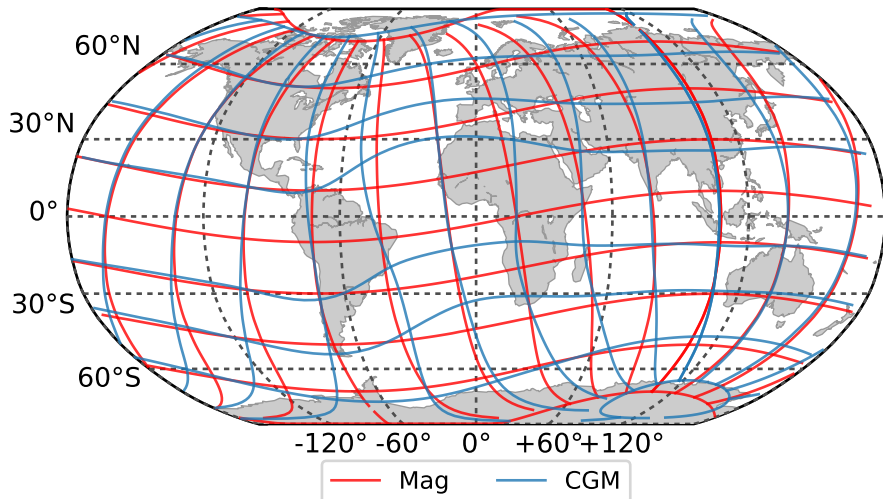


Figure 4.12: A comparison between Magnetic Dipole (MAG) and Corrected Geomagnetic (CGM) coordinates. Corrected Geomagnetic coordinates are obtained by following a magnetic field line, as defined by IGRF, from an input point to its intersection with the magnetic dipole equator. The CGM latitude and longitude are then obtained by following the dipole field line to its footprint on the Earth’s surface. Contours are spaced every 20° in geomagnetic latitude, and 30° in geomagnetic longitude.

the IGRF model down to its footprint (*Laundal and Richmond, 2016*).

Field line tracing is a computationally-intensive task for a coordinate transformation tool. Historically, researchers relied on precomputed lookup tables and interpolation. The Altitude-Adjusted CGM (AACGM) model (*Baker and Wing, 1989; Shepherd, 2014*) uses a spherical-harmonic fit to rapidly transform between CGM and MAG coordinates.

CGM coordinate systems are undefined at some regions near the geomagnetic equator, due to the fact that some IGRF fieldlines may never intersect with it. In these cases, approximate models are often used. *Baker and Wing (1989)* simply omitted geomagnetic latitudes within $\sim 24^\circ$ of the equator from their study; subsequent researchers have performed spline fits and interpolation to further reduce the undefined region.

We use the AACGMv2 algorithm and implementation from *Shepherd* (2014), available at <http://superdarn.thayer.dartmouth.edu/aacgm.html>. Figure 4.12 compares MAG and AACGM contours on a geographic map.

Figure 4.13 shows the relative difference between GLD average current density using MAG coordinates only, vs using the AACGM coordinate transform.

4.5 Global and Seasonal Energy Fluxes

Having computed the precipitation for a single flash across a variety of input parameters, we can examine global energy deposition by shifting, scaling, and summing the LEP stencils according to the GLD360 lightning dataset. The resulting electron precipitation is heavily dependent on the population of radiation belt electrons; rather than leverage historical data, we provide two estimates, using the AE8 model for maximal and minimal filling, in effort to determine the upper and lower bounds on precipitation.

LEP stencils are computed using the parameters in table 4.1. Stencils are computed for canonical 10 kA flashes, in 5° steps in latitude, between 15° and 55° , for dayside and nightside ($MLT = 12$ and 0 respectively), for an array of $K_p = \{0, 2, 4, 6, 8\}$. The resulting stencils are then interpolated onto a fixed $0.5^\circ \times 0.5^\circ$ grid in geomagnetic latitude and longitude, and for all valid values of K_p ($0 - 9$ in ~ 0.3 steps). Noting the relatively quick transition at the day/night terminator, we bin each flash in the GLD360 dataset into dayside or nightside. The 256 energy bands are summed into 64 sub-bands to reduce memory requirements.

Figure 4.14 shows the global average energy precipitation resulting from LEP, for maximum and minimum conditions. Precipitation is integrated over the energy band of interest (10 eV - 10 MeV), and averaged over a three year period between August 2014 and July 2017. We use historical data for K_p , which is reported in three-hour segments.

The pitch-angle scattering model scales linearly with respect to wave amplitude, and therefore scales quadratically with respect to flash peak current. To account for arbitrary peak current values, we scale the resulting precipitation stencils accordingly:

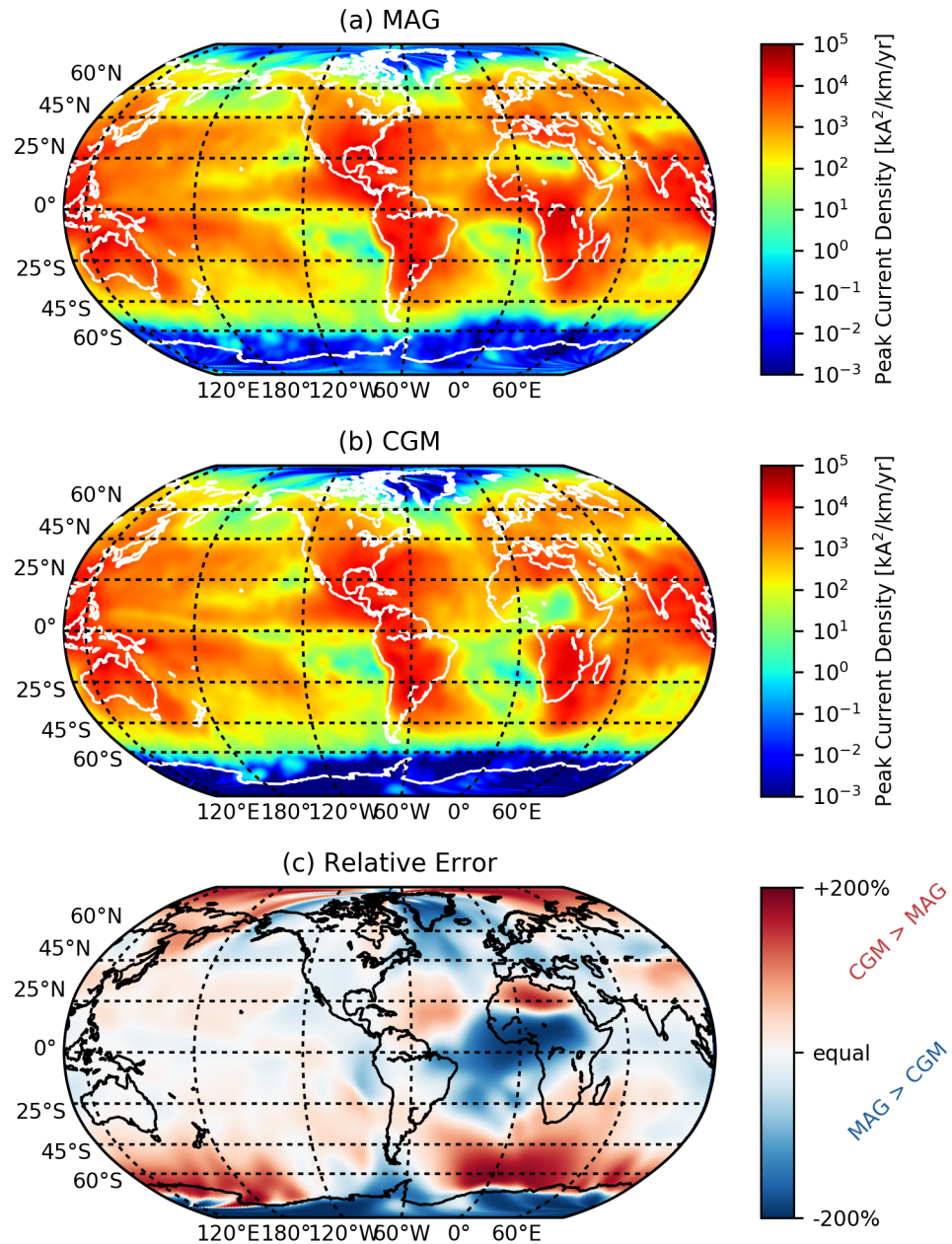


Figure 4.13: Average lightning activity, weighted by peak current intensity, as measured by the GLD360 dataset. Data is averaged from August 2014 through July 2017. (a) the GLD360 data, in geographic coordinates. (b) the GLD360 data, shifted to its equivalent coordinates using the AACGM coordinate transform. (c) the relative error between the two coordinate frames.

$$\phi(I) = \phi(I_{ref}) \frac{I^2}{I_{ref}^2} \quad (4.17)$$

The two sources of stochasticity in our model are 1) the location and intensity of lightning, and 2) the value of K_p . Lightning activity and K_p are generally uncorrelated, as K_p is driven by activity within the magnetosphere, and lightning activity by terrestrial weather patterns. As shown in figures 4.8 and 4.9, fluctuations in K_p have little effect on our precipitation model in most situations ($K_p < 6$). Unexplored in this work, however, is the correlation between radiation belt filling conditions and K_p ; e.g., radiation belt filling events generally occur alongside geomagnetically-active conditions, in which K_p will be high.

By integrating over latitude and longitude, rather than time, we can examine any seasonal trends which may be present. Figure 4.15 shows the global energy flux in kilowatts, across the globe, as a function of time, for maximal and minimal filling conditions. The global energy deposition rate shows very weak seasonal dependence, and can range from a few kilowatts to several megawatts. The disperse energy deposition rate suggests that LEP is not a prominent driver of energy in the lower ionosphere. However, sporadic energy deposition due to LEP is measurable by sub-ionosphere VLF remote sensing (?), and may still be capable of inducing turbulence in the upper ionosphere.

The lack of seasonal dependence, however, suggests that LEP can provide a constant, year-round loss mechanism for radiation belt electrons, especially when considering that radiation belt electrons can drift in longitude around the Earth, on timescales of minutes to days (*Walt, 1994*), and can thereby interact with lightning activity across the globe.

While total global lightning activity is relatively constant, regional lightning is a highly seasonal phenomenon. We can integrate the energetic electron precipitation over the continental United States, to explore seasonal dependence on a finer scale, such as in *Gemelos et al. (2009)*. Figure 4.16 shows the total energy precipitation between $20^\circ - 50^\circ$ in geomagnetic latitude, and -50° to $+10^\circ$ in geomagnetic longitude

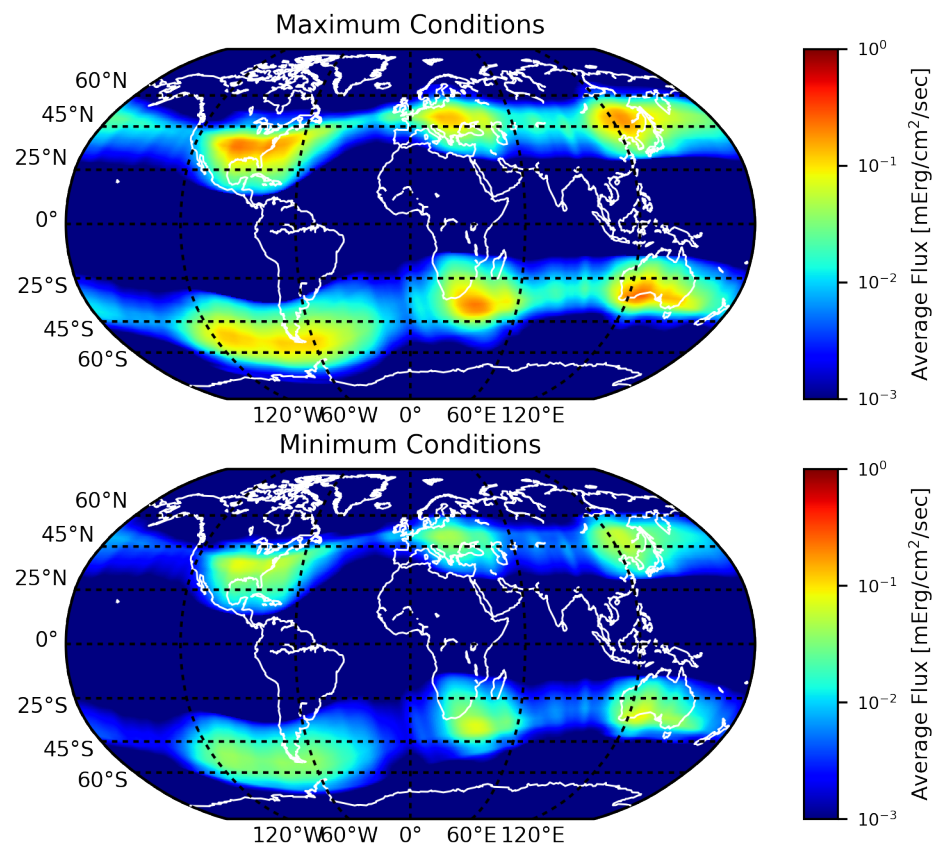


Figure 4.14: Time-averaged energetic electron precipitation “hot spots”, for the GLD360 dataset, between August 2014 and July 2017. Total energy is shown, integrated between 10 eV and 10 MeV.

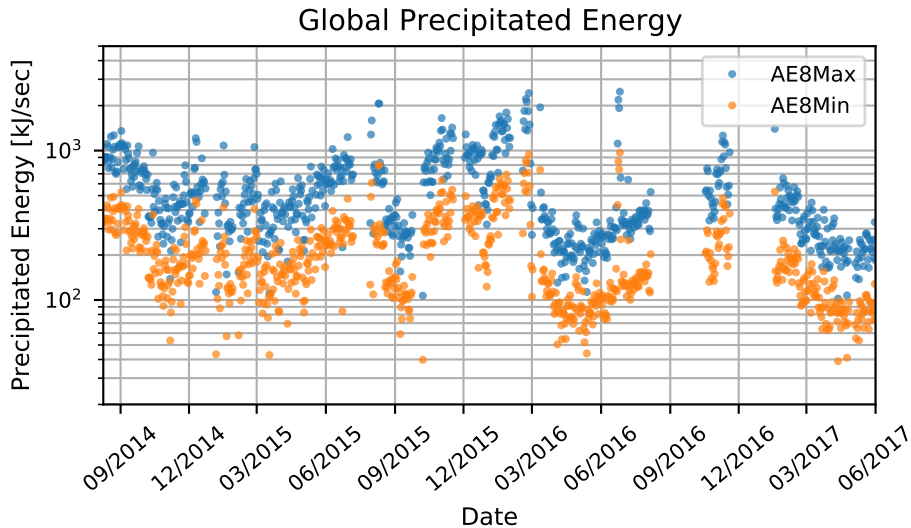


Figure 4.15: Global average energy deposition due to LEP. Precipitation is integrated across the globe, for energetic electrons between 10 eV and 10 MeV.

(approximately over the continental United States). Narrowing our observation window reveals a much greater seasonal variation, peaking in the summer months, and reaching a minimum in December and January.

4.6 Lifetime Estimates

The previous section examined the energy deposition into the ionosphere due to LEP. Next, we consider the relative effect of LEP as a loss mechanism from the populated radiation belts.

Our precipitation model is linearly proportional to the current population of electrons along a given magnetic fieldline, which results in an exponential loss function, parameterized by a time constant τ :

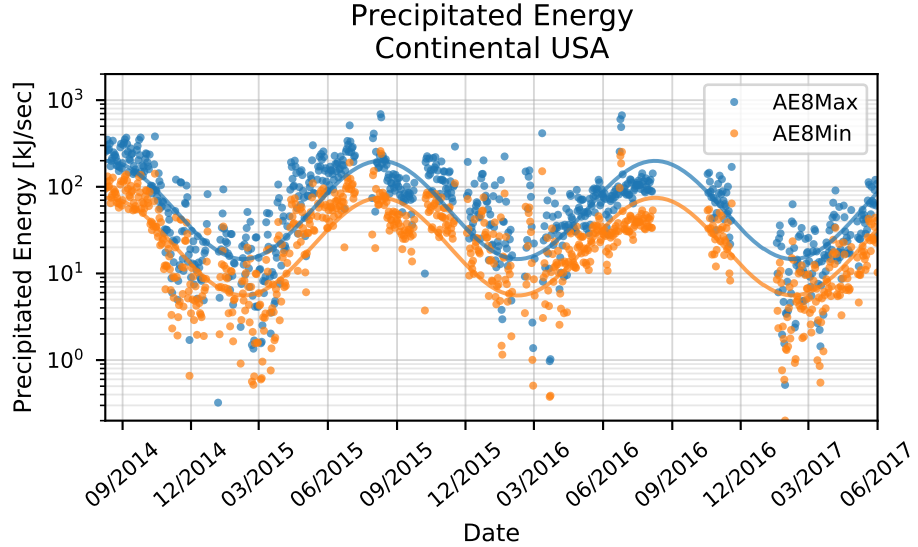


Figure 4.16: Average energy deposition due to LEP over the continental United States (20° to 50° geomagnetic latitude, -50° to $+10^\circ$ geomagnetic longitude). Seasonal variation is much more apparent than in the global integration (figure 4.15).

$$\frac{dN}{dt} \propto N \quad (4.18)$$

$$\therefore N(t) = N_0 e^{-t/\tau} \quad (4.19)$$

$$\frac{dN}{dt} = -\frac{N_0}{\tau} e^{-t/\tau} \quad (4.20)$$

$$= -\frac{N(t)}{\tau} \quad (4.21)$$

$$\tau = \frac{N(t=t_0)}{dN/dt|_{t_0}} \quad (4.22)$$

Once summed over the GLD360 dataset, our model delivers electron losses impinging on a cross-sectional area at 100km, with units [$\#/\text{cm}^2/\text{ev/sec}$]. To compute the percentage loss, we must determine the number of electrons (per energy) which occupy the fieldline above the same cross-sectional area, resulting in $\tau \sim \text{sec}$.

The total electrons along a given fieldline above a cm^2 ionosphere patch is computed by integrating the (energy) differential, omnidirectional equatorial flux, such as from the AE8 model. As in the precipitation code, we ascribe a sinusoidal pitch-angle distribution (e.g., figure 2.16) to the electrons in the omnidirectional flux value.

The AE8 energy-differential, omnidirectional flux models have units $J \sim [\#/cm^2/\text{sec}/\text{ev}]$, which represent the total flux of electrons through a cross-sectional area at the equator, per unit energy. We use a change of variables and integrate over the sinusoidal pitch-angle distribution $P(L, \alpha)$, using the relationship in equation (4.7) to relate an electron's bounce time τ_b to it's pitch angle α and total kinetic energy E .

$$P(L, \alpha) = \begin{cases} \frac{1}{1 - 2\alpha_{lc}/\pi} \sin \frac{\alpha - \alpha_{lc}}{1 - 2\alpha_{lc}/\pi}, & \alpha_{lc} < \alpha < \pi - \alpha_{lc}. \\ 0, & \text{otherwise.} \end{cases} \quad (4.23)$$

$$N_{0,equator} = \int_0^{\pi/2} J(E) P(L, \alpha) \tau_b(L, \alpha) \sin \alpha \cos \alpha d\alpha \quad (4.24)$$

We then convert the integrated value N_0 from an equatorial cross-sectional area to an equivalent cross-sectional area at the ionosphere, using a “crunch” term according to the constricting dipole magnetic field:

$$\epsilon_m = \frac{1}{L} (R_E + H_{iono}) / R_E \quad (4.25)$$

$$C_b = \sqrt{1 + 3(1 - \epsilon_m)} / \epsilon_m^3 \quad (4.26)$$

$$N_{0,iono} = C_b N_{0,equator} \quad (4.27)$$

In order to examine the effectiveness of LEP across all energies, and avoid numerical issues where the AE8 model values are small, we compute an additional set of stencils, using a “flat” radiation belt population, by setting $J(E) = 1 [1/\text{cm}^2/\text{sec}/\text{ev}]$. Figure 4.17 shows the precipitated energy distribution from a flat radiation belt population, in the same format as figure 4.11. The bimodal peaks resulting from the multiple resonant interaction modes are more-readily visible, without the additional loss due to reduced radiation belt populations at higher energies.

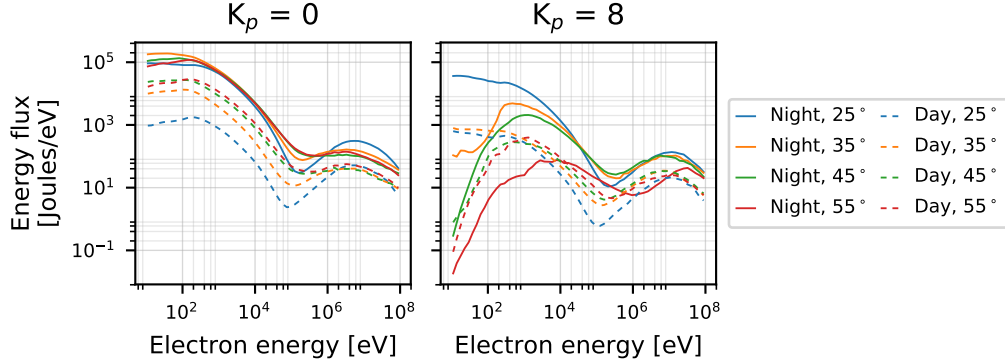


Figure 4.17: Energy spectrum of precipitating electrons, for $K_p=0$ and 8, for a range of input latitudes, for day and night, from a uniform (differential flux = $1/\text{cm}^2/\text{eV}$) fieldline population.

We then compute an equivalent precipitation map using the GLD360 dataset, and the flat-distribution stencils. We average the resulting precipitation over all latitudes to obtain a typical flux estimate. The loss timescale, τ , is then obtained using equation (4.22), with the fieldline population N computed using equation (4.27), and the loss rate dN/dt given by the global average precipitation estimate, both using the flat distribution for J .

Figure 4.18 shows the estimated lifetime for radiation belt electrons, subjected solely to LEP-induced losses, versus electron energy and fieldline.

Two prominent results are apparent in figure 4.18: First, we see two enhancement regions, centered at lower energies (~ 100 eV), and at higher energies (~ 10 MeV). We can attribute this bimodal pattern to the preferential energy bands of each resonant mode, as in figure 4.17. Interestingly, our model shows a null in precipitation effectiveness in the band between 100 keV and 1 MeV; this band has generally been thought to be the dominant precipitation region (Voss *et al.* (1984), Voss *et al.* (1998)). Second, LEP is only an effective loss mechanism for inner belt and slot-region fieldlines ($L < 3$), owing to the much much greater volume traversed by higher- L fieldlines.

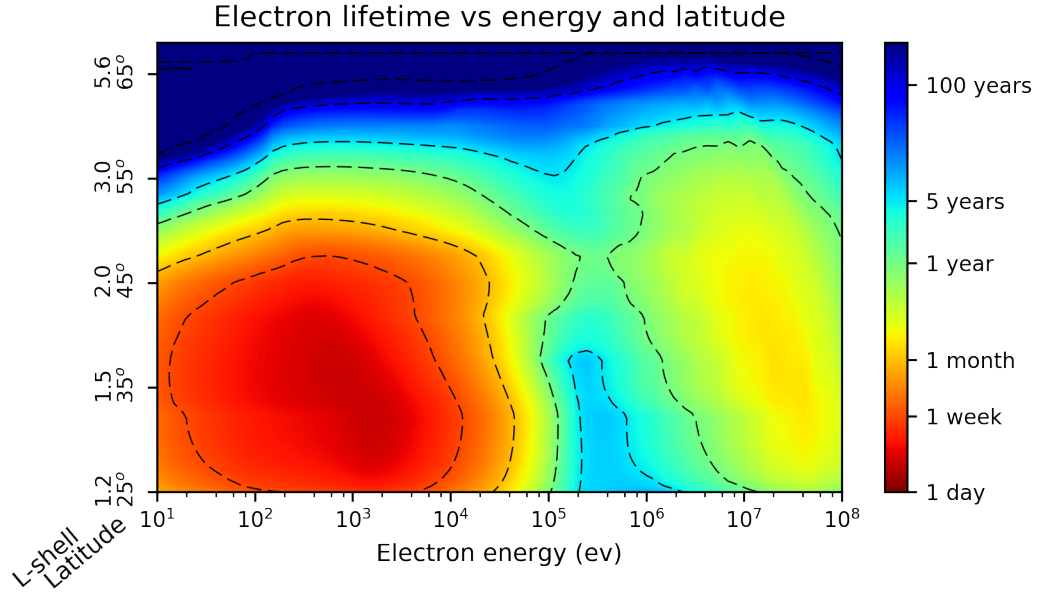


Figure 4.18: Estimated lifetimes (τ , the time required for a population to decay by $1/e$) for radiation belt electrons subjected solely to LEP-induced losses.

4.7 Comparison to other research

We can compare our resulting precipitation estimates to two related works: *Gemelos et al.* (2009) used data from the DEMETER spacecraft, along with seasonal lightning fluxes as measured by the NLDN network, to examine seasonal trends in LEP at 126 keV, and *Meredith et al.* (2007), which uses *in situ* VLF wave measurements to estimate lifetimes of radiation belt electrons due to various scattering mechanisms (LEP, chorus, hiss).

Figure 4.19 shows our modeled electron precipitation at 123 keV for August and December, averaged over 2014 - 2017, along with the corresponding northern hemisphere lightning activity as measured by GLD360, to facilitate comparison with *Gemelos et al.* (2009), figure 1. Geographically, our model shows very good agreement with *Gemelos et al.*; however our modeled fluxes are several orders of magnitude lower. Possible explanations for the discrepancy in precipitation amplitude are that the DEMETER spacecraft orbited at 710 km altitude, while our fluxes are estimated at

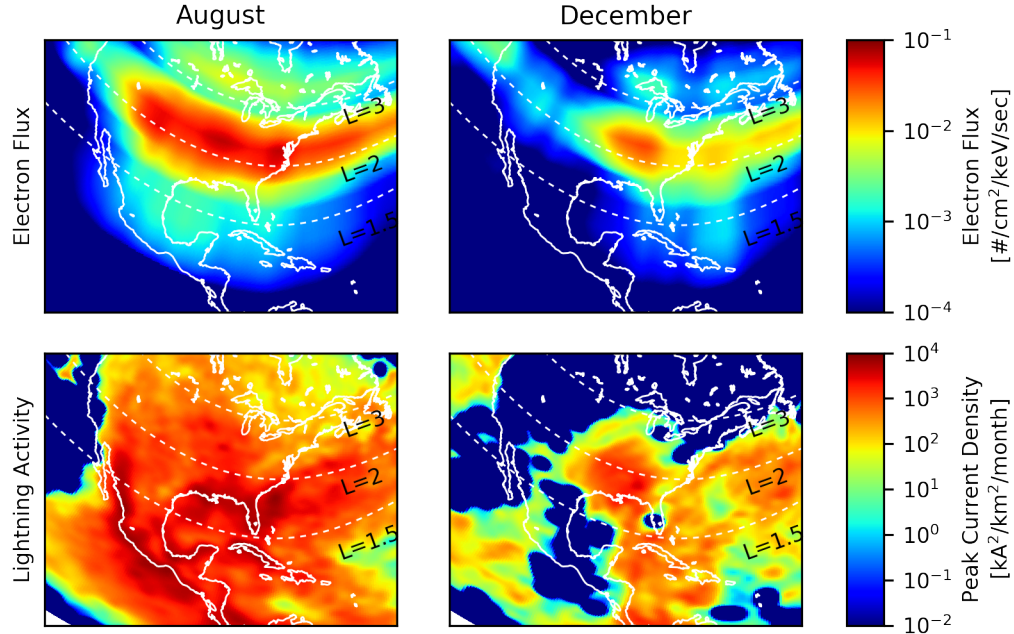


Figure 4.19: Average precipitation at 123 keV over the continental United States, for summer (August) and winter (December). The bottom plots show the corresponding northern-hemisphere lightning as measured by GLD360.

100 km. Additionally, the DEMETER particle detector viewed particles with local pitch angles near $\sim 85^\circ$, and a full-width, half maximum viewing angle of 30° . While this orientation and viewing angle should measure only particles within the loss cone, the detector measures precipitation due to a variety of additional scattering mechanisms beyond LEP.

Figure 4.20 compares our estimated electron lifetimes to those reported by *Meredith et al.* (2007). *Meredith et al.* estimates electron lifetimes using a database of magnetosphere VLF wave measurements from the CRRES spacecraft; they then compute pitch angle scattering using the PADIE code, for a variety of assumed wave conditions. *Meredith et al.* concludes that pitch angle scattering due to magnetospherically-reflecting whistlers (e.g., LEP) is of little relevance to relativistic electron lifetimes.

Our work is somewhat consistent, in that within the specified energy band, both

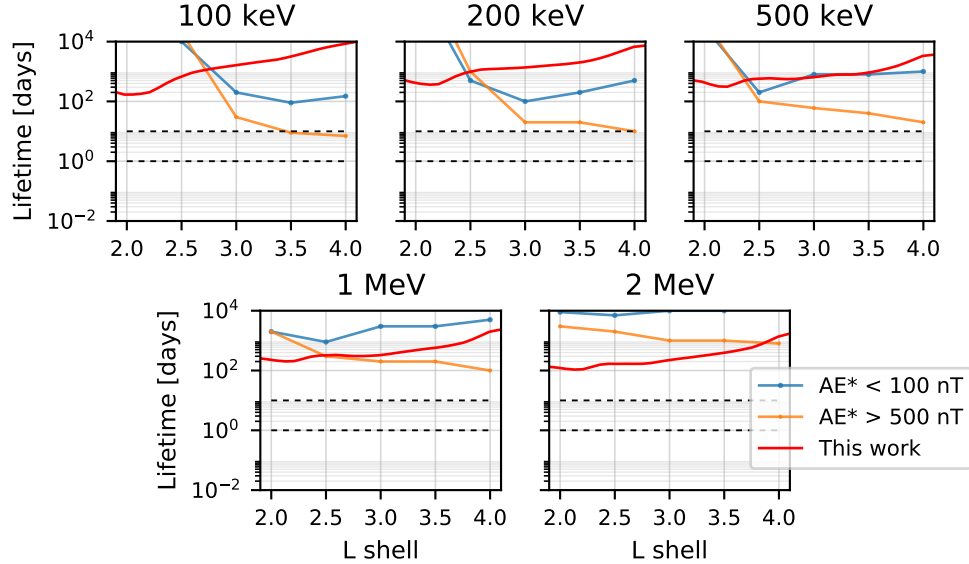


Figure 4.20: Comparison of estimated electron lifetimes with those of *Meredith et al.* (2007). Red lines show our results; blue lines show *Meredith et al.* (2007) estimates for quiet geomagnetic conditions; and orange for active geomagnetic conditions. Dashed black lines indicate the approximate measured lifetime of electrons (1 to 10 days).

works show lifetimes much greater than expected, suggesting that LEP is not a dominant loss mechanism. However, our model does show shorter lifetimes at lower L-shells. Additionally, *Meredith et al.* does not examine lifetimes of lower energy electrons, for which our model shows the strongest losses.

Chapter 5

Satellite Instrumentation for LEP Measurement

Having discussed the various steps in the LEP process, and the nuance required in modeling, we now turn to a more-practical discussion, regarding direct measurement of pitch-angle scattering due to wave-particle interactions.

The following chapter represents somewhat of a detour from the preceding chapters. In the first few years of my time at Stanford, I worked on a hardware design for a CubeSat-based measurement platform, designed specifically for the study of these interactions. The project, named the VLF Wave-Particle Precipitation Mapper, or VPM, formed a nexus of several research projects within the Stanford VLF group – numerical modeling, fault-tolerant chip design, and embedded systems development – and granted our small team of graduate students and research scientists design experience for a space-based mission.

In order to quantify the relative effect of waves on particle distributions, one needs to measure two quantities: The incident wave, in the form of electric and magnetic fields, and the pitch angles of the particles impinging on the satellite. VPM samples the wave by measuring two of the six wave components – one E and one B measurement, perpendicular to each other – and the distribution of pitch angle distribution using two electron spectrometers, oriented such that one samples only particles within the loss cone, and the other only trapped particles.

The VPM team was led by Dr. Robert Marshall and Dr. Ivan Linscott; the bulk of the hardware design was done by Jeff Chang and Steven Ingram. Additional software and hardware design was done by Christopher Young, Jordan Lenoach, and Alex Cousland. My primary contribution was the design and implementation of all the onboard firmware and digital signal processing. Design of the electron pitch-angle spectrometer system was contracted to a group at Lockheed Martin, as we lacked the facilities or the expertise to work with energetic particles.

Our design was dictated by two primary constraints: 1) Design with the ability to exchange all commercial-grade components with space-rated components, and in an effort to reduce the risk of catastrophic computer failures, 2) that the system include no embedded firmware or programs stored in volatile memory. These constraints left a marked imprint on our final design. In a sense, we designed for a conventional satellite mission, with the notable exception that our instrument was small.

Were I to do this project again, from scratch, I would strongly advocate following the CubeSat ethos: Sacrifice bulletproof reliability in exchange for rapid design and prototyping, and affordability of flight components. CubeSat missions generally fly in low-earth orbit (~ 400 km altitude), and have mission lifetimes on the order of a few years, at maximum, due to atmospheric drag. While the idea of a fully radiation-tolerant design is alluring, it is hard to justify the price increase in parts (often $\sim 1000 \times$ greater), and the difficulty in designing for them, for a short-duration, academic mission.

This chapter was mostly written shortly after delivery of the initial VPM prototype, in January, 2015. Both VPM and DSX were delayed several years afterward; as of writing, VPM has been picked up by a new group at AFRL, and is slated to launch in January, 2019.

5.1 VPM Mission Overview

The VLF Wave and Particle Precipitation Mapper (VPM) is a 3U CubeSat designed to measure wave activity and relativistic electrons in the Earth's radiation belts from low-Earth orbit (LEO). The VPM payload consists of an electric field dipole antenna

and a magnetic field search coil to measure waves in the VLF frequency band from 100 Hz to 30 kHz; and two electron detectors, designed to measure electron energies from 100 keV to 1 MeV. In addition to single-spacecraft scientific goals outlined below, VPM is a companion to the Wave-Induced Precipitation of Electron Radiation (WIPER) experiment on the Demonstration and Science Experiments (DSX) mission (*Schoenberg et al.*, 2006; *Spanjers et al.*, 2006), a small spacecraft designed to investigate the Earth’s radiation belts using active probing techniques. Both spacecraft are scheduled to be launched in 2019.

VPM will study the Earth’s radiation belts from Low-Earth Orbit (LEO). The radiation belts are comprised of relativistic electrons from hundreds of keV to tens of MeV, and protons from tens to hundreds of MeV. These energetic particles can be highly damaging to spacecraft and to astronauts (e.g. *Barth et al.*, 2003), and comprise a vital component of space weather which affects satellite navigation and communication (*Bothmer and Daglis*, 2007). The distribution and evolution of radiation belt populations are controlled by geomagnetic activity and by wave activity in the plasmasphere. Radiation belt particles can be scattered in energy and pitch angle by magnetic reconfiguration, and by wave activity, which can include Alfvénic, electrostatic and electromagnetic waves. Waves can energize these particles, or cause them to precipitate and be lost to the Earth’s upper atmosphere. The extent to which wave activity of different sources controls radiation belt distributions and lifetimes is still under considerable investigation. For example, the current Van Allen Probes (VAP) mission, launched in 2012, is particularly investigating the processes that accelerate and transport radiation belt electrons; radiation belt loss mechanisms; and the effects of geomagnetic storms on the radiation belts (*Spence et al.*, 2014).

Specific science goals of the VPM mission are:

1. Improve climatology models of plasmaspheric hiss
2. Conduct conjunction experiments with the DSX mission and WIPER instrument
 - (a) Measure the Antenna Radiation Pattern of the WIPER VLF transmitter known as the TNT (Transmitter, Narrow-band receiver, and Tuners)

- (b) Measure the Radiation Efficiency of the TNT
 - (c) Estimate the efficiency of Wave-Particle interactions using WIPER-injected waves
3. Improve understanding of the effects of Lightning in the near-Earth space environment
 - (a) Improve climatology models of lightning and whistler activity
 - (b) Estimate the efficiency of lightning whistler-induced wave-particle interactions
 4. Improve understanding of the effects of VLF transmitters in the near-Earth space environment
 - (a) Measure the efficiency of propagation in the earth-ionosphere waveguide and leakage into the ionosphere and magnetosphere
 - (b) Estimate the efficiency of VLF transmitter whistler-induced wave-particle interactions
 5. Measure the trans-ionospheric absorption of lightning-generated sferics and whistlers
 6. Measure VLF wave propagation characteristics in the near-Earth space environment
 7. Validate models of wave-particle interactions

Here we present the design of the VPM payload instrumentation and data processing, with an emphasis on the VLF wave instrumentation and data processing unit. The VPM payload is unique in a number of ways: i) four science instruments have been collocated in 1.5U of payload space; ii) all data processing is handled in firmware, reducing the power requirements and eliminating any software from the payload; and iii) data products are delivered with maximum flexibility thanks to the unique implementation of processing methods. These unique aspects of VPM will be discussed in sections to follow.

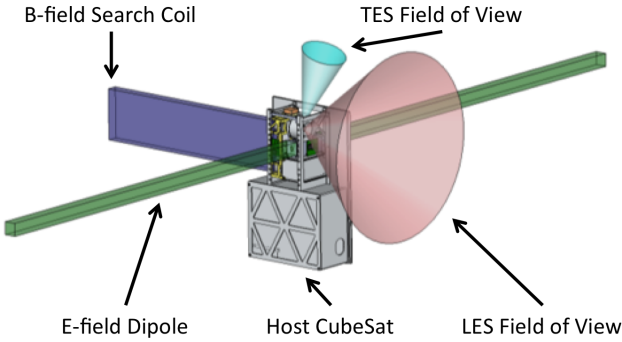


Figure 5.1: Drawing of an assembled VPM payload, shown in one possible configuration integrated into a 6U CubeSat bus, with both antennas deployed. Conical shapes indicate fields of view of the Lost-Electron Spectrometer (LES) and Trapped Electron Spectrometer (TES).

5.2 Hardware Architecture

VPM's system design was governed by three primary constraints:

1. Facilitate integration with a 3U CubeSat bus. The payload must fit into a 1.5U (10x10x15 cm) volume. The bus provides 3.3v and 5v power rails, an RS422 connection, and a single, 1-Hz-sampled analog connection.
2. Provide an upgrade path for high-reliability, radiation-tolerant components wherever possible.
3. Design simple operation modes with high reliability and low verification complexity.

The VPM payload consists of five hardware systems:

1. a power and interface board
2. a two-channel VLF broadband receiver (μ BBR)
3. two deployable VLF antennas for sampling the electric and magnetic field respectively

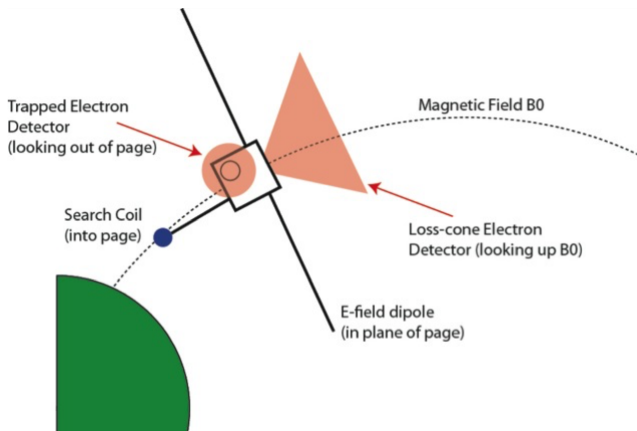


Figure 5.2: Illustration of on-orbit alignment of the VPM payload. Conical, salmon-colored shapes indicate fields of view of the electron spectrometers; E and B fields are sampled perpendicular to each other and to the background magnetic field.

4. a digital data processing system (DPU)
5. and a Loss-Cone Spectrometer (LCS), a pair of electron energy spectrometers designed to sample the energy distribution of the local loss cone.

All circuit boards are connected by a common stack connector and housed in an aluminum enclosure to reduce parasitic RF interference. A rendering of the system is shown in figure 5.3.

5.2.1 FPGAs

Full-scale space systems commonly use radiation-tolerant, multiple-redundant single-board computers. While robust and flight-verified, such systems are cost, size, and power-prohibitive for a cubesat mission. Several commercial cubesat single-board computers exist (such as those from Pumpkin or Tyvak); however these systems are designed for general satellite operations, and provide more functionality than necessary for an isolated payload. Additionally, single-CPU solutions are not well-suited for realtime, parallel streaming tasks, as data from multiple sources must be buffered and processed serially, increasing memory and clock speed requirements.

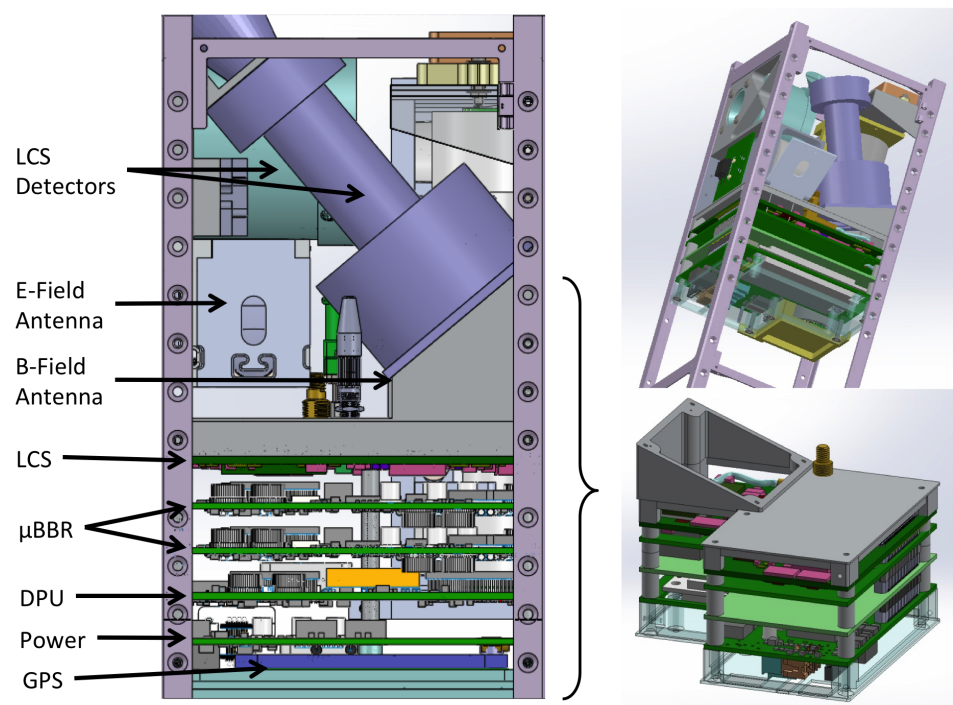


Figure 5.3: Rendering of the VPM payload hardware, showing locations of the E and B-field antenna deployers; the two particle detectors for the Loss-Cone Spectrometer, and the electronic card stack, shown without aluminum enclosure.

VPM omits any such embedded CPU and instead uses a realtime streaming solution implemented entirely in a Field-Programmable Gate Array (FPGA).

FPGAs consist of a network of assignable logic gates and interconnections, which allow for gate-level circuits to be implemented using a hardware development language such as VHDL or Verilog, achieving ASIC-like performance without the burden of IC development. By working at the gate level, multiple-input designs can operate in clock-cycle-accurate lock step, allowing for low-power designs with minimal wasted circuitry. Additionally, gate-level designs inherently have fewer operating states, and once implemented, provide a high degree of reliability without risk of segmentation faults, memory leaks, or other higher-level issues common in CPU systems.

FPGAs find common use in embedded systems for peripheral interfacing and low-level data handling. A hybrid CPU / FPGA design was considered, wherein a “soft” CPU is implemented within the FPGA fabric – however such a design needlessly increased verification complexity, while similarly reducing system reliability. It should be noted, however, that VPM acts only as a peripheral for a separate satellite bus, and is not tasked with a myriad of other responsibilities required of a satellite mission – telemetry, communication, power management and so forth – the complexity of which necessitate a full CPU solution.

VPM uses the Actel ProAsic3 series of FPGAs. Actel FPGAs were selected largely for their focus on reliability, and simple upgrade path to a radiation-tolerant model. Development and prototyping was done using an A3PE/3000 chip (the largest available at time of design), which provides 3 million gates assignable in 75,264 tiles, and 604 kilobits of onboard SRAM . Additional functionality onboard the ProAsic3 series include clock conditioning circuits, differential signaling drivers, and 1 kilobit of flash ROM used to store lookup tables, which combined allow for a single-chip data processing system.

5.2.2 Power and GPS

The lowest circuit board in the VPM stack houses power systems, antenna deployer drivers, and a GPS daughterboard. VPM requires three power connections from the

host spacecraft – +5v, +3.3v, and an unregulated, high-current-capacity supply at \approx 9v, on a single micro-D connector. Additional connections are provided for two antenna deployers. A 100-pin stack connector is used for all inter-board power and communication.

VPM contains two deployable antennas – a 1-meter flexible dipole antenna for sampling the electric field, and a magnetic-field search coil, which is deployed away from the system to reduce parasitic noise. Both antennas are tensioned and held in place using a burn-wire deployer in which a thin plastic filament is held against a conductive wire. To deploy, VPM drives a current through the wire until the plastic filament melts through, allowing the antenna to extend on its own.

The power and GPS board contains two drive transistors to provide the necessary burn-wire current, and are fed from the unregulated supply. Connections are made to deployers via a pair of micro-D connectors.

Bipolar $\pm 12v$ power for the loss-cone spectrometer and searchcoil preamp is provided via a Picosat DC/DC converter.

GPS timing and location are provided by a NovAtel OEM615 embedded GPS receiver. While not radiation-tolerant, this card has flight heritage on multiple CubeSat and nanosatellite missions, and can be configured to operate without altitude restrictions (*Spangelo et al., 2013*).

5.2.3 DPU

Data processing and system commanding is performed on the DPU board. The DPU board contains a single Actel A3PE/3000 FPGA housed in an FG484 ball-grid array package. Local power for the FPGA is supplied by linear regulator circuits – 3.3v and 2.5v for IO banks, and switchable 1.5v or 1.2v for the FPGA core voltage, depending on whether an A3PE or A3PL part is populated. The FPGA is programmed through a 10-pin JTAG header.

Clocking onboard the DPU is provided by a 20 MHz temperature-controlled oscillator, which feeds a clock-conditioning circuit on the FPGA. Processing is done at a divided 10 MHz clock, with the exception of memory operations which operate at

full speed.

Temporary data storage is provided by a 3D-Plus 128-megabyte SDRAM, which is clocked and controlled by firmware within the FPGA. The 3D-Plus SDRAM was selected primarily for availability of a pin-compatible, radiation-tolerant upgrade. The SDRAM uses a 32-bit wide data buss, and includes an internal refreshing algorithm.

Communication between VPM and the host satellite is implemented using a standard UART protocol over an RS422 connection, made through a pair of differential line drivers, again selected for a pin-compatible radiation-tolerant upgrade.

VPM provides low-level housekeeping and debug signals over an analog connection, intended to be sampled by the host spacecraft. A variety of signals are connected through an analog multiplexing chip, including analog and digital power rails; system temperature as measured by a thermocouple near the GPS receiver; the bipolar 12v supply; and five channels allocated to the loss-cone spectrometer. Outputs can be selected via a system command, or set to cycle through at 5 seconds per input.

RS422 and analog housekeeping connections are made through a single micro-D connector. Connections are provided for an FTDI UM232H USB interface used extensively in development; however on flight, all connections are made through micro-D connectors or the 100-pin stack connector.

5.2.4 VLF Receiver Boards

VPM uses a modified version of the Stanford Micro Broadband Receiver (μ BBR) as used on the SpriteSat mission, and the GLIMS payload onboard the International Space Station (*Ushio et al.*, 2011). The VPM μ BBR provides two channels of amplification, filtering, and digitization at an 80 kHz sampling rate. VPM uses a pair of proprietary chips – a combination low-noise amplifier (LNA) and anti-aliasing filter (AAF), and an analog-to-digital converter (ADC) – which were the result of two PhD theses (*Wang*, 2009; *Mossawir*, 2009). The chips were designed for low power consumption and high radiation tolerance.

An intermediate buffering stage provides an additional 10 V/V gain; an active two-pole high-pass filter with a 3-dB point at 3 kHz can be inserted between the LNA and

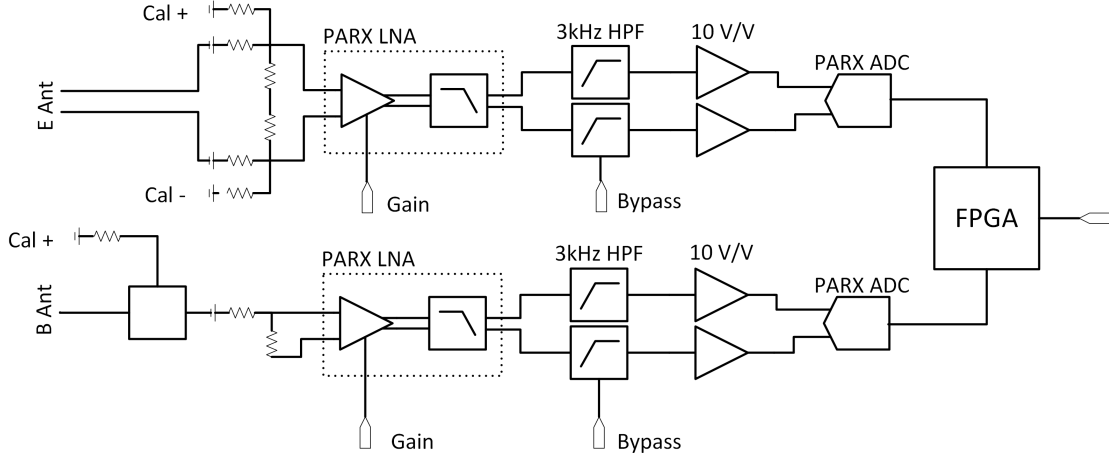


Figure 5.4: Simplified schematic of the μ BBR signal conditioning and data conversion chain

ADC sections, or bypassed completely using sealed, mechanical relays. Gain at the LNA can be remotely selected, either 1 or 10, for a total system gain of 20 or 40 dB. The assembled system gives a spurious-free dynamic range (SFDR) of approximately 55 dB across the passband. The analog stage operates on a single, 2.5v supply, which is derived locally using a 2.5v reference source and a radiation-tolerant op-amp. A simplified schematic of the receiver chain is shown in figure 5.4.

Channel 1 features a differential input, which is capacitively coupled to the electric dipole antenna. Channel 2 is single-ended, and connects to the output of a magnetic-field search coil, which contains its own active signal conditioning circuitry. Filtering and amplification is done differentially, using parallel single-ended circuits.

The ADCs use a 5-stage pipeline architecture; digital assembly and calibration of the first three stages is performed in an FPGA. The resulting FPGA module returns 13-bit equivalent resolution, packed as 16-bit samples (*Wang, 2009*).

Signal conditioning and ADC are located on a single board, which feed an interstitial FPGA on a second board. Parasitic coupling between the two channels is reduced by constraining each channel to a separate side of the board, with a ground-plane layer separating the two.

The μ BBR FPGA receives system and sampling clocks through the 100-pin stack

connector, by way of the DPU FPGA. When enabled, the 80 kHz sampling clock is generated by the GPS card and is accurate to ± 50 nanoseconds. Should the system fail to detect a GPS-synchronized clock for more than 6 seconds, the system will attempt to reset the GPS card. If three resets are attempted without success, the system will default to an internally-generated sampling clock, which is derived from an onboard oscillator. GPS synchronization can be re-enabled via a system command.

All digital communication between the μ BBR and the DPU is done via differential (LVDS) signaling. All communication is done synchronous to the DPU system clock, to eliminate communication errors due to clock and temperature drift.

Calibration Tone

The μ BBR signal chain features an onboard calibration signal generator, which can be used to assess the frequency response of the system on-orbit. A pseudorandom digital signal is generated using the μ BBR FPGA, using the feedback register methodology described by *Paschal* (2005). VPM uses a 7-bit feedback register for a maximal-length sequence of 128 samples. This signal is passed through a voltage divider and capacitively coupled to the input of each analog channel. The Fourier transform of the resulting signal features a comb of uniformly-spaced frequencies, as shown in figure 5.5. When calibration mode is entered, the system will generate one minute of calibration tone, which can be recorded by a 30-second, full-resolution burst. Results of a typical calibration are shown in figure 5.6.

Finally, an onboard digital sine-wave generator can be enabled; in this mode the μ BBR ignores any analog signal and delivers a full-scale sine wave. While not scientifically useful, this mode enables diagnosis of communications issues, and confirmation of survey-mode processing.

5.2.5 Deployable Antennas

VPM contains two deployable antenna structures, oriented perpendicular to each other and to the background magnetic field, which facilitate discrimination of electromagnetic waves from evanescent fields. The electric dipole antenna was designed

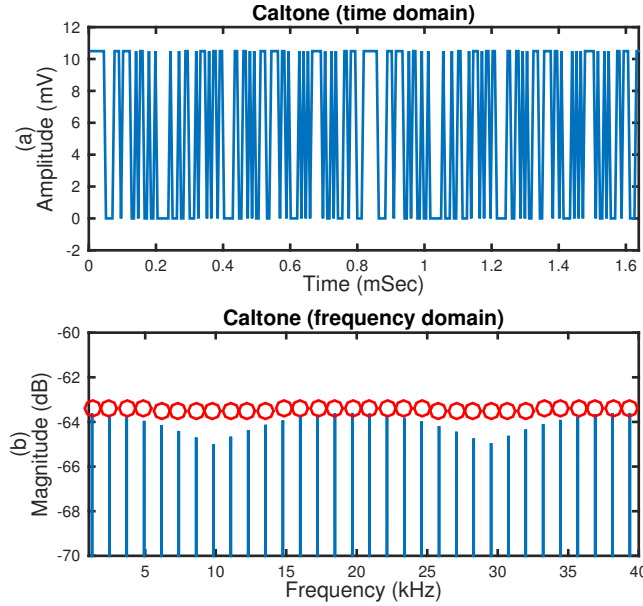


Figure 5.5: Pseudorandom calibration signal. Plot (a) shows two repetitions of the signal in the time domain, with magnitude attenuated from the 3.3v LVDS pin; plot (b) shows the Fourier transform of the signal. Red circles denote total power summed from adjacent frequency bins, to account for windowing effects.

by the Deployable Structures team at the Air Force Research Lab (AFRL), while the magnetic field antenna and apparatus was designed by the French Climate Research Laboratory at the National Center for Scientific Research (CNRS).

The electric dipole antenna is comprised of a conductive strip on a flexible tape, which is rolled up and held in place with a burn wire.

In the presence of a plasma, the electric dipole antenna's impedance can vary substantially with plasma parameters (density, temperature), and orientation with respect to the background magnetic field. For analytic, closed-form expressions, see *Balmain* (1964), and the series of papers by *Wang and Bell* (*Wang and Bell*, 1969, 1972). For a full numerical treatment of plasma-immersed VLF electric dipoles, see the thesis work of *Chevalier* (*Chevalier*, 2007).

For purposes of system characterization, we assume the antenna and receiver are perfectly matched; assuming an infinite plane wave with right-angle incidence and ignoring plasma effects, the conversion between input voltage at the μ BBR terminals

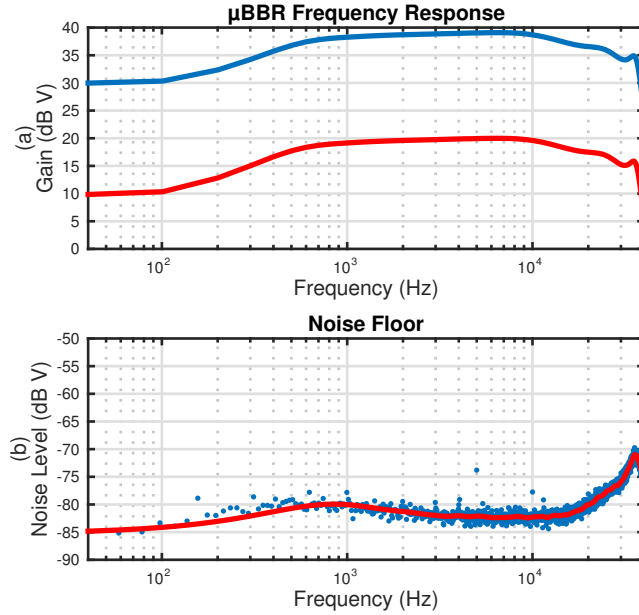


Figure 5.6: Characteristics of the μ BBR analog signal conditioning chain, beginning with the LNA/AAF. Plot (a) shows the frequency response for both high and low gain settings. Responses of the antennas are not taken into account. Selectable high-pass filters are disabled. Plot (b) shows the power spectrum of the noise floor, which is effectively independent of gain setting. Level is in decibels relative to ± 1.0 volts full-scale.

and electric field magnitude V_{in}/E_0 (Volts per Volts / meter) is ≈ 1 .

The search-coil antenna is also deployed from the payload to reduce electrical interference. The antenna includes a dedicated preamp which operates on ± 12 v power. Sensitivity of the antenna and preamplifier are shown in figure 5.7.

Both antennas use a single-deploy burn-wire system. VPM includes options for each deployer to be armed and deployed separately, and can be repeated in the event that the retaining filament fails to release the antenna.

Deployed antennas are shown in figure 5.1.

Figure 5.8 gives a rough estimate of the maximum and minimum detectable field amplitudes. Maximum levels are calculated assuming the low gain setting and a clipping voltage at the ADC; minimum levels are those which are below the system's noise floor at the high gain setting. Note that, for a plane wave in free space, the

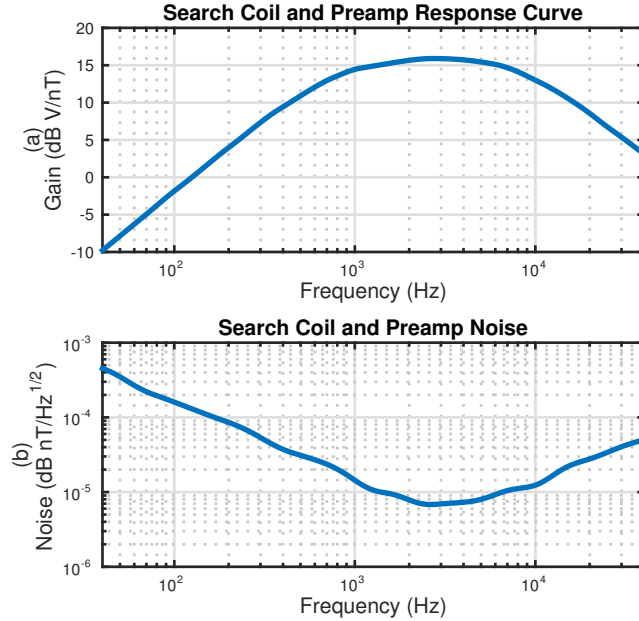


Figure 5.7: Characteristics of the search coil and associated preamp. Plot (a) shows the transfer function in dB-scaled volts per nanotesla. Plot (b) shows the search coil and preamp's noise spectral density in units of nanotesla per $Hz^{1/2}$

magnitudes of E and B are related by $B_0 = \frac{E_0}{c}$, where c is the speed of light; For an electric field $E_0 \approx 1$ V/m, the corresponding magnetic field has $B_0 \approx 0.3$ nT.

The range of measurable amplitudes is comparable to other in-situ VLF measurement systems; DEMETER reports a minimum sensitivity of 2×10^{-5} nT-Hz $^{-1/2}$ (*Cussac et al.*, 2006). The Electric Fields and Waves (EFW) instrument onboard the Radiation Belt Storm Probes (RBSP) satellite use 100-meter double probe sensors with a maximum detection amplitude of ± 1 V/m (*Wygant et al.*, 2014). Several other studies report phenomena within the VLF band (whistlers, chorus) to have amplitudes on the order of 20 mV/m and 1 nT (*Wygant et al.*, 2014; *Cattell et al.*, 2015; *Bhattacharya et al.*, 2009).

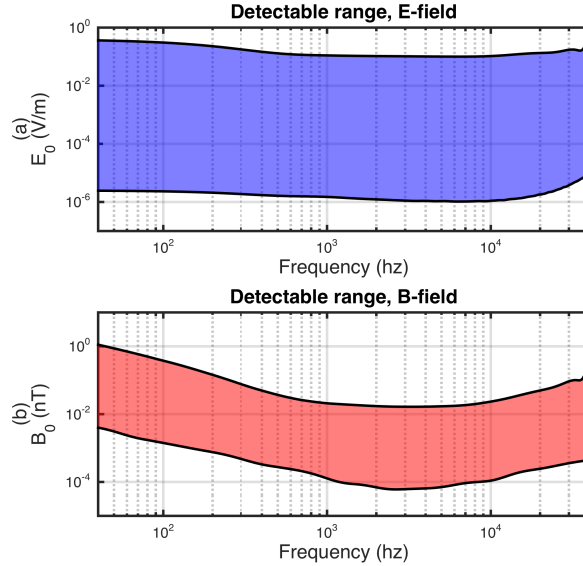


Figure 5.8: Approximate detectable field magnitudes, assuming no loss due to geometric factors of the antennas. Plot (a) shows the range of electric field strengths E_0 in Volts / Meter. Plot (b) shows the range of magnetic fields in nanotesla.

5.3 Firmware Architecture

VPM delivers two data products – a low-resolution survey mode, which runs constantly, and a commandable burst mode, which will accumulate an equivalent of 30 seconds of full-resolution data. All data processing is performed on a single Actel ProAsic3 FPGA, using fixed-point, twos-compliment arithmetic. Survey and burst mode streams operate in parallel, feeding data to a common memory controller, which packetizes and buffers data using a radiation-tolerant 128MB SDRAM. Fixed-size packets are then transmitted at the soonest availability to the host spacecraft at 400 kilobaud using a standard RS422 / UART protocol.

Figure 5.9 shows a block diagram of the firmware architecture.

5.3.1 Reduced-Resolution (Survey) Data

Survey data consists of a reduced-resolution energy spectrogram for each VLF channel, and if installed, an energy histogram of each particle detector. Survey-mode

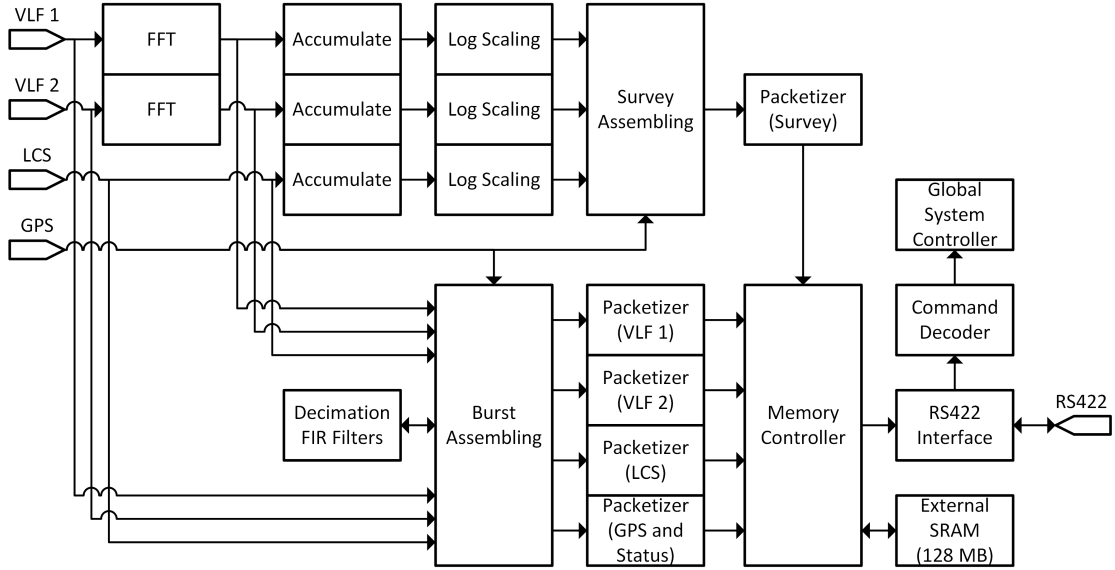


Figure 5.9: Block diagram of firmware modules. Arrows indicate flow of data.

time resolution can be selected from one of three presets – short, medium, and long – corresponding to 1024, 2048, or 4096 FFTs, or 6.5536, 13.1072, or 26.2144 seconds respectively. VLF spectrograms consist of 512 frequency bins, with energies mapped to 8 bits on a logarithmic scale.

Frequency Mapping and Accumulation

VLF data is delivered to the DPU as 16-bit, twos-compliment integers, which are buffered locally, overlapped by 50% (512 samples), and multiplied by a Chebyshev window function. Data is then mapped to the frequency domain using a 1024-point, decimation-in-time Fast Fourier Transform, as described in (*Oppenheim and Schafer, 2009*). Buffering within the FFT is sized such that the full resolution of multiplications are kept without overflow. Real and imaginary components are rounded to 16 bits.

Absolute values of the real and imaginary components are then squared and summed, resulting in a 512-point vector of 32-bit integers, representing the squared magnitude of the frequency content.

Magnitudes are then accumulated using the full input resolution plus 12 padding

bits, guaranteeing no overflow for $2^{12} = 4096$ accumulations. The resultant output is a 512-point vector of 44-bit integers.

Fixed-Point Log Scaling

Arithmetic beyond addition, subtraction, multiplication, and power-of-two division is intractable without a dedicated arithmetic unit, generally requiring an iterative or multi-cycle algorithm. In many cases a simple lookup table can be used to map values from one space to another; however the size of a stored lookup table can become unwieldy with increased resolution. VPM makes use of a hybrid algebraic / lookup table method to map 44-bit integers to an 8-bit logarithmic space in a single clock cycle, and making efficient use of FPGA resources.

We begin with the log-of-sums identity:

$$\log_n(a + b) = \log_n(a) + \log_n\left(1 + \frac{b}{a}\right) \quad (5.1)$$

where we separate our input into the *integer* portion, a , and the *fractional* portion, b . We take the integer portion to be the maximum power of two less than the input, and the fractional portion to be the remainder, $b = x - a$. Each component can then be dealt with separately via a reduced lookup table.

The integer portion is simple to compute: $\log_2(2^n) = n$, which can be calculated by finding the index of the greatest nonzero bit. To make full use of 8 output bits, we multiply by a scaling factor given by:

$$S = \frac{2^{Nb_{out}}}{Nb_{in}} \quad (5.2)$$

Where $Nb_{out} = 8$, the number of bits at the output, and $W_{in} = 32$, the number of bits at the input, for a scaling factor of $S = 8$.

The fractional portion, $\log_2\left(1 + \frac{b}{a}\right)$ is determined using a lookup table with $2^{Nb_{frac}}$ entries.

This method makes most-efficient use of the output range when both input and output bit widths are powers of two – e.g., mapping 32-bit input to 8-bit output.

Using $Nb_{in} = 32$, $Nb_{out} = 8$, and $Nb_{frac} = 5$, we require only two 32-entry lookup tables, rather than an intractable 2^{32} entries for a direct lookup table, or 256 entries for a partitioning lookup table.

VPM's accumulators deliver 44-bit integers, which must be passed into the 32-bit lookup tables. However, by simply taking the 32 most-significant bits, we introduce substantial error in the smaller output values. In order to make full use of the 44-bit integers, we use a barrel-shifting technique using the log-of-products identity:

$$\log(ab) = \log(a) + \log(b) \quad (5.3)$$

$$\log\left(\frac{a}{b}\right) = \log(a) - \log(b) \quad (5.4)$$

In the event that simply taking the most-significant 32 bits will result in a truncated fractional portion, we shift the input by Nb_{frac} bits; equivalent to multiplying by $2^{Nb_{frac}}$. We then pass the top 32 bits to the lookup tables, sum the result, and subtract the added portion $S \cdot Nb_{frac}$. The complete module is shown in figure 5.10, and performs within ± 1 bit from the equivalent floating-point computation in Matlab when x is greater than $2^{12} = 4096$.

For each frequency, the equivalent survey-mode computation is given by:

$$\text{round}(S \cdot \log_2\left(\frac{1}{n} \sum_1^n (\text{re}(x_f)^2 + \text{im}(x_f)^2)\right)) \quad (5.5)$$

where x_f are the outputs of the windowed, overlapped FFT.

Survey Product Data Structure

Each column of the survey product includes a complete GPS timestamp containing time, location, and velocity. GPS timestamps are collected every second; however no provisions are made to snap columns to the exact start time. Rather, survey columns are transmitted every 1024, 2048, or 4096 FFTs, depending on current configuration, with the GPS timestamp corresponding to the last whole second before the column is requested. In order to eliminate storage requirements for staging a survey column, data from the VLF receiver channels are interleaved, along with data from the particle

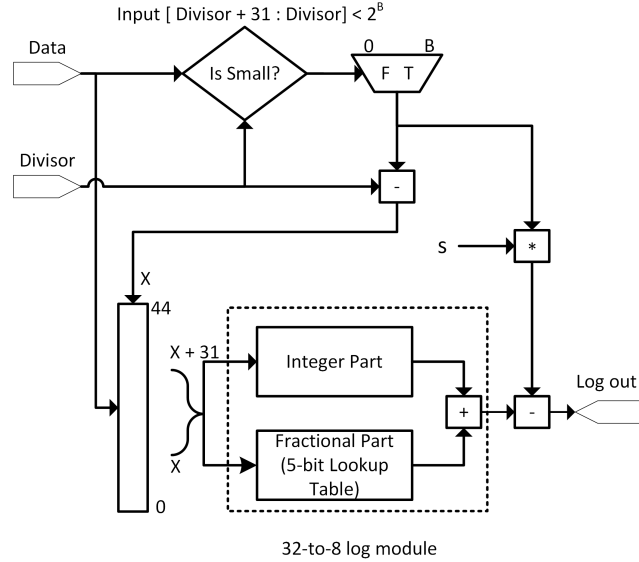


Figure 5.10: Block diagram of the log-scaling module, which efficiently maps a 32-bit average to an 8-bit value. Additional logic improves accuracy by making use of truncated bits for small inputs.

spectrometers if present, into a 4-byte output stream.

Each column begins with a 4-byte header, 0xABCD-1234. Survey data is then presented four bytes at a time, alternating between the two VLF channels and spectrometer data when available. The data stream alternates between the two VLF channels when the spectrometer data has been fully read out. When available, the survey data is followed by a 180-byte GPS timestamp. Each survey column ends with a four-byte footer, 0x6789-1234, and an appropriate number of zeroes to assure a complete 32-bit word is passed to the memory controller. When both GPS and spectrometer data are present, the resulting column is 1280 bytes. The data format is illustrated in figure 5.11.

5.3.2 Full-Resolution Burst Data

VPM can log full-resolution data in a variety of modes, here referred to as *experiments*. Data can be logged in either time or frequency domain, and can be taken on a

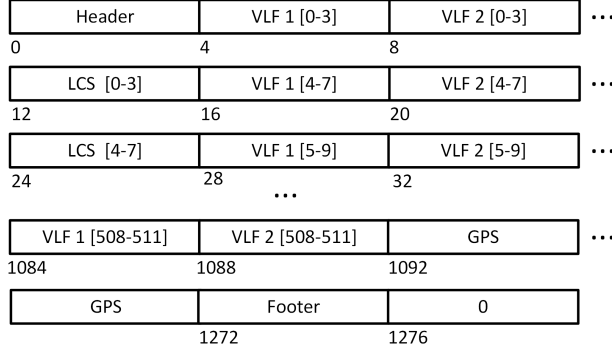


Figure 5.11: Interleaving scheme for survey data. A single survey column consists of 512 bytes from each of the two VLF channels, 64 bytes from the spectrometer, and 180 bytes from the GPS receiver. The data are interleaved in four-byte segments.

modulated duty cycle, ranging from a single 30-second segment, to a selectable 1, 2, 5, or 10 seconds of data followed by a 2, 5, 10, or 30 second pause. The requested modulation will be repeated n pulses times, which can be assigned via a separate command. When a GPS timestamp is available, an experiment will start at the next whole second after the burst command is received; if GPS card is not available, logging will start as soon as the command is received. Each subsequent on / off segment is tagged with a new GPS timestamp. A system status packet is logged at the beginning and end of each experiment.

Time-domain experiments can be taken at their full 80 kHz sampling rate, or decimated by factors 2, 4, 8, or 16. When decimation is selected, data is filtered using a 105th-order FIR low-pass filter. Filter coefficients were designed using the MATLAB Filter Design Toolbox (*fdatool*), using the Least-Squares design algorithm. Cutoff frequencies were selected such that signals above the Nyquist frequency are attenuated by at least 60 dB. Filter coefficients are hard-coded and stored in on-chip ROM; filter delay lines are stored in on-chip RAM. Multiply-accumulate processing is done serially using a single hardware multiplier per channel.

Maximum possible filter lengths are constrained both by available system resources, and by data sampling rate – that is for each new data sample, we require n multiplications. Given VPM’s 10 MHz system clock and 80 kHz sample rate, a

Table 5.1: Burst-mode duty-cycle modulation settings. Modes are listed as seconds on / seconds off.

0	10/30	4	5/30	8	2/30	12	1/30
1	10/10	5	5/10	9	2/10	13	1/10
2	10/5	6	5/5	10	2/5	14	1/5
3	10/2	7	5/2	11	2/2	15	1/2

maximum filter is $\approx \frac{10e6}{80e3} = 125$. $n = 105$ was chosen to give sufficient padding for possible clock drift.

Frequency-domain experiments can be used to effectively reduce storage and transmission requirements in the event that only a small frequency band is of interest. The frequency range – 512 bins, spaced uniformly between 0 and 40 kHz – is split into 16 bands, which can be selectively enabled with each experiment. VPM uses two parallel FFT engines, which implement a 1024-point FFT, using a 50% overlap and a Chebyshev window function with 75 dB sidelobe attenuation. Frequency data is accurate to a MATLAB or similar floating-point FFT computation to within 16 bits.

Burst experiments are selected using a 24-bit command structure as shown in figure 5.12. Each burst command begins with a header 2'b01. Bit three selects time-domain (1) or frequency-domain (0) data collection. Bit four enables time-axis duty-cycle modulation (“windowing”); bits 5 through 8 select the windowing pattern as shown in table 5.1. For time-domain experiments, bit 9 enables downsampling and decimation. The downsampling factor is set by bits 10 and 11 – 2'b00, 2'b01, 2'b10, and 2'b11 corresponding to 40 kHz, 20 kHz, 10 kHz and 5 kHz sampling rates respectively. For time-domain experiments, the remaining 13 bits are ignored. For frequency-domain experiments, bits 9 through 24 enable storage of each frequency band, from highest-frequency to lowest-frequency. Each band contains 32 FFT bins for a bandwidth of 2500 Hz.

5.3.3 GPS Timestamps

VPM uses a NovAtel OEM 615 embedded GPS receiver which communicates directly with the DPU via RS232. When the system is reset, or when GPS synchronization is

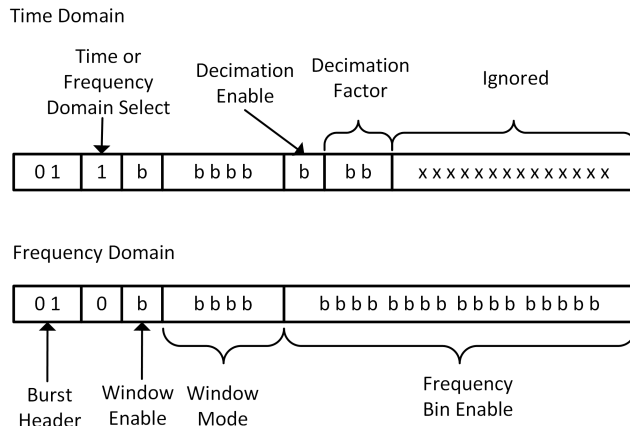


Figure 5.12: 24-bit command structure used to request burst experiments. The top row shows a time-domain experiment; the bottom shows a frequency domain experiment.

selected, the DPU requests two data products – BESTPOSB and BESTVALB – which provide solutions for position and velocity, encoded in a binary stream as described in (nov, 2012). Timestamps are updated every second, and are accurate to the system sampling clock / PPS to ± 50 ns. Together, the two data products occupy 180 bytes, and include position, velocity, and several metrics of quality-of-fit. Decoding can be done using the NovAtel Convert4 application, or our provided MATLAB script.

Figure 5.13 shows an example of a frequency-domain experiment, which has been windowed on both the time and frequency axes, and its corresponding survey data.

5.3.4 System Status Messages

VPM includes provisions for a single, comprehensive system status message. A system status message is logged at the beginning and end of each burst experiment; at the beginning of an antenna arm or deploy command; if the GPS receiver times out; or upon request by the host spacecraft.

Status messages include the following information:

- Source of the status request

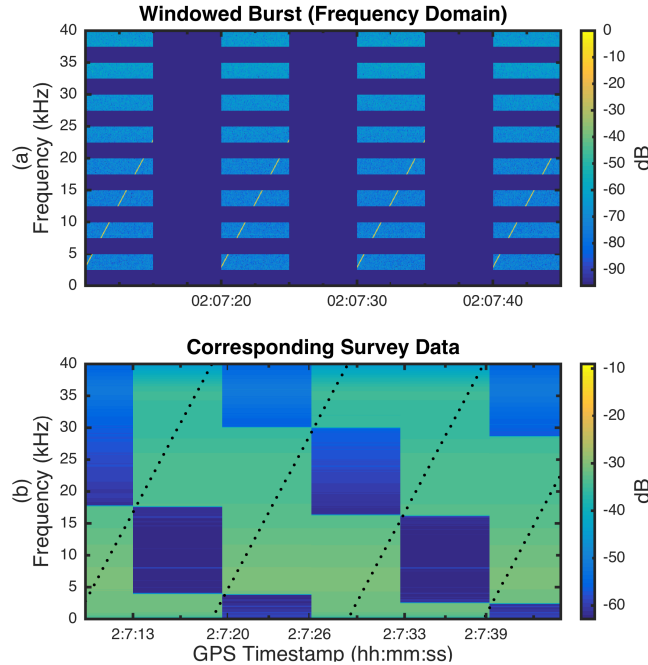


Figure 5.13: An example of a burst experiment. Plot (a) shows the data returned from a frequency-domain burst experiment, which has been windowed in time using mode 6 – five seconds on, five seconds off. Only every other frequency bin has been enabled. Input to the μ BBR is a 10-second frequency sweep. Plot (b) shows the corresponding survey data, using the highest-resolution setting (\approx 6.5-second bins). The dashed black overlay shows the approximate input frequency. Amplitudes are shown in decibels relative to full-scale.

- Last command received by the system
- System uptime in seconds
- Total commands received by the system
- Channel enabled / disabled status of E, B, and LCS burst data
- Sampling clock selection - either GPS or internal
- Deployer arm status for each antenna
- Total attempted antenna deploys since last reset

- Analog housekeeping mux setting
- Survey product duration
- Current burst repeat setting
- Total packets sent from each data stream
- Total bytes currently stored in memory
- Current experiment number for each data stream
- Total count of GPS errors and attempted resets

5.3.5 Memory and Data Storage

VPM lacks a full-fledged CPU and operating system, which necessitates the creation of a simple data handling and arbitration scheme. Use of a file system is avoided by regarding pre-transmission memory as a single buffering queue, with the expectation that data is read by the host spacecraft at the soonest availability. Memory management is divided into a set of packetizing modules – one for each unique datastream – which feed a simple arbitrating state machine. Complete packets are then stored contiguously in the external 128 MB SDRAM in the order in which they are generated. Packets are read contiguously, first-in-first-out.

Packeting

VPM has facilities for six unique datastreams: Survey data; two channels of VLF data; spectrometer (LCS) data; GPS timestamps; and system status messages. Each datastream feeds an identical parallel packeting module, which writes packet headers and footers, logs metadata required in decoding, escapes header bytes from within the datastream, and inserts padding zeros to guarantee a consistent 512-byte packet. Packeting modules can each buffer two full packets before being read out.

Header and footer bytes are both 0x7E; however bytes in the datastream can take on all possible values between 0x00 and 0xFF. To prevent confusion when reading

packets, we escape all instances of 0x7E within the datastream and insert a two-byte sequence 0x7D7D. Additionally, instances of 0x7D are replaced with 0x7D5D. To guarantee realtime streaming, escaping and external SDRAM reads and writes operate on a full-speed 20 MHz clock.

VPM’s packet structure is shown in figure 5.14. The following metadata are included in each packet:

- Packet Start Index (4 bytes): A four-byte integer representing the sample index of the first value within the packet – used in assembling many thousands of packets from a burst experiment into a contiguous field.
- Data Type (1 byte): Each channel is tagged with a single-byte label, denoting the packet’s source: ASCII “S” for Survey; “E” for VLF 1; “B” for VLF 2; “L” for spectrometer data; “G” for GPS data; and “I” for system information / status messages.
- Experiment Number (1 byte): Each experiment or survey column share a common experiment number, used to distinguish packets from sequential experiments.
- Checksum (1 byte): A simple checksum is provided as a quick verification of packet health. VPM’s checksum is a simple, 1-byte rolling sum of all prior bytes in the packet, including headers and escape characters. Two bytes are reserved in the packet order so that, in the event that the checksum value is escaped, the packet will remain a fixed size.
- Byte Count (2 bytes): An integer representing the number of bytes contained within the packet, post-escaping. In order to maintain a fixed-size packet, data fields are padded with a variable number of zeroes. Three bytes are reserved for Byte Count in the event that the value is escaped. Note that only one value need be reserved, as the most-significant byte will never be escaped.

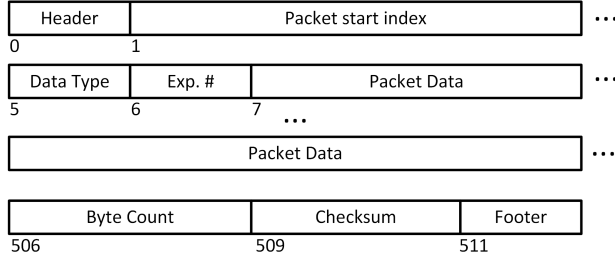


Figure 5.14: Structure of packets returned by VPM. Packets include various metadata required for reassembly, and are zero-padded to assure a constant size of 512 bytes.

5.3.6 System Control

Commands are passed to VPM through the RS422 port, which operates at 400 kilobaud. Commands are received by a simple format-checking state machine. All commands are 24-bit, and of the form: $\{ \text{0x7E} \parallel \text{Byte 1} \parallel \text{Byte 2} \parallel \text{Byte 3} \parallel \text{0x7E} \}$. Bytes are reassembled in big-endian order. Commands which do not meet this form exactly are discarded; however, the three command bytes must be escaped in the same manner as on transmission if they include a 0x7E or 0x7D value.

Successfully-received commands are passed to a master state machine, which then sets global parameters and passes commands to submodules accordingly.

The first two bits of a command dictate the intended recipient: 2b'00 for DPU and system commands; 2b'01 for burst commands; 2b'10 for μ BBR commands; and 2b'11 for commands sent to the loss-cone spectrometer.

DPU commands are in a human-readable ASCII character format (“G1” = Enable GPS, “G0” = Disable GPS, etc). Burst and μ BBR commands assign a specific purpose to each of the remaining 22 bits.

5.4 Concluding Remarks

We have described a novel design for a CubeSat payload instrument, which is capable of sampling the VLF band of the electromagnetic spectrum while simultaneously sampling energetic particle distributions of the radiation belt. The system draws

less than 5 Watts including the onboard GPS receiver, and occupies a 1.5U volume. The system provides two data products – a low-resolution survey product which runs continuously, and a full-resolution burst product, which is available on demand from the host spacecraft. The onboard software is implemented entirely in an FPGA fabric, eliminating the need for additional volatile program storage, which reduces risk of CPU errors and improves system reliability. Additionally the system can be implemented using radiation-tolerant components. A CubeSat carrying the VPM payload is scheduled to be launched by the Air Force Research Laboratory in 2019.

Chapter 6

Conclusions

6.1 Suggestions for Future Work

Appendix A

Reference Equations

A.1 Landau Damping

In raytracing, we calculate wave growth and attenuation according to Landau damping. We use the *Brinca* (1972) formulation – itself a reorganization of *Kennel* (1966) – which assumes a cold background plasma, onto which a small thermal electron population is ascribed. The following (frustratingly complex) equation set is taken from *Brinca* (1972), and reprinted here for organization.

Calculating a growth rate begins simply: we assume a time-varying plane wave in the usual complex (“phasor”) form:

$$E \sim E_0 e^{i(\omega t - \mathbf{k} \cdot \mathbf{r})} \quad (\text{A.1})$$

If either ω or \mathbf{k} have an imaginary component, then the result will be an additional real-valued term, which we can factor out as χ :

$$E = E_0 e^{i(\omega t - (\mathbf{k}_r + i\mathbf{k}_i) \cdot \mathbf{r})} \quad (\text{A.2})$$

$$= E_0 e^{-\chi r} e^{i(\omega t + \mathbf{k} \cdot \mathbf{r})} \quad (\text{A.3})$$

If the new exponential term $-\chi$ is positive, the wave will be amplified; if the term is negative, the wave will be attenuated.

The spatial growth rate χ is given by equation A.4 (*Brinca*, 1972; *Kennel*, 1966):

$$\chi = -\frac{ck_i}{\omega} = \frac{\delta}{4\eta(2A\eta^2 - B)} (T_1 - T_2 - T_3) \quad (\text{A.4})$$

with the following terms:

$$\begin{aligned} T_1 &= \frac{\eta^2 \sin \theta^2 - P}{2(S - \eta^2)} \Gamma_I \cdot [(R - \eta^2) J_{m-1} + (L - \eta^2) J_{m+1}]^2 G_1 \\ T_2 &= 2[(S - \eta^2 \cos^2 \theta)(S - \eta^2) - D^2] \Lambda_I J_m G_2 \\ T_3 &= 2\eta^2 \sin \theta \cos \theta \Gamma_I \cdot [(R - \eta^2) J_{m-1} + (L - \eta^2) J_{m+1}] G_2 \end{aligned} \quad (\text{A.5})$$

where $\chi > 0$ indicates damping.

Note that *Brinca* has related the temporal damping rate ω_i from *Kennel* (1966) to a spatial damping rate k_i by assuming a constant propagation at the group velocity v_g .

A, B, C, D, L, P, R , and S are the Stix environment parameters given by 2.26 – 2.27, and are functions of wave frequency, local plasma density, and local magnetic field strength.

As previous, θ is the angle between the wavenormal vector and the background magnetic field, and η is the wave refractive index, found by solving equation 2.30.

The terms J_m , J_{m+1} and J_{m-1} are Bessel functions of the first kind, which account for the multiple resonant modes – $m = 0$ indicates the Landau resonance; $m \pm 1$ the Cyclotron resonance.

The terms Γ_I and Λ_I are summations over resonant modes $m \in \{-\infty \dots \infty\}$, and integrations over the velocity space v_\perp, v_\parallel given by:

$$\Gamma_I = \frac{2\pi^2\omega_p^2}{\omega k_{\parallel}} \sum_{m=-\infty}^{\infty} \int_0^{\infty} v_{\perp}^2 dv_{\perp} \int_{-\infty}^{\infty} \delta(v_{\parallel} - V_m) dv_{\parallel} \quad (\text{A.6})$$

$$\Lambda_I = \frac{2\pi^2\omega_p^2}{\omega k_{\parallel}} \sum_{m=-\infty}^{\infty} \int_0^{\infty} v_{\perp} dv_{\perp} \int_{-\infty}^{\infty} v_{\parallel} \delta(v_{\parallel} - V_m) dv_{\parallel} \quad (\text{A.7})$$

$$V_m = \frac{\omega - m\omega_c}{k_{\parallel}} \quad (\text{A.8})$$

Finally, the temperature distribution is included in the values G_1 and G_2 – each of which are functions of the *gradient* of the phase-space distribution function:

$$f = f(\mathbf{x}, \mathbf{v}) = f(\mathbf{x}, v_{\perp}, v_{\parallel}):$$

$$G_1 = \left(1 - \frac{k_{\parallel}v_{\perp}}{\omega}\right) \frac{\partial f}{\partial v_{\perp}} + \frac{k_{\parallel}v_{\perp}}{\omega} \frac{\partial f}{\partial v_{\parallel}} \quad (\text{A.9})$$

$$G_2 = J_m \left[\left(1 + \frac{m\omega_c}{\omega}\right) \frac{\partial f}{\partial v_{\parallel}} - m \frac{\omega_c}{\omega v_{\perp}} \frac{\partial f}{\partial v_{\perp}} \right] \quad (\text{A.10})$$

Despite the complexity of these equations, the phase-space distribution function f is the only fundamental new input – every remaining parameter is an output of the raytracer, and itself a result of our plasma density and magnetic field models.

Our implementation, derived from *Golden et al.* (2010), computes the gradients of f numerically using finite differencing, therefore granting the flexibility to use any arbitrary distribution function.

Bibliography

(2012), OEM6 TM Family Firmware Reference Manual, *Tech. Rep. July*, NovAtel Inc.

Angerami, J. J. (1963), Studies of Planetary Atmospheres 1., *Distribution*, 69(21).

Appleton, E. V. (1932), Appleton : Wireless Studies of the Ionosphere . Wireless Studies of the Ionosphere .* Appleton : Wireless Studies of the Ionosphere ., (10).

Baker, D. N., A. N. Jaynes, V. C. Hoxie, R. M. Thorne, J. C. Foster, X. Li, J. F. Fennell, J. R. Wygant, S. G. Kanekal, P. J. Erickson, W. Kurth, W. Li, Q. Ma, Q. Schiller, L. Blum, D. M. Malaspina, A. Gerrard, and L. J. Lanzerotti (2014), An impenetrable barrier to ultrarelativistic electrons in the Van Allen radiation belts, *Nature*, 515(7528), 531–534, doi:10.1038/nature13956.

Baker, K. B., and S. Wing (1989), A new magnetic coordinate system for conjugate studies at high latitudes, *Journal of Geophysical Research*, 94(A7), 9139, doi: 10.1029/JA094iA07p09139.

Balmain, K. G. (1964), The Impedance of a Short Dipole Antenna in a Magnetoplasma, *IEEE Transactions on Antennas and Propagation*, AP-12(5), 605–617, doi:10.1109/TAP.1964.1138278.

Barber, C. B., D. P. Dobkin, and H. Huhdanpaa (1996), The quickhull algorithm for convex hulls, *ACM Transactions on Mathematical Software*, 22(4), 469–483, doi:10.1145/235815.235821.

- Barth, J. L., C. S. Dyer, and E. G. Stassinopoulos (2003), Space, atmospheric, and terrestrial radiation environments, *IEEE Transactions on Nuclear Science*, 50 III(3), 466–482, doi:10.1109/TNS.2003.813131.
- Beall, D. S., C. O. Bostrom, and D. J. Williams (1967), Structure and Decay of the Starfish Radiation Belt, October 1963 to December 1965, *Journal of Geophysical Research*, 72(13), 3403, doi:10.1029/JZ072i013p03403.
- Bell, T. F. (1984), The nonlinear gyroresonance interaction between energetic electrons and coherent VLF waves propagating at an arbitrary angle with respect to the Earth's magnetic field, *Journal of Geophysical Research*, 89(A2), 905–918, doi: 10.1029/JA089iA02p00905.
- Bell, T. F. (2002), The Landau damping of magnetospherically reflected whistlers within the plasmasphere, *Geophysical Research Letters*, 29(15), 2–5, doi: 10.1029/2002GL014752.
- Bhattacharya, S., S. Sarkar, A. K. Gwal, and M. Parrot (2009), Electric and magnetic field perturbations recorded by DEMETER satellite before seismic events of the 17th July 2006 M 7.7 earthquake in Indonesia, *Journal of Asian Earth Sciences*, 34(5), 634–644, doi:10.1016/j.jseaes.2008.08.010.
- Bilitza, D., and B. W. Reinisch (2008), International Reference Ionosphere 2007: Improvements and new parameters, *Advances in Space Research*, 42(4), 599–609, doi:10.1016/j.asr.2007.07.048.
- Bittencourt, J. A. (2004), *Fundamentals of Plasma Physics*, 3rd ed.
- Blaes, P. R., R. A. Marshall, and U. S. Inan (2016), Global occurrence rate of elves and ionospheric heating due to cloud-to-ground lightning, *Journal of Geophysical Research A: Space Physics*, 121(1), 699–712, doi:10.1002/2015JA021916.
- Bortnik, J. (2005), Precipitation of radiation belt electrons by lightning-generated magnetospherically reflecting whistlers, Ph.D. thesis, Stanford University.

- Bortnik, J., and R. M. Thorne (2007), The dual role of ELF/VLF chorus waves in the acceleration and precipitation of radiation belt electrons, *Journal of Atmospheric and Solar-Terrestrial Physics*, 69(3), 378–386, doi:10.1016/j.jastp.2006.05.030.
- Bortnik, J., U. S. Inan, and T. F. Bell (2006), Temporal signatures of radiation belt electron precipitation induced by lightning-generated MR whistler waves: 1. Methodology, *Journal of Geophysical Research: Space Physics*, 111(2), 1–22, doi: 10.1029/2005JA011182.
- Bortnik, J., R. M. Thorne, and N. P. Meredith (2007), Modeling the propagation characteristics of chorus using CRRES suprathermal electron fluxes, *Journal of Geophysical Research: Space Physics*, 112(8), 1–13, doi:10.1029/2006JA012237.
- Bothmer, V., and I. A. Daglis (2007), *Space Weather: Physics and Effects*, Springer Science and Business Media.
- B.Peter, W. (2007), Quantitative Measurement of Lightning-Induced Electron Precipitation Using Vlf Remote Sensing, (February).
- Brinca, A. L. (1972), On the Stability of Obliquely Propagating Whistlers, *Journal of Geophysical Research*, 77(19), 3495–3507.
- Brooks, C. E. P. (1925), The distribution of thunderstorms over the globe, *Geophysical Memorandum*, 24.
- Bruce, C. E. R., and R. H. Golde (1941), The Lightning Discharge, *The Journal of the I.E.E.E*, 88(6), 487–505.
- Burgess, W. C., and U. S. Inan (1993), The Role of Ducted Whistlers in the Precipitation Loss and Equilibrium Flux of Radiation Belt Electrons, *Journal of Geophysical Research*, 98(A9), 15,643–15,665.
- Carpenter, D. L., and R. R. Anderson (1992), An ISEE / Whistler Model of Equatorial Electron Density in the Magneto sphere Od D ’ j :, *J. Geophys. Res.*, 97, 1097–1108.

- Carpenter, D. L., U. S. Inan, M. L. Trimpi, R. A. Helliwell, and J. P. Katsufakis (1984), Perturbations of subionospheric LF and MF signals due to whistler-induced electron precipitation bursts, doi:10.1029/JA089iA11p09857.
- Cattell, C. A., A. W. Breneman, S. A. Thaller, J. R. Wygant, and C. A. Kletzing (2015), Van Allen Probes observations of unusually low frequency whistler mode waves observed in association with moderate magnetic storms: Statistical study, *Geophysical Research Letters*, 42(18), 7273–7281, doi:10.1002/2015GL065565.
- Cayton, T. E. (2005), Phase-Space Density Analyses of the AE-8 Trapped Electron and the AP-8 Trapped Proton Model Environments, *Tech. rep.*, Office of Scientific and Technical Information, Oak Ridge, TN, Los Alamos, NM.
- Chandler, O., M. O. Chandler, J. H. Waite, and T. E. Moore (1991), Observations of polar ion outflows, *Journal of Geophysical Research: Space Physics*, 96(A2), 1421–1428, doi:10.1029/90JA02180.
- Chang, H. C., and U. S. Inan (1983), Quasi-relativistic electron precipitation due to interactions with coherent VLF waves in the magnetosphere, *Journal of Geophysical Research*, 88(A1), 318–328.
- Chang, H. C., and U. S. Inan (1985), Test particle modeling of wave-induced energetic electron precipitation, doi:10.1029/JA090iA07p06409.
- Chen, F. F. (1983), *Introduction to Plasma Physics and Controlled Fusion*, Plenum Press, New York, NY, doi:QC718.C39 1983.
- Chevalier, T. W. (2007), Near-Field Characteristics of Electric Dipole Antennas in The Inner Magnetosphere, Ph.D. thesis, Stanford University.
- Cohen, M. B., N. G. Lehtinen, and U. S. Inan (2012), Models of ionospheric VLF absorption of powerful ground based transmitters, *Geophysical Research Letters*, 39(24), 1–5, doi:10.1029/2012GL054437.

- Conrad, E., G. Gurtman, G. Kweder, M. J. Mandell, and W. W. White (2010), Collateral Damage to Satellites from an EMP Attack, *DTRA Technical Report, DTRA-IR-10*.
- Cornwall, J. M. (1964), Scattering of energetic trapped electrons by very-low-frequency waves, *Journal of Geophysical Research*, 69(7), 1251–1258, doi: 10.1029/JZ069i007p01251.
- Cotts, B. R. T. (2011), Global Quantification of Lightning-Induced Electron Precipitation Using Very Low Frequency Remote Sensing, Ph.D. thesis.
- Cussac, T., M. A. Clair, P. Ultré-Guerard, F. Buisson, G. Lassalle-Balier, M. Ledu, C. Elisabelar, X. Passot, and N. Rey (2006), The Demeter microsatellite and ground segment, *Planetary and Space Science*, 54(5), 413–427, doi: 10.1016/j.pss.2005.10.013.
- Delaunay, B. (1934), Sur la sphere vide, doi:10.1051/jphysrad:01951001207073500.
- Dungey, J. (1963), Loss of van allen electrons due to whistlers, *Planetary and Space Science*, 11(6), 591–595, doi:10.1016/0032-0633(63)90166-1.
- Edgar, B. (1972), The structure of the magnetosphere as deduced from magneto-spherically reflected whistlers, Ph.D. thesis, Stanford University.
- English, R. A., R. E. Benson, V. J. Bailey, and C. M. Barnes (1973), Apollo Experience Report- Protection Against Radiation.
- Fehlberg, E. (1969), Low-order classical Runge-Kutta formulas with stepsize control and their application to some heat transfer problems, *Tech. Rep. July*, NASA.
- Gallagher, D. L., P. D. Craven, R. H. Comfort, and T. E. Moore (1995), On the azimuthal variation of core plasma in the equatorial magnetosphere, *Journal of Geophysical Research: Space Physics*, 100(A12), 23,597–23,605, doi: 10.1029/95JA02100.

- Gallagher, D. L., P. D. Craven, and R. H. Comfort (1999), Global Core Plasma Model, *Journal of Geophysical Research: Space Physics*, 105(A8), 18,819–18,833, doi:10.1029/1999JA000241.
- Gemelos, E. S., U. S. Inan, M. Walt, M. Parrot, and J. A. Sauvaud (2009), Seasonal dependence of energetic electron precipitation: Evidence for a global role of lightning, *Geophysical Research Letters*, 36(21), 0–4, doi:10.1029/2009GL040396.
- Golden, D. I., M. Spasojevic, F. R. Foust, N. G. Lehtinen, N. P. Meredith, and U. S. Inan (2010), Role of the plasmapause in dictating the ground accessibility of ELF/VLF chorus, *Journal of Geophysical Research: Space Physics*, 115(11), 1–15, doi:10.1029/2010JA015955.
- Graf, K. (2009), The Effects of Ground-Based Very Low Frequency Transmitters on the Ionosphere and Magnetosphere, Ph.D. thesis, Stanford University.
- Griffiths, D. J. (1999), *Introduction to Electrodynamics*, 3rd ed., Prentice-Hall, Inc, Upper Saddle River, New Jersey.
- Hakura, Y. (1965), Tables and maps of geomagnetic coordinates corrected by the higher spherical harmonic terms, *Rep. Ionos. Space Res. Japan*, 19, 121–157.
- Haselgrove, J. (1954), Ray theory and a new method for ray tracing, *Report of the Physical Society Conference on Physics of the Ionosphere*, pp. 355–364.
- Haselgrove, J., and C. B. Haselgrove (1960), Twisted ray paths in the ionosphere, *Proceedings of the Physical Society*, 75, 357–363, doi:10.1088/0370-1301/70/7/302.
- Helliwell, R. A. (1965), *Whistlers and Related Ionospheric Phenomena*, Stanford University Press.
- Helliwell, R. A., J. P. Katsufakis, and M. L. Trimpi (1973), Whistler-induced amplitude perturbation in VLF propagation, doi:10.1029/JA078i022p04679.
- Henyey, F. S. (1980), Improved ray description of wave equations, *Physical Review Letters*, 45(24), 1897–1900, doi:10.1103/PhysRevLett.45.1897.

- Hess, W. N. (1963), The artificial radiation belt made on July 9, 1962, *Journal of Geophysical Research*, 68(3), 667–683, doi:10.1029/JZ068i003p00667.
- Hess, W. N. (1964), The Effects of High Altitude Explosions, *Tech. rep.*, Goddard Space Flight Center, National Aeronautics and Space Administration.
- Hoerlin, H. (1976), United States High-Altitude Test Experiments: A Review Emphasizing the Impact on the Environment, *Los Alamos, Scientific Laboratory of the University of California, LA-6405*, 23–27.
- Horner, F. (1954), The accuracy of the location of sources of atmospherics by radio direction-finding, *Proceedings of the IEE - Part III: Radio and Communication Engineering*, 101(74), 383–390, doi:10.1049/pi-3.1954.0091.
- Horner, F. (1957), Very-Low-Frequency Propagation and Direction-Finding, *The Proceedings of the Institution of Electrical Engineers*, 104(14), 73–80.
- Inan, U., W. Burgess, T. Wolf, D. Shafer, and R. Orville (1988), Lightning-Associated Precipitation of MeV Electrons from the Inner Radiation Belt, *Geophysical Research Letters*, 15(2), 172–175, doi:10.1029/GL015i002p00172.
- Inan, U. S. (1977), Non-Linear Gyroresonant Interactions of Energetic Particles and Coherent VLF Waves in the Magnetosphere, Ph.D. thesis, Stanford University.
- Inan, U. S., M. Walt, H. D. Voss, and W. L. Imhof (1989), Energy spectra and pitch angle distributions of lightning-induced electron precipitation - Analysis of an event observed on the S81-1 (SEEP) satellite, *Journal of Geophysical Research (ISSN 0148-0227)*, 94, 1379, doi:10.1029/JA094iA02p01379.
- Kennel, C. (1966), Low-Frequency Whistler Mode, *Physics of Fluids*, 9(11), 2190, doi:10.1063/1.1761588.
- Kennel, C. F., and H. E. Petschek (1966), Limit on stably trapped particle fluxes., *Journal of Geophysical Research*, 71(1), 1–28, doi:10.1029/JZ071i001p00001.

- Kimura, I. (1966), Effects of Ions on Whistler-Mode Ray Tracing, *Radio Science*, 1(3), 269–283, doi:10.1002/rds196613269.
- Krider, E. P., R. C. Noggle, A. E. Pifer, and D. L. Vance (1980), Lightning Direction-Finding Systems for Forest Fire Detection, doi:10.1175/1520-0477(1980)061;0980:LDFSFF;2.0.CO;2.
- Kulkarni, P. (2009), Controlled precipitation of radiation belt electrons, Ph.D. thesis, Stanford University, doi:10.1029/2002JA009580.
- Landau, L. D. (1946), On the vibrations of the electronic plasma, *Soviet Journal of Physics*.
- Lauben, D. (1998), Precipitation of radiation belt Electrons by obliquely-propagating lightning-generated whistler waves, Ph.D. thesis, Stanford University.
- Lauben, D. S., U. S. Inan, and T. F. Bell (1999), Polewarddisplaced electron precipitation from lightninggenerated oblique whistlers, *Geophysical Research Letters*, 26(16), 2633, doi:10.1029/1999GL900374.
- Lauben, D. S., U. S. Inan, and T. F. Bell (2001), Precipitation of radiation belt electrons induced by obliquely propagating lightning-generated whistlers, *Journal of Geophysical Research*, 106(A12), 29,745, doi:10.1029/1999JA000155.
- Laundal, K. M., and A. D. Richmond (2016), Magnetic Coordinate Systems, *Space Science Reviews*, pp. 1–33, doi:10.1007/s11214-016-0275-y.
- Lee, D. T., and B. J. Schachter (1980), Two algorithms for constructing a Delaunay triangulation, *International Journal of Computer & Information Sciences*, 9(3), 219–242, doi:10.1007/BF00977785.
- Lyons, L. R., and R. M. Thorne (1973), Equilibrium structure of radiation belt electrons, *Journal of Geophysical Research*, 78(13), 2142–2149, doi:10.1029/JA078i013p02142.

- Marshall, R. A., J. Bortnik, N. Lehtinen, and S. Chakrabarti (2011), Optical signatures of lightning-induced electron precipitation, *Journal of Geophysical Research: Space Physics*, 116(8), 1–8, doi:10.1029/2011JA016728.
- Mathews, J. H., and K. D. Fink (2004), *Numerical Methods Using Matlab*.
- McIlwain, C. E. (1961), Coordinates for mapping the distribution of magnetically trapped particles, *Journal of Geophysical Research*, 66(11), 3681–3691, doi: 10.1029/JZ066i011p03681.
- Meredith, N. P., R. B. Horne, S. A. Glauert, and R. R. Anderson (2007), Slot region electron loss timescales due to plasmaspheric hiss and lightning-generated whistlers, *Journal of Geophysical Research: Space Physics*, 112(8), 1–12, doi: 10.1029/2007JA012413.
- Montgomery, M. D., J. R. Asbridge, S. J. Bame, and W. C. Feldman (1974), Solar wind electron temperature depressions following some interplanetary shock waves: evidence for magnetic merging?, *Journal of Geophysical Research*, 79(22), 3103–3110, doi:10.1029/JA079i022p03103.
- Mossawir, B. (2009), High-Fidelity, Broadband Amplification and Filtering for Spaceborne Instrumentation, Ph.D. thesis, Stanford University.
- Nag, A., S. Mallick, V. A. Rakov, J. S. Howard, C. J. Biagi, J. D. Hill, M. A. Uman, D. M. Jordan, K. J. Rambo, J. E. Jerauld, B. A. DeCarlo, K. L. Cummins, and J. A. Cramer (2011), Evaluation of U.S. national lightning detection network performance characteristics using rocket-triggered lightning data acquired in 2004-2009, *Journal of Geophysical Research Atmospheres*, 116(2), 1–8, doi: 10.1029/2010JD014929.
- Ngo, H. D. (1989), Electrostatic waves stimulated by VLF whistler mode waves scattering from magnetic-field-aligned plasma density irregularities, Ph.D. thesis, Stanford University.

- Norris, R. S., and T. B. Cochran (1996), Nuclear Weapons Tests and Peaceful Nuclear Explosions by the Soviet Union: August 29, 1949 to October 24, 1990.
- Oppenheim, A. V., and R. W. Schafer (2009), *Discrete-Time Signal Processing*, 3rd ed., Prentice Hall Press, Upper Saddle River, New Jersey.
- Orville, R. E. (1995), Lighting Detection from Ground and Space, in *Handbook of Atmospheric Electrodynamics*, pp. 137–149.
- Orville, R. E., and D. W. Spencer (1979), Global Lightning Flash Frequency, doi: 10.1175/1520-0493(1979)107;0934:GLFF;2.0.CO;2.
- Paschal, E. (2005), Pseudo-Random Waveforms and Comb Calibration Signals, *Tech. rep.*, Stanford University.
- Persoon, A. M., D. A. Gurnett, and S. D. Shawhan (1983), Polar cap electron densities from DE 1 plasma wave observations, *Journal of Geophysical Research: Space Physics*, 88(A12), 10,123–10,136, doi:10.1029/JA088iA12p10123.
- RistićDjurović, J. L. (1993), Gyroresonant Scattering of Radiation Belt Electrons by Oblique Whistler Waves, Ph.D. thesis, Stanford University.
- RistićDjurović, J. L., U. S. Inan, and T. F. Bell (1992), Precipitation of Suprathermal (100 EV) Electrons by Oblique Whistler Waves, *Geophysical Research Letters*, 19(16), 1639–1642.
- RistićDjurović, J. L., T. F. Bell, and U. S. Inan (1998), Precipitation of radiation belt electrons by magnetospherically reflected whistlers, *Journal of Geophysical Research*, 103(A5), 9249–9260.
- Said, R. K., U. S. Inan, and K. L. Cummins (2010), Long-range lightning geolocation using a VLF radio atmospheric waveform bank, *Journal of Geophysical Research Atmospheres*, 115(23), 1–19, doi:10.1029/2010JD013863.
- Sazhin, S. (1993), *Whistler-mode Waves in a Hot Plasma*, 1 ed., Cambridge University Press, Cambridge.

- Schoenberg, J., D. Cohen, G. Ginet, B. Dichter, M. Xapsos, A. Adler, M. Scherbarth, and D. Smith (2006), The Demonstration and Science Experiments (DSX): A fundamental science research mission advancing technologies that enable MEO spaceflight, in *European Space Agency, (Special Publication) ESA SP*, vol. 625 SP.
- Schwelb, E. (1964), Nuclear Test Ban Treaty and International Law, *The American Journal of International Law*, 58(3), 642–670.
- Shepherd, S. G. (2014), Altitude-adjusted corrected geomagnetic coordinates: Definition and functional approximations, *Journal of Geophysical Research: Space Physics*, 119(9), 7501–7521, doi:10.1002/2014JA020264.
- Shprits, Y. Y., R. M. Thorne, R. B. Horne, S. A. Glauert, M. Cartwright, C. T. Russell, D. N. Baker, and S. G. Kanekal (2006), Acceleration mechanism responsible for the formation of the new radiation belt during the 2003 Halloween solar storm, *Geophysical Research Letters*, 33(5), 2–5, doi:10.1029/2005GL024256.
- Spangelo, S. C., M. W. Bennett, D. C. Meinzer, A. T. Klesh, J. A. Arlas, and J. W. Cutler (2013), Design and implementation of the GPS subsystem for the Radio Aurora eXplorer, *Acta Astronautica*, 87, 127–138, doi:10.1016/j.actaastro.2012.12.009.
- Spanjers, G., J. Winter, D. Cohen, A. Adler, J. Guarnieri, M. Tolliver, G. Ginet, B. Dichter, and J. Summers (2006), The AFRL Demonstration and Science Experiments (DSX) for DoD Space Capability in the MEO, *2006 IEEE Aerospace Conference*, pp. 1–10, doi:10.1109/AERO.2006.1655750.
- Spence, H. E., G. D. Reeves, D. N. Baker, J. B. Blake, M. Bolton, S. Bourdarie, A. A. Chan, S. G. Claudepierre, J. H. Clemons, J. P. Cravens, S. R. Elkington, J. F. Fennell, R. H. Friedel, H. O. Funsten, J. Goldstein, J. C. Green, A. Guthrie, M. G. Henderson, R. B. Horne, M. K. Hudson, J. M. Jahn, V. K. Jordanova, S. G. Kanekal, B. W. Klatt, B. A. Larsen, X. Li, E. A. MacDonald, I. R. Mann, J. Niehof, T. P. O'Brien, T. G. Onsager, D. Salvaggio, R. M. Skoug, S. S. Smith, L. L. Suther, M. F. Thomsen, and R. M. Thorne (2014), Science goals and overview of the Radiation Belt Storm Probes (RBSP) Energetic Particle, Composition, and

- Thermal Plasma (ECT) suite on NASA's Van Allen Probes mission, *The Van Allen Probes mission*, 9781489974334, 311–336, doi:10.1007/978-1-4899-7433-4-10.
- Starks, M. J., R. A. Quinn, G. P. Ginnet, J. M. Albert, G. S. Sales, B. W. Reinisch, and P. Song (2008), Illumination of the plasmasphere by terrestrial very low frequency transmitters: Model validation, *Journal of Geophysical Research: Space Physics*, 113(9), 1–16, doi:10.1029/2008JA013112.
- Stix, T. H. (1992), *Waves in Plasmas*, American Institute of Physics, New York, NY, doi:QC718.5.W3S75.
- Thébault, E., C. C. Finlay, C. D. Beggan, P. Alken, J. Aubert, O. Barrois, F. Bertrand, T. Bondar, A. Boness, L. Brocco, E. Canet, A. Chambodut, A. Chuliat, P. Coisson, F. Civet, A. Du, A. Fournier, I. Fratter, N. Gillet, B. Hamilton, M. Hamoudi, G. Hulot, T. Jager, M. Korte, W. Kuang, X. Lalanne, B. Langlais, J.-M. Léger, V. Lesur, F. J. Lowes, S. Macmillan, M. Mandea, C. Manoj, S. Maus, N. Olsen, V. Petrov, V. Ridley, M. Rother, T. J. Sabaka, D. Saturnino, R. Schachtschneider, O. Sirol, A. Tangborn, A. Thomson, L. Tøffner-Clausen, P. Vigneron, I. Wardinski, and T. Zvereva (2015), International Geomagnetic Reference Field: the 12th generation, *Earth, Planets and Space*, 67(1), 79, doi: 10.1186/s40623-015-0228-9.
- Thorne, R. M. (2010), Radiation belt dynamics: The importance of wave-particle interactions, *Geophysical Research Letters*, 37(22), 1–7, doi:10.1029/2010GL044990.
- Thorne, R. M., W. Li, B. Ni, Q. Ma, J. Bortnik, L. Chen, D. N. Baker, H. E. Spence, G. D. Reeves, M. G. Henderson, C. A. Kletzing, W. S. Kurth, G. B. Hospodarsky, J. B. Blake, J. F. Fennell, S. G. Claudepierre, and S. G. Kanekal (2013), Rapid local acceleration of relativistic radiation-belt electrons by magnetospheric chorus, *Nature*, 504(7480), 411–414, doi:10.1038/nature12889.
- Tsyganenko, N. A., and M. I. Sitnov (2005), Modeling the dynamics of the inner magnetosphere during strong geomagnetic storms, *Journal of Geophysical Research: Space Physics*, 110(A3), 1–16, doi:10.1029/2004JA010798.

- Ushio, T., M. Sato, T. Morimoto, M. Suzuki, H. Kikuchi, A. Yamazaki, Y. Takahashi, Y. Hobara, U. Inan, I. Linscott, Y. Sakamoto, R. Ishida, M. Kikuchi, K. Yoshida, and Z.-I. Kawasaki (2011), The Global Lightning and Sprite Measurement (GLIMS) Mission on International Space StationNo Title, *IEEJ Transactions on Fundamentals and Materials*, 131(12), 971–976, doi: <http://dx.doi.org/10.1541/ieejfms.131.971>.
- Van Allen, J. A. (1958), Observation of High Intensity Radiation by Satellites 1958 Alpha and Gamma, *Journal of Jet Propulsion*, 28(9), 588–592, doi:10.2514/8.7396.
- Vette, I. (1991), The Model Trapped Electron Environment, *Environment*.
- Vette, J. I. (1966), Models of the Trapped Radiation environment: Volume I: Inner Zone Protons and Electrons, *Tech. rep.*, Scientific and Technical Information Division; National Aeronautics and Space Administration (NASA).
- Voss, H. D., W. Imhof, M. Walt, J. Mobilia, E. Gaines, J. B. Reagan, U. S. Inan, R. A. Helliwell, D. L. Carpenter, J. P. Katsufrakis, and H. C. Chang (1984), Lightning-Induced Electron Precipitation, *Nature*, 310(30 August 1984).
- Voss, H. D., M. Walt, W. L. Imhof, J. Mobilia, and U. S. Inan (1998), Satellite observations of lightning-induced electron precipitation, *Journal of Geophysical Research*, 103(97), 11,725, doi:10.1029/97JA02878.
- Walt, M. (1964), The Effects of Atmospheric Collisions on Geomagnetically Trapped Electrons, *Jgr*, 69(19), 3947, doi:10.1029/JZ069i019p03947.
- Walt, M. (1994), *Introduction to Geomagnetically Trapped Radiation*, 1 ed., Cambridge University Press, Cambridge.
- Wang, C. C.-I. (2009), High Fidelity Analog-to-digital Conversion for Spaceborne Applications, Ph.D. thesis, Stanford University.
- Wang, T. N. C., and T. F. Bell (1969), Radiation Resistance of a Short Dipole Immersed in a Cold Magnetoionic Medium, doi:10.1029/RS004i002p00167.

- Wang, T. N. C., and T. F. Bell (1972), VLF/ELF Radiation Patterns of Arbitrarily Oriented Electric and Magnetic Dipoles in a Cold Lossless Multicomponent Magnetoplasma, *Journal of Geophysical Research*, 77(7), 1174–1189.
- Wenaas, E. P. (1978), Spacecraft Charging Effects on Satellites Following Starfish Event, *Tech. Rep. DTL-831090*, Computer Sciences Corp, El Segundo, CA.
- Wygant, J. R., J. W. Bonnell, K. Goetz, R. E. Ergun, F. S. Mozer, S. D. Bale, M. Ludlam, P. Turin, P. R. Harvey, R. Hochmann, K. Harps, G. Dalton, J. McCauley, W. Rachelson, D. Gordon, B. Donakowski, C. Shultz, C. Smith, M. Diaz-Aguado, J. Fischer, S. Heavner, P. Berg, D. M. Malsapina, M. K. Bolton, M. Hudson, R. J. Strangeway, D. N. Baker, X. Li, J. Albert, J. C. Foster, C. C. Chaston, I. Mann, E. Donovan, C. M. Cully, C. A. Cattell, V. Krasnoselskikh, K. Kersten, A. Brenneman, and J. B. Tao (2014), *The Electric Field and Waves Instruments on the Radiation Belt Storm Probes mission*, vol. 9781489974, 183–220 pp., Springer, Inc, doi:10.1007/978-1-4899-7433-4-6.